IRREVERSIBLE ELECTROPORATION FOR THE TREATMENT OF AGGRESSIVE HIGH-GRADE GLIOMA

Paulo A. Garcia

Dissertation submitted to the faculty of the Virginia Polytechnic Institute and State University in partial fulfillment of the requirements for the degree of

Doctor of Philosophy

In

School of Biomedical Engineering and Sciences

Rafael V. Davalos

John L. Robertson

John H. Rossmeisl, Jr.

Christopher G. Rylander

Ge Wang

November 5, 2010

Blacksburg, Virginia

Keywords: Malignant Glioma, Brain Cancer Therapy, Minimally Invasive Surgery, Tumor Ablation, Nonthermal Ablation

IRREVERSIBLE ELECTROPORATION FOR THE TREATMENT OF AGGRESSIVE HIGH-GRADE GLIOMA

Paulo A. Garcia

ABSTRACT

Malignant gliomas (MG), most notably glioblastoma multiforme (GBM), are among the most aggressive of all malignancies. High-grade variants of this type of brain cancer are generally considered incurable with singular or multimodal therapies. Many patients with GBM die within one year of diagnosis, and the 5-year survival rate in people is approximately 10%. Despite extensive research in diagnostic and therapeutic technologies, very few developments have emerged that significantly improve survival over the last seven decades.

Irreversible electroporation (IRE) is a new non-thermal focal tissue ablation technique that uses low-energy electric pulses to destabilize cell membranes, thus achieving tissue death. The procedure is minimally invasive and is performed through small electrodes inserted into the tissue with treatment duration of about one minute. The pulses create an electric field that induces an increase in the resting transmembrane potential (TMP) of the cells in the tissue. The induced increase in the TMP is dependent on the electric pulse parameters. Depending on the magnitude of the induced TMP the electric pulses can have no effect, transiently increase membrane permeability or cause spontaneous death.

In this dissertation we hypothesize that irreversible electroporation is capable of ablating normal (gray and white matter) and pathological (MG and/or GBM) brain tissue in a highly focused non-thermal manner that is modulated through pulse parameters and electrode configuration. Through a comprehensive experimental and numerical investigation, we tested and attained results strongly supporting our hypothesis. Specifically, we developed numerical models that were capable of simulating an entire IRE treatment protocol and would take into account pulse parameters (e.g. duration, frequency, repetition rate and strength) in addition to

the dynamic changes in tissue electrical conductivity due to electroporation and joule heating, as well as biologically relevant processes such as blood perfusion and metabolic heat. We also provided a method to isolate the IRE effects from undesired thermal damage in models that were validated with real-time temperature measurements during the delivery of the pulses. Finally we outlined a procedure to use 3D volumetric reconstructions of IRE lesions using patient specific MRI scans in conjunction with the models described for establishing field thresholds or performing treatment planning prior to the surgical procedure; thus supplying the readers with the tools and understanding necessary to design appropriate treatment protocols for their specific application.

Experimentally we presented the first systematic *in vivo* study of IRE in normal canine brain and the multimodal treatment of a canine MG patient. We confirmed that the procedure can be applied safely in the brain and was well tolerated clinically. The lesions created with IRE were sub-millimeter in resolution and we achieved 75% tumor volume reduction within 3 days post-IRE in the patient. In addition to the sharp delineation between necrotic and normal brain, the treatments spared the major blood vessels, making it appropriate for treatment of tumors adjacent to, or enveloping critical vascular structures. We believe that irreversible electroporation will play a key role in the treatment of intracranial disorders including malignant brain cancer in which the intent is to focally kill undesired tissue while minimizing damage to surrounding healthy tissue.

To my mom...

ACKNOWLEDGMENTS

Throughout my life, I have been very lucky to be surrounded by people that have been extremely supportive and encouraging. I would like to first thank my mother for all the sacrifices that she made in order for me to get an excellent education. I admire you more than words can express and I am extremely thankful for all your efforts of putting my siblings and me through school and all the life lessons of perseverance and hard work. I would also like to thank my uncle, Walter, for always being there for my family without expecting anything in return. Finally, I would like to acknowledge Ponchitas and Pipe for being my best friends and always being there to support and guide me.

In addition, I would like to thank my advisor, Dr. Davalos, for giving me the opportunity to work with such an amazing lab in this inspiring project and also for allowing me to participate in awesome conferences and workshops worldwide. I would also like to thank Dr. Rossmeisl, Dr. Bob and Dr. Ellis for the tremendous guidance and expertise that they have provided to me while collaborating with them these last couple years. Thanks as well to the members of the best lab in the world for providing a wonderful learning environment. You guys were crucial in developing experiments, brainstorming ideas, and more importantly, being there for the lab meetings downtown, scientific conferences and special occasion celebrations. Thanks also to Ashby for her help and encouragement in the final stages of my doctoral work.

Finally, I would like to thank some of the many people that contributed in various ways for me to come to the United States and succeed in my education from high school all the way through the completion of my Ph.D. Thank you Martin Felton not only for being a great person but also for planting the seed in the families of Isi Esquenazi, Tito Herrera, Alexa Pacini and Juliana Dorronsoro in order for me to attend Christchurch. Those generous donations allowed me to pursue my dream of attending an American University and whenever capable, I will also do the same in return for those who come behind me and need assistance. In addition, I would like to acknowledge Lindsay, Carol Ann and Terry for their continued love, inspiration, and support. You guys definitely made me feel close to home and I am extremely appreciative for the many wonderful memories. Thanks also to Coach Evans for considering me part of his family and offering his unconditional support.

TABLE OF CONTENTS

LIST OF ABBREVIATIONS

Carmustine or "bis-chloronitrosourea"	BCNU
Central Nervous System	CNS
Computed Tomography	CT
Deoxyribonucleic Acid	DNA
Electrocardiogram	ECG
Electrochemotherapy	ECT
Electrogenetherapy	EGT
Gadolinium	Gad
Glioblastoma Multiforme	GBM
Good Laboratory Practices	GLP
High-Intensity Focused Ultrasound	HIFU
Irreversible Electroporation	IRE
Laser Interstitial Thermal Therapy	LITT
Malignant Glioma	MG
Magnetic Resonance Imaging	MRI
Messenger Ribonucleic Acid	mRNA
Nanosecond Pulsed Electric Field	nsPEF
Primary Brain Tumor	PBT
Radiofrequency	RF
Radiotherapy	RT
Transmembrane Potential	TMP

LIST OF FIGURES

LIST OF TABLES

CHAPTER 1 - MOTIVATION

1.1 MALIGNANT BRAIN TUMORS

Malignant tumors of the central nervous system (CNS) are the third leading cause of cancer-related deaths in adolescents and adults between the ages of 15 and 34; in children, brain tumors are the leading cause of cancer death. Furthermore, the two-year survival rate for patients with glioblastoma multiforme (GBM), a high-grade (IV) astrocytoma, is grim. Prior to the advent of adjunctive therapies protocols combining radiation therapy and temozolomide, fewer than 5% of patients survived more than 2 years. With the use of this combination, 2-year survival, while improved by some months, is still poor – about 26% [176]. One of the reasons for poor survival is that glioma cells infiltrate 2-3 cm beyond the volume of visible tumor [80]. Further, treatment of GBM is limited by inefficient intracellular delivery of chemotherapy because of the lack of permeability of brain tissue to many chemotherapeutic agents. In the past few decades, there has been a steady increase in the incidence of brain cancers and, given the aging population, brain tumors will soon be one of the most commonly encountered human neoplasms.

Common approaches to the treatment of malignant gliomas (MGs) involves surgery [14], radiation therapy [170], and/or various chemotherapeutic regimens [116], and combinations of these three modalities. Neither single nor multimodality treatments are curative [137]. While promising (but sometimes contradictory) results have been seen in GBM patients treated with carmustine (BCNU) wafers [16] or molecular therapies, such as bevacizumab [131], there has been no broad acceptance of methods other than radiation/temozolomide therapy. Practically all patients with the most aggressive malignant glioma -GBM- are refractory to treatments and they die. Many types of cancer, such as mammary gland carcinoma, metastasize readily to the CNS [142], making treatment of secondary (i.e., metastatic) lesions in the brain both imperative and difficult. At present, treatment of both primary and secondary brain tumors is provided to improve or sustain neurological function of the patient, to diminish the size of the tumor growing intracranially, and to lengthen intervals between treatments.

1.1.1 Translational Models of Spontaneous Human MGs

Dogs and humans are the only species in which primary brain tumors (PBTs) are common. Intracranial spontaneous primary tumors in dogs are three times more common than in humans [45, 177]. PBTs account for 1-3% of all deaths in aged dogs where necropsy is performed [97]. An incidence rate of 14.5 cases/100,000 dogs at risk has been reported; this may be imprecise, as actuarial data are not collected on most dogs at time of death [186]. Over 70% of primary tumors occur in dogs aged six years or more, a period in lifespan comparable to middle age in humans, although they may occur in younger animals as well. Astrocytomas, oligodendrogliomas and invasive meningiomas are most common [118]. High grade astrocytomas, anaplastic oligodendrogliomas, and mixed anaplastic astrocytic oligodendrogliomas, all histomorphologically identical to those seen in humans, have been reported [96].

Breed predispositions to the development of MGs include a high incidence in broad-headed dogs (Bulldogs, Boxers, and Boston Terriers) and are strongly indicative of the presence of one or more malignant glioma-related oncogenes linked to phenotype. Members of our research team have demonstrated overexpression of several oncoproteins, found in human MGs, including ephrin 2a, interleukin 13-Ra2, and Fra-1, also being overexpressed in identical dog tumors, again showing the strong, translational homology.

Dogs with malignant gliomas present with significant clinical signs, including seizures, depressed or disoriented mental status (assessed by standard neurologic evaluations), and motor dysfunction [109]. Radiographic features on computed tomography of the major tumor types (astrocytoma, oligodendrogliomas, and meningiomas) were helpful in diagnosis, but could be markedly improved with use of more sophisticated imaging studies, such as high resolution MRI and diffusion tensor imaging (DTI), as demonstrated by our recent work using rats [6]. Unfortunately, patterns of survival for dogs with MGs are similar to those seen in people, with death relatively soon (weeks to months) after diagnosis, for those animals that are not humanely euthanized at the time of diagnosis.

Thus, new specific methods of MG treatment, aimed at curing tumors, are needed urgently. In this dissertation, we describe a plan to further develop a novel, a minimally-invasive but highly effective therapy known as irreversible electroporation (IRE) for the treatment of high-grade malignant glioma.

1.2 DISSERTATION OVERVIEW

This dissertation systematically investigates the feasibility and efficacy of using irreversible electroporation as a method for brain cancer treatment, specifically aggressive high-grade gliomas. After a brief history of irreversible electroporation and its potential as a tissue ablation technique we provide some of the theoretical background of electroporation and summarize some of the pre-clinical studies in organs outside of the central nervous system (CNS). In addition, the therapeutic applications of other techniques that also use pulsed electric fields are presented. All of these techniques have one thing in common which is that an electric field is generated and is responsible for the outcome of the treatments.

Chapter 3 explores the numerical modeling aspect needed to simulate some of the effects of the electric fields in tissue. Specifically, we use two different electrodes geometries to investigate the types of electric field and temperature distributions in tissues that are exposed to electric pulses typically used in irreversible electroporation protocols. In addition, we investigate the effects of heterogeneities by simulating treatments in different tissue types. The chapter concludes by quantifying the thermal dose and ensuring that the levels stay low in order to maintain the benefits of a non-thermal treatment.

It is important to accurately model and predict the effects that the pulses induce in tissue. To this end, Chapter 4 describes an experiment in which an *ex vivo* canine brain was treated with two different irreversible electroporation protocols. The importance of the experiment was that for the first time, real-time temperature was measured during the delivery of the high-voltage pulses. We validated the numerical models with the temperature data and introduced the thermal damage concept as a way to prevent undesired damage due to elevated temperatures in the treated tissue.

In Chapter 5, we outline the experiments tailored at assessing the safety and efficacy of using irreversible electroporation for the non-thermal ablation of normal canine brain tissue. These procedures were performed with Institutional Animal Care and Use Committee (IACUC) approval and were necessary in order to familiarize ourselves with intracranial procedures and study the effects in the brain in preparation for canine patients that could potentially be treated at the Teaching Hospital of the Virginia-Maryland Regional College of Veterinary Medicine. These intracranial procedures confirmed the ability of IRE to produce focal ablations that could be modulated with the applied voltage and electrode configuration. In addition, we spared the major vasculature which allows for the treatment of otherwise non-resectable tumors that envelop or are in close proximity to critical vasculature structures.

During the *in vivo* experiments described previously, both ultrasound and magnetic resonance images were acquired immediately after and at 48 hours post-IRE. Chapter 6 attempts to characterize the types of lesions generated by IRE by using image analysis software and numerical models that account for dynamic changes during the treatment due to electroporation and thermal effects. In addition, by generating 3D reconstructions of the lesions a threshold of ~ 500 V/cm is proposed as the required electric field magnitude needed to kill the brain tissue under specific IRE pulse parameters and electrode configurations.

Even though there are several theoretical papers describing the thermal effects induced by irreversible electroporation, in my opinion these simulations lack an assessment of potential thermal damage due to elevated temperatures. Therefore, in Chapter 7 we perform a comprehensive parametric study in which we investigate voltages (500 V, 1000 V, and 1500 V) that are delivered at different frequencies (0.5 Hz, 1.0 Hz, and 4.0 Hz) using similar pulse parameters and identical electrode configurations as in chapter 5. Using the advanced numerical techniques introduced in Chapter 3 and 6, we compared the volumes treated by IRE to those experiencing temperatures of $T > 43°C$, $T > 50°C$, and/or thermal damage values greater that 0.53 which is the onset of 1st degree burns in skin. The results that are presented here take into account naturally occurring physiological processes and provide these volumes as a function of treatment duration so that the all possible treatment effects can be visualized.

We experimentally confirm the non-thermal aspect of irreversible electroporation by measuring the temperature during an *in vivo* computed tomographic guided intracranial procedure in canine brain at two locations along the electrode-tissue interface which are the regions that experiences the highest electric fields and thus heating.

We conclude the dissertation by presenting the results of the first brain cancer patient treated with irreversible electroporation in Chapter 8. In this non-resectable high-grade glioma patient the intent was to reduce the tumor size in order to alleviate some of the clinical signs in order for the dog to be involved in additional radiation therapy. In this patient, for the first time as well we used an isolated 3D tumor reconstruction in our numerical models to plan the IRE treatment. The patient recovered well from the IRE treatment and by 48 hours post-IRE a 75 % reduction in tumor volume was assessed with 3D tumor reconstructions. This allowed for the patient to undergo intense radiotherapy for four weeks and at 4 months post-IRE the brain tumor was in complete remission. The patient developed a complication of radiation therapy (radiation necrosis) and was humanely euthanized at the owner's request. We were able to significantly improve the quality and extend the life of the patient but the tragic outcome has motivated us to continue to investigate the irreversible electroporation and assess its efficacy initially without any other treatment modality.

Chapter 9 summarizes the findings of the previous chapters and addresses some of the future work and relevant issues that need to be investigated before irreversible electroporation becomes one of the standards of care for brain cancer, including malignant high-grade glioma.

CHAPTER 2 - IRREVERSIBLE ELECTROPORATION FOR TISSUE/TUMOR ABLATION – A REVIEW[1]

2.1 INTRODUCTION

Electroporation is a biophysical process in which biological cells are transiently or permanently permeabilized by exposing them to a series of low-energy pulsed electric fields using electrodes. These external pulses induce an increase in the resting transmembrane potential (TMP) of the cells. The induced increase in the TMP is dependent on the electric pulse parameters (i.e. strength, duration, repetition rate, and pulse number) and physical geometry of the electrodes used to deliver the pulses. Depending on the magnitude of the induced TMP the electric pulses can have no effect, transiently increase membrane permeability to exogenous agents or cause spontaneous death due to loss of cell homeostasis. Even though these are the main effects described by the electroporation community, other possible intracellular responses might be responsible for treatment outcome.

Irreversible electroporation (IRE) is the term describing the case in which the membrane is compromised to such an extent that cell death is inevitable. This promising technique is under substantial investigation for the ablation of undesirable tissues, particularly tumors and arrhythmogenic regions in the heart [1, 2, 32, 36, 49, 50, 143, 155]. The procedure involves placing electrodes around the targeted tissue and delivering a series of intense but short electric pulses. These pulses induce irrecoverable structural changes in the cell membranes of the targeted tissue, ultimately leading to cell death. IRE is a form of molecular surgery since it only affects a single molecular component of the treated volume, the cell membrane. In addition, the procedure is minimally invasive, requires only a few minutes for administration, promotes an immune response, supports rapid lesion resolution, and may be monitored in real-time with ultrasound [1, 110, 121, 143]. IRE has the ability to create complete and predictable cell ablation with sharp transition between normal and necrotic tissue, while preserving important components of the tissue such as the extracellular matrix, major blood vessels, myelin sheaths, and nerves.

[1] Portions of Chapter 2 were reprinted with permission from NOVA Science Publishers, Inc. from: Non-thermal irreversible electroporation for tissue ablation, in Electroporation in Laboratory and Clinical Investigations, Enrico P. Spugnini and A. Baldi, Editors. 2010, Nova Science: Hauppauge, NY. Authors: Garcia, P.A., R.E. Neal II, and R.V. Davalos.

This chapter introduces the reader to irreversible electroporation for tissue ablation with particular application to cancer therapy. To this end, after providing a historical perspective, we present a brief theoretical review of electroporation using analytical expressions and numerical models of the induced effects of electroporation in spherical and spheroidal cells. Finally, we present a review of some of the most recent pre-clinical IRE studies and other therapeutic applications of pulsed electric fields in tissue.

2.2 HISTORY

It is difficult to discern when IRE was first observed. The literature suggests that the initial studies could have been as early as the 18th century [15, 57, 59, 138, 151]. However, it was not until 1967 that Sale and Hamilton demonstrated the non-thermal lethal effect of high electrical fields on organisms [73, 154, 160, 161]. They concluded that the damage to the cell membrane occurs when the transmembrane potentials of around 1 V are reached. This threshold is based on the theoretical electric potential distribution of an insulating sphere in a conducting medium in an analysis that has become a classic in the field of electroporation and is presented in the following section [73, 154, 160, 161, 165].

For decades, IRE has been studied extensively within *in vitro* cellular systems, in particular the food industry for sterilization and preprocessing of food [47, 183]. IRE has also been considered an effective means to destroy both gram positive and gram negative bacteria and amoebae with regards to water decontamination for biofouling control [91, 153, 164, 188].

Another context in which IRE has been studied is in the delayed cell damage in high-voltage accidents [111, 113] and the post-electric-shock arrhythmias during defibrillation [90]. Lee *et al.* showed that electrical injury is attributed to thermal damage as well as IRE in superposition [111, 113]. It had also been observed in medical applications involving thermal ablation using electrical fields that the electrosurgical tools also induce electroporation and that coagulation may be due to electrofusion of the membranes [13].

In traditional electroporation experiments in vitro, IRE had been seen as a negative effect since the purpose of such a technique is to introduce a macromolecule through the membrane without affecting the viability of the cell population. It was not until recently that Davalos, Mir and Rubinsky postulated that IRE could be induced *in vivo* to destroy substantial

volumes of targeted tissue prior to the onset of thermal damage [36]. It had been shown on *in vitro* experiments that IRE is an effective means to kill mammalian cells, including cancerous ones [102, 148]. However, if IRE could not ablate a significant amount of tissue prior to the onset of thermal damage, there would be no benefit to using IRE over thermal ablation techniques since it would act in superposition. Alternatively, there would be tremendous advantages in using IRE if it could non-thermally kill the targeted area while sparing major blood vessels, connective tissue, nerves, and the surrounding tissue. The integrity of these structures is vital for the healing of the tissue after surgery. Their hypothesis that IRE could be used as an independent modality for tissue ablation was confirmed in small animal models in the liver [49], and on tumors [1], as well as in large animal models in the liver [155], the prostate [143], and the heart [108]. These *in vivo* studies yielded a wealth of information pertaining to the additional benefits of IRE ablation procedures as described below.

Irreversible electroporation is therefore a new surgical technique to ablate undesirable tissue [36]. The technique is easy to apply, can be monitored and controlled, is not affected by local blood flow, and does not require the use of adjuvant drugs to kill tissue. The minimally invasive procedure involves placing needle electrodes into or around the targeted area to deliver a series of short and intense electric pulses that induce structural changes in cell membranes that promote cell death. The results from the previous studies confirmed that IRE has great potential as an ablation technique. Due to the need for new and precise brain cancer treatments, we decided to investigate the feasibility and efficacy of using IRE for the treatment of aggressive high-grade gliomas. Specifically, we hypothesize that irreversible electroporation is capable of ablating normal (gray and white matter) or pathological (MG and/or GBM) brain tissue in a highly focused non-thermal manner that is modulated through pulse parameters and electrode configuration.

2.3 THEORY OF ELECTROPORATION

The cell membrane is a complex biological system that separates the interior of a cell to the extracellular environment. The membrane is composed primarily of a thin phospholipid bilayer with embedded proteins that regulate the movement of substances in and out of the cell. The permeability of the membrane to molecules is dependent on the electric charge, size

and conformation of the molecules. The cell membrane is basically a non-conductive barrier that protects and controls the transport in and out of the cell through ion channels and the membrane's resting potential. Electroporation is a molecular tool and an electromechanical method used to introduce polar molecules into a cell through the cell membrane via intense and short electrical fields [199].

When cells are exposed to pulsed electric fields that are much longer than their charging time, the induced transmembrane potential reaches steady-state within microseconds of the exposure. In this general case, the membranes act as electrical insulators that prevent the current from entering the cell. The local distortions of the electric field around the cells and its vicinity can be attributed to the discrepancy between the membrane's much lower electric conductivity compared to both the intracellular and extracellular environments [101]. Since the electric conductivity is several orders of magnitude smaller than the intracellular and extracellular compartments, most of the electric field in the cell is concentrated within the membrane itself [101]. The magnitude of the TMP is proportional to the amplitude of the applied electric field, and with a sufficiently strong field, there is a significant increase in membrane permeability [150]. Thus, the analytical expressions and numerical models at the single cell level attempt to characterize the induced TMP by external electric fields and are presented in the following sections in conjunction with the predominant theory of pore formation. There are additional models that account for dynamic changes during electroporation in order to calculate the number of pores and distribution of pore radii as functions of time and positions on the surface of spherical cells and can be found in [103] for further reference.

2.3.1 Analytical Transmembrane Potential in Spherical and Spheroidal Cells

The natural transmembrane potential is on the order of ~-70 mV from the inside to the outside ($V_{intracellular} - V_{extracellular}$) in healthy cells. If the potential drop across the membrane is made to exceed approximately 1 V by the action of an applied electric field, structural rearrangement of the lipid bilayer occurs, creating permanent aqueous pathways or pores for ions and macromolecules to pass through, i.e. electroporation [160]. The analytical expression of the steady-state induced transmembrane potential in spherical cells was derived by H. P.

Schawn several decades ago [165]. In his derivation Schwan assumed that the membrane was electrically non-conductive and of a uniform thickness. This resulted in the well-known steady-state Schwan's equation

$$\Delta\Phi(\theta) = \frac{3}{2} ERcos(\theta) \tag{1}$$

where $\Delta\Phi(\theta)$ is the induced transmembrane potential, *E* is the applied electric field, *R* is the radius of the cell and θ is the polar angle measured from the center of the cell with respect to the direction of the electric field. Under physiological conditions Equation 1 only differs by several parts per thousand from the exact expression

$$\Delta\Phi(\theta) = \frac{3}{2} \frac{\sigma_e[3dR^2\sigma_i + (3d^2R - d^3)(\sigma_m - \sigma_i)]}{[R^3(\sigma_m - 2\sigma_e)\left(\sigma_m + \frac{1}{2}\sigma_i\right) - (R-d)^3(\sigma_e - \sigma_m)(\sigma_i - \sigma_m)]} ERcos(\theta) \tag{2}$$

where $\sigma_e, \sigma_m,$ and σ_i are the electric conductivities of the extracellular environment, cell membrane and intracellular space (cytoplasm), respectively, and *d* is the membrane thickness [99]. The complete expression is only valid under the assumptions of uniform membrane thickness and membrane conductivity, and reduces to Equation 1 when $\sigma_m = 0$ due to the cancellation of the *d*, σ_i, and σ_e.

The typical formula to approximate the induced transmembrane potential, $\Delta\Phi(\theta, t)$, resulting from a time-dependent (response to step function of a DC current including square/rectangular pulses) electric field for a cell in suspension is given by

$$\Delta\Phi(\theta, t) = \frac{3}{2} ERcos(\theta)\left[1 - \exp\left(-\frac{t}{\tau}\right)\right] \tag{3}$$

where τ is the time constant of the membrane and is given by

$$\tau = \frac{R \cdot C_m}{\frac{2\sigma_e\sigma_i}{2\sigma_e + \sigma_i} + \frac{R}{d}\sigma_m} \tag{4}$$

with the C_m term denoting the membrane capacitance ($C_m = \frac{\varepsilon_m}{d}$) which is a function of the membrane's relative permittivity, ε_m, and the thickness [100]. For most electroporation cases as shown in Figure 1, the transient terms can be neglected because the pulse durations (50 µs - 50 ms) are much longer than the membrane charging time, which is approximately 1 µs for spherical cells about 10 µm in diameter. In the remainder of this dissertation, the transient

terms will be neglected but for applications where very short (nsPEFs) pulses are used they must be included [194].

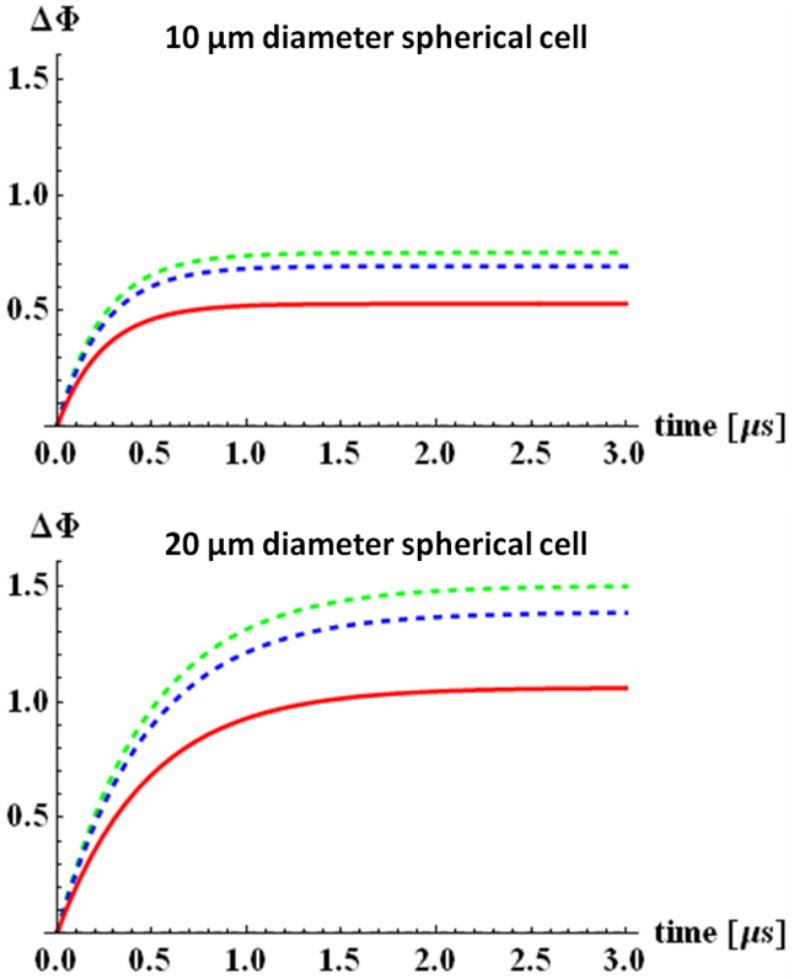

Figure 1: Transmembrane potential (TMP) in response to a time-dependent external electric field for a spherical cells with diameters of (top) 10 µm and (bottom) 20 µm. Note: There is an indirect correlation between the TMP and the position on the cell denoted by the angles from top to bottom $\rightarrow 0\ (\mathrm{top}), {}^{\pi}/_{8}, {}^{\pi}/_{4}, {}^{\pi}/_{2}\ (\mathrm{bottom})$.

The analytical description of the potential distribution induced in non-conductive and conductive spheroidal cells has been derived [19, 89]. This work was used by Kotnik *et al.* to derive the steady-state transmembrane potential of the spheroidal cells using spherical coordinates [101] which is given by

$$\Delta\Phi(\theta) = \begin{cases} E\dfrac{R_2^2-R_1^2}{\frac{R_2^2}{\sqrt{R_2^2-R_1^2}}\operatorname{arccot}\left(\frac{R_1}{\sqrt{R_2^2-R_1^2}}\right)-R_1}\dfrac{R_2\cos(\theta)}{\sqrt{R_1^2\sin^2(\theta)+R_2^2\cos^2(\theta)}}; & R_1 < R_2 \\ E\dfrac{R_1^2-R_2^2}{R_1-\frac{R_2^2}{\sqrt{R_1^2-R_2^2}}\log\left(\frac{R_1+\sqrt{R_1^2-R_2^2}}{R_2}\right)}\dfrac{R_2\cos(\theta)}{\sqrt{R_1^2\sin^2(\theta)+R_2^2\cos^2(\theta)}}; & R_1 > R_2 \end{cases} \quad (5)$$

where *E* is the applied electric field, $R_1$is the radius along the axis of rotational symmetry (polar radius), R_2 is the radius perpendicular to the axis of rotational symmetry, and θ is the polar angle measured from the cell center with respect to the direction of the field. The assumptions in Equation 5 are similar to the ones in the Schwan equation in which there is a non-conductive membrane and the physical conditions are similar to physiological ones. In this expression the induced transmembrane potential is unaffected by the thickness of the membrane (assumed constant) as long as the cell is symmetrical with respect to a plane to which the field is perpendicular. Figure 2 shows the induced transmembrane potentials for the oblate (black – thick dashed), spherical (blue – thin dashed) and prolate (red – solid) cells in units of ER_1 as in [101]. From Figure 2 one can appreciate that the shape of the cell is important in determining the induced transmembrane potential and that the areas closest to the electrodes (i.e. $\theta = \frac{\pi}{2}, \frac{3\pi}{2}$) are where the maximum transmembrane potential values are induced.

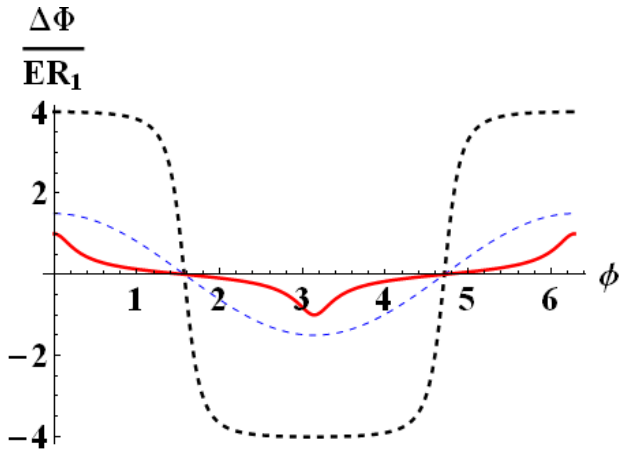

Figure 2: Transmembrane potential normalized by ER_1 as a function of theta. Adapted from [101].

2.3.2 Numerical Determination of Transmembrane Potential

In the previous section we presented several examples of analytical expressions to express the TMP of spherical and spheroidal cells. Even though this method is very useful to

give insight as to the behavior of cells in an electric field, it is limited to a few geometries. In this section, we used the same method and parameters described by Pucihar *et al.* in which the TMP can be calculated using numerical models by a distributed impedance boundary condition that represents the cell membrane [150]. This technique is helpful since cells are not perfect spheres or spheroids and it bypasses the meshing/solving challenges of having geometry dimensions that span over several orders of magnitude like in the case of a cell membrane (~5 nm) versus the cell itself (~10 μm). Most importantly, the procedure can be used in 3-D reconstructions of microscopically imaged cells, providing a realistic description of the influence of the electric fields on the cells [150].

In Figure 3 we outline the distortions that the cells have on a uniform electric field. It is important to note that even though the color maps in the four panels are different they were all generated with a uniform electric field of 1000 V/cm. The variation in color map is representative of the electric field outside of the cell which depends on the orientation of the spheroid cell with respect to the direction of the field. Four different angles were evaluated showing the highest electric field magnitudes when the longest dimension of the cell is perpendicular to the field as in Figure 3A and the smallest electric field when the longest dimension is parallel to the field (Figure 3D).

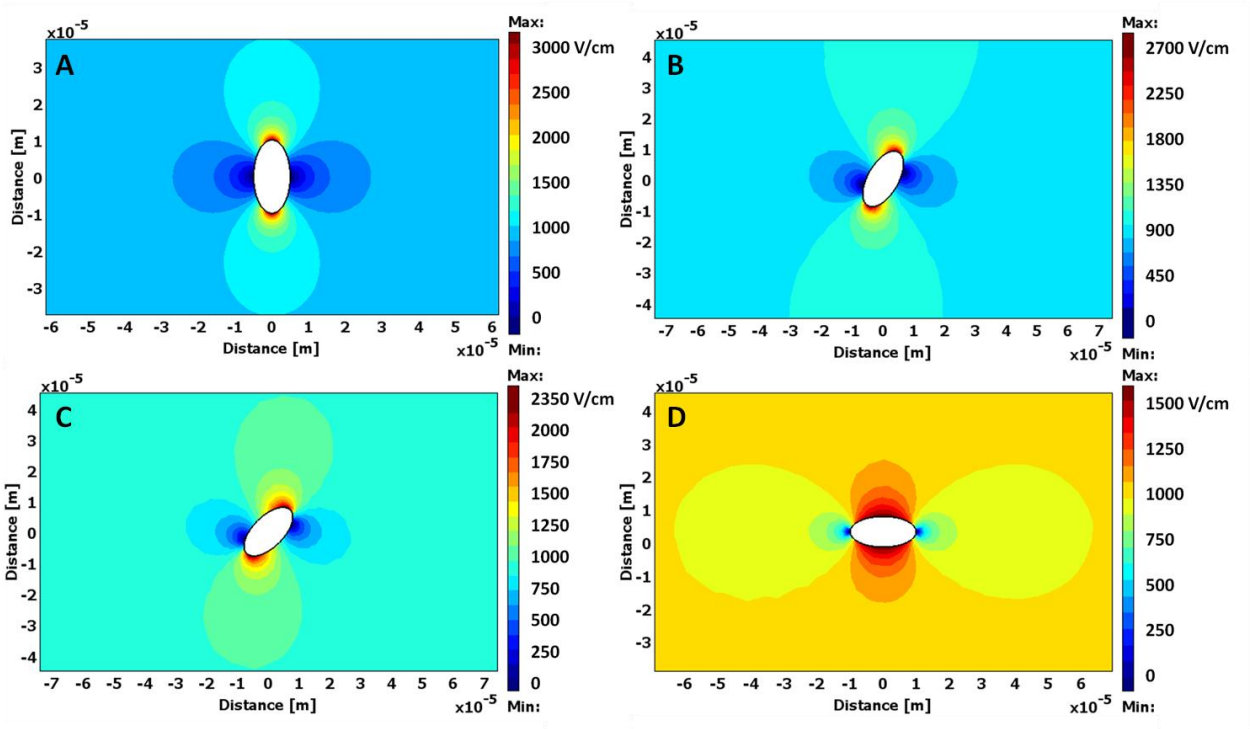

Figure 3: Electric field distributions around the 10 µm x 20 µm ellipsoidal cells exposed to an external electric field of 1000 V/cm at angles of A) 0 degree, B) -30 degrees, C) -45 degrees and D) -90 degrees with respect to the direction of the field (left to right).

In addition to the electric field, one is able to compute the TMP by taking the difference between the electric potentials calculated on the inside and outside of the cell membrane [150]. In this example, TMP is plotted against the arc-length of a 10 µm x 20 µm ellipsoidal cell. From Figure 4 one can visualize that the TMP ranges from 1.5 V to -1.5 V including regions of zero potential along the membrane. This observation is consistent with the regions where the pores are formed, i.e. those regions of elevated TMP. The influence of the orientation of the major axis of the ellipsoid cells with respect to the direction of the electric field is explored by looking at 0, -30, -45, and -90 degrees rotation.

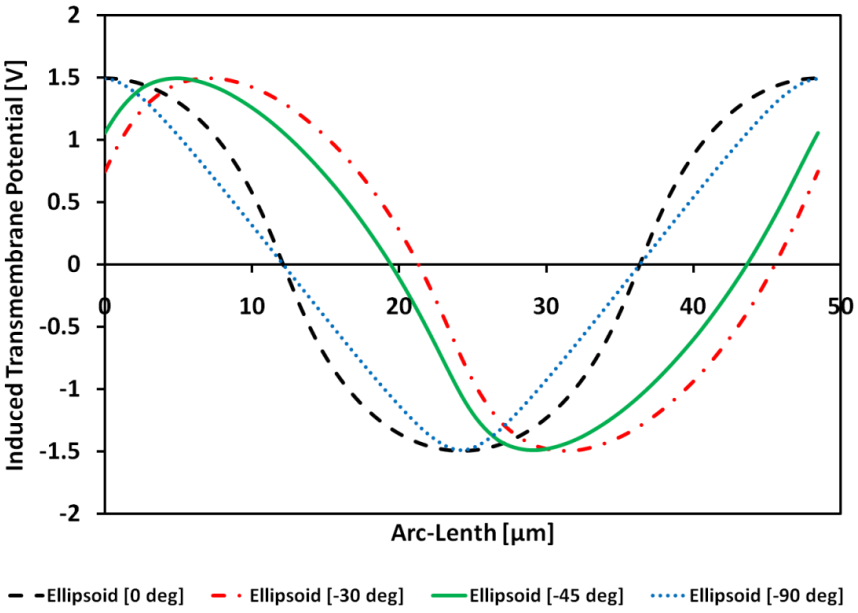

Figure 4: Induced transmembrane potential on spheroidal cells exposed to a uniform electric field of 1000 V/cm.

2.3.3 Dynamics of Electroporation and the Transient Aqueous Pore Hypothesis

Even though the biophysical phenomenon at the molecular level is unknown, the hypothesis is that there is a rearrangement of the lipid bilayer in the plasma membrane that creates water-filled structures, which provide a pathway for ions and molecules that normally are not permeable to the cell membrane. The electroporation dynamics are considered as a four-step process: pore induction, expansion, stabilization and resealing.

Initially, thermal fluctuations are responsible for the spontaneous generation of hydrophobic pores (Figure 5). As shown in Figure 6, there exists a critical radius where it becomes more energetically favorable for one of the hydrophobic pores to transition to into hydrophilic pore. Additionally, increasing the transmembrane potential reduces this critical radius and makes the hydrophilic pore more stable [93]. When the pore reaches this metastable state, it becomes permeable to small molecules and ions. The presence of the induced transmembrane potential lowers the required energy for existence of the pore [189]. When the electric field is no longer there, the membrane starts to return to its normal membrane potential and resealing of the pores occur. However, if excessive voltage is applied the hydrophilic pores become unstable and there is irreversible breakdown (i.e. irreversible electroporation).

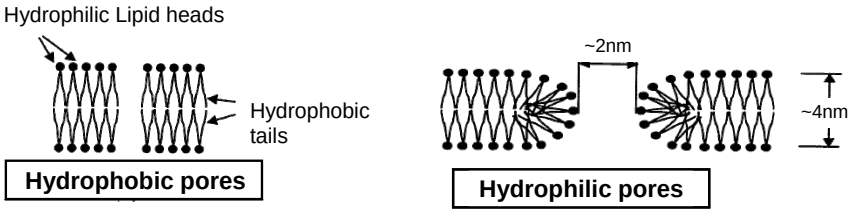

Figure 5: Schematic representing the hydrophobic and hydrophilic pores that are believed to be involved in the electroporation process [134].

The transient aqueous pore hypothesis has been described in detail by Krassowska [38, 39] and it is the most widely accepted theory for electroporation. The roots can be found in the works of Chizmadzhev, which postulated that the process of electroporation was due to local "defects" (pores) in the membrane [23]. These works could reasonably predict the threshold voltage for membrane rupture (IRE), but were unable to explain membrane resealing. Further refinement of the membrane pore theory was the launching point to the transient aqueous pore model [193].

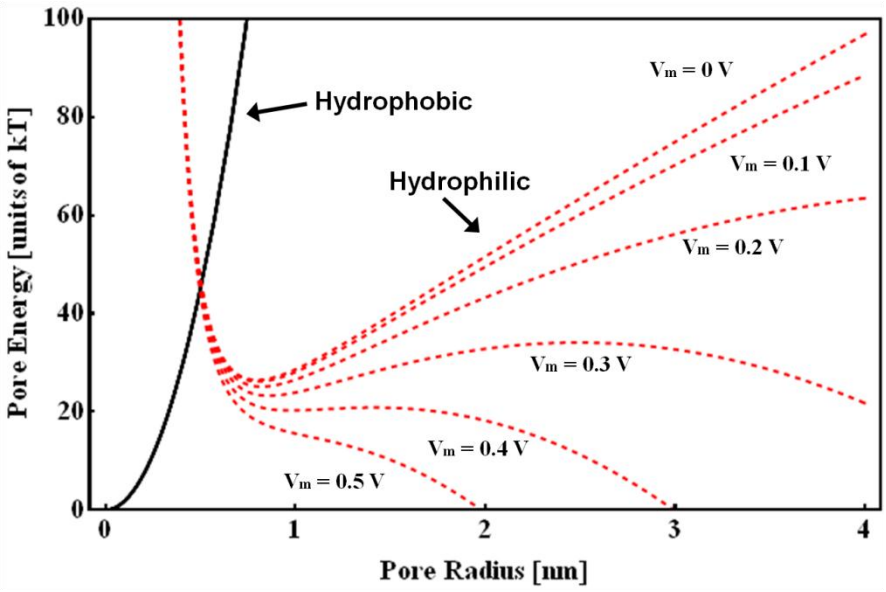

Figure 6: Energy associated with hydrophobic and hydrophilic pores for increasing transmembrane potential (V_m). Dark solid line represents energy associated with hydropobic pore and the dashed red lines represent the energy associated with hydrophilic pore [39, 134]. Figure generated with parameters given in [39].

The main features observed during electroporation of planar bilayer are described accurately with the aqueous pore model. In addition, this model can explain most of the

observed behavior during electroporation. During the pore induction process, hydrophobic defects are spontaneously created in the membrane by thermal fluctuations.

The energy associated with a hydrophobic pore is given by

$$E(r) = E_*(\frac{r}{r_*})^2 \quad (6)$$

It is generally believed that the pre-existing hydrophobic pores become hydrophilic in order to minimize their free energy [193]. Even though water is able to pass through these pores [67], ions are not due to the extra energy needed. When the water-filled defects or hydrophobic pores grow (resulting from the increased TMP) to a radius of 0.3 nm to 0.5 nm, a hydrophilic pore forms by the reorientation of the lipid molecules into an structure that is more energetically favorable (Figure 6) [67].

The hydrophilic pore formation energy is based on classical surface chemistry. The approach compares the change in energy of an intact membrane with one that has a circular region of radius r missing. The pore formation energy, $E(r)$, is the difference from the gain in edge energy of the pore (γ) and the reduction in energy due to the loss of a circular patch that has been removed from the membrane ($\pi\sigma r^2$). The constant γ is the energy per length along the circumference needed to form the pore and σ is the energy per area of a flat, pore-free membrane [193]. The expression for the pore formation energy is given by

$$E(r) = 2\pi\gamma r - \pi\sigma r^2 + (\frac{C}{r})^4 \quad (7)$$

Equation 7 provides some insight as to the significant barrier that thermal fluctuations must overcome in order to create a hydrophobic pore (Figure 6). As described previously, the applied external electric field increases the TMP and thus plays a considerable role in pore formation. In addition, as hydrophilic pores are created, the electrical energy associated with the lipid molecules being replaced by water needs to be considered [39]

$$\varphi(r) = E(r) - \pi a_p V_m^2 r^2 \quad (8)$$

where V_m is the TMP and $\pi a_p V_m^2 r^2$ is the capacitive contribution.

Despite studies, relatively little is known about the mechanism by which IRE causes cell death. There have been numerous experimental studies on cell viability following the delivery

of an electric pulse [60, 82, 102, 117]. Yet, there are disagreements within the literature. There is an ongoing debate whether IRE-induced cell death is caused by: (1) cell membrane rupture [191, 192], (2) excessive leakage through pores [81, 191, 192], or (3) thermal damage to cells [92]. The three proposed mechanisms have different scaling laws that relate the strength (E) and duration (d) of the threshold electric pulse for cell death. In particular, for rupture: ln(d) ~ $1/E^2$; for leakage: d ~ 1/E; and for thermal damage: d ~ $1/E^2$ [103]. Some studies find a correlation between cell death and the total energy delivered by the pulse [92, 141], while others do not [164, 187]; and yet others correlate cell death with the total pulse charge [102]. Despite the varying mechanism theories, IRE has been tested in animal models of disease and is currently being investigated for human applications. This dissertation provides a summary of some of the published investigations that have been performed to date.

2.4 PRE-CLINICAL ANIMAL MODELS

Recently, IRE was shown to be an effective method to treat tumors through studies with aggressive cutaneous mouse sarcoma tumors *in vivo* in preclinical mouse models [1]. The electrical pulses were delivered through two plate electrodes placed across the tumors. Complete regression was achieved in 12 out of 13 treated tumors when eighty 100 µs pulses were delivered at a repetition rate of 1 pulse every 3.3 seconds using an applied electric field of 2500 V/cm (Figure 7). Histology verified that ablation occurred as a direct result of irreversible membrane permeabilization [1]. These results were achieved with a single treatment that lasted less than five minutes.

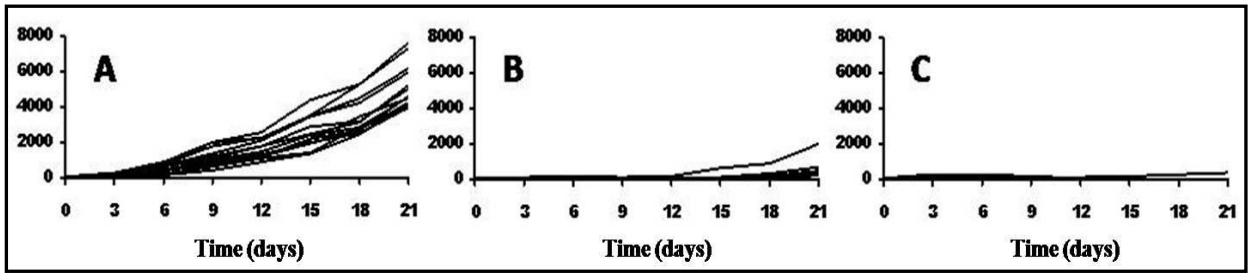

Figure 7: Tumor volume (mm^3) within nude mice after IRE treatment as a function of days after treatment. A: No treatment – tumors continue to grow. B: Eight 1000 µs pulses at 0.03 Hz deterred growth tumors and 4/13 tumors completely regressed. C: Eighty 100 µs pulses at 0.3 Hz deterred growth and 12/13 tumors completely regressed. Parameters were characterized by the same total energized (8 ms) and treatment durations (267 s). Adapted from [1].

An original *in vivo* study conducted by Edd *et al.* used a single 20-ms-long square wave pulse of 1000 V/cm (chosen to have no significant thermal effect) applied across rat livers using two plate electrodes three hours before sacrificing the animals and performing histology on the liver [49]. It was found that the livers experienced microvascular occlusion while large vessel architecture was preserved as well as a strong demarcation between regions that were unaffected, and those that experienced IRE induced cell death.

The preservation of vasculature was more thoroughly investigated by Maor *et al.* [121], where ten 100 μs pulses of 3800 V/cm at a frequency of 10 pulses per second were administered across the carotid artery of six rats 28 days before histology. This study found a large decrease in the number of vascular smooth muscle cells without evidence of aneurysm, thrombus formation, or necrosis. In addition to promoting the efficacy of performing IRE procedures on regions near major blood vessels and the potential application of IRE to treat pathological processes involving excessive proliferation of vascular smooth muscle cells, such as restenosis, an increase in conductivity of the tissue during treatment was found, resulting from the increased permeability of the cell membranes.

In a study on swine liver from [110], a total of 11 lesions were created using monopolar and bipolar electrodes with ninety 100 μs pulses ranging from 1000 to 1667 V/cm. This study showed complete hepatic cell death without extracellular structural destruction as well as hypoechoic properties to the ablated regions during procedure administration, allowing real-time procedure monitoring using ultrasound.

A preclinical study on the implications of IRE for the ablation of prostate tissue (both cancerous and regions exhibiting prostatitis) was performed by [143], where one or four bipolar or monopolar electrodes were placed in the prostates of six beagle dogs before administering eighty pulses of 100 μs ranging from 1000 to 3000 V/cm. This study found IRE lesions with a narrow transition between complete necrosis and unaffected tissue, with complete destruction of the IRE lesion and resolution within two weeks, as observed by marked shrinkage. The shrinking regions resulting from the procedure show strong adaptability of IRE protocols for the treatment of pathologies involving swollen tissues and organs. This study also examined the effects on sensitive peripheral structures such as the urethra, blood vessels, nerves, and rectum

that have experienced problems with thermal techniques and found all to be unaffected by the IRE treatment application. The preservation of the microvasculature experienced in this study also raises the question for the possibility of normal tissue regeneration within the ablated regions.

A unique observation in the IRE lesions from [143] was evidence of an immunologic reaction, prompting the possibility of a tumor specific immunological reaction that may be promoted by IRE, further enhancing treatment outcome. This also shows the potential for destruction of micro-metastasis in affected lymph nodes, possibly reducing the risk for recurrence. Furthermore, a study was performed on the immunologic response by [2] on implanted tumors from a mouse sarcoma cell line. They used IRE parameters previously found in [1] to yield complete tumor regression (plate electrodes with four trains of 16 pulses 100 µs in length at 2500 V/cm with a 90° electrode rotation between trains) on mice sacrificed 1-72 hours after treatment. Immunohistochemistry was performed, and it was determined that IRE from this procedure did not require an immunological response to produce ablation, suggesting the efficacy of using IRE on immunodepressed patients.

These IRE animal experiments verified the many beneficial effects resulting from this special mode of non-thermal cell ablation. With major structures such as the extracellular matrix, major blood vessels, and myelin sheaths preserved, there is extremely rapid lesion resolution with healthy tissue [155], preventing scar formation and promoting a beneficial immune response [155]. Preventing scar formation is especially important because it allows the determination of treatment success or failure through imaging, something not possible when using thermal techniques [143, 172]. This method also allows treatment in the heart [108] and blood vessels [121] without the danger of coagulation in the blood stream and subsequent emboli.

2.5 OTHER THERAPEUTIC APPLICATIONS OF PULSED ELECTRIC FIELDS IN TISSUE

Irreversible electroporation is currently being studied as part of a family of therapeutic applications that also uses pulsed electric fields in tissue. Some of the other applications include classical electroporation in which the intent is to permeabilize cells in a reversible manner in order to introduce anti-cancer drugs in Electrochemotherapy (ECT) or plasmid DNA in

Electrogenetherapy (EGT) in a non-viral manner [123, 127-130]. There is also an emerging field that uses nanosecond pulsed electric fields (nsPEFs) approximately 40 kV/cm in magnitude to treat tumors [11, 40, 70].

2.5.1 Electrogenetherapy (EGT)

In electrogenetherapy the purpose is to deliver genes that are encoded in a plasmid to specific tissues for cancer and infectious diseases treatment. In order to increase the expression of the gene, electroporation is used in order to permeabilize the cells to these macromolecules. This technique uses much lower electric fields than in IRE but with pulse durations of a couple milliseconds which electrophoretically assist the transport process. The first clinical trial delivering plasmid DNA using *in vivo* electroporation evaluated the safety of the procedure on patients with metastatic melanoma. Since then several other trials are under investigation to evaluate the clinical application of EGT to treat infectious diseases and other disorders with vaccines through electroporation-mediated therapeutic gene delivery.

2.5.2 Electrochemotherapy (ECT)

ECT is a relatively new minimally invasive technique that employs reversible electroporation pulses to facilitate the penetration of non-permeant or low-permeant drugs, such as bleomycin or cisplatin, into cells. A major advantage of ECT is that it selectively kills only rapidly dividing cells, such as tumor cells. In tissue ablation, ECT is a safe and highly efficient method to introduce non-permeable cancer drugs into malignant cells and is currently used to treat cutaneous and subcutaneous tumors in humans [12, 69, 127, 128]. However, this method requires the combination of chemical agents with an electric field, which irreversible electroporation does not.

2.5.3 Nanosecond Pulsed Electric Fields (nsPEF)

Nanosecond pulsed electric fields are achieved by means of electrical pulses in the tens of nanoseconds range and field strengths of 40-80 kV/cm [11, 40]. Previously in nsPEF, it was thought that cell death was not a consequence of the irreversible cell membrane permeabilization as in IRE, but the probable result of Ca^{2+} ions released inside the cells [11]. Recently, it has been shown by several authors that there is in fact cell membrane

permeabilization that might also be responsible for the anti-tumor effectiveness of nsPEFs. R. Nuccitelli *et al.* [139, 140] described antitumor effects in mice using this technique.

2.6 CONCLUSION

This chapter introduced the field of irreversible electroporation and its potential to ablate large tissue volumes. The advantages of IRE over other focal ablation techniques lay within its ability to ablate tissue through a non-thermal mechanism. This method preserves the extracellular matrix, nerves, major blood vessels, and other sensitive tissues, enhancing treatment outcome. This ablation of the targeted areas exhibits rapid lesion creation and resolution, prompting the repopulation of the region with healthy cells. Though treatment success is not dependent upon the immune system, a tumor specific immune response capable of helping to destroy any residual micro-metastases occurs, decreasing the chances of recurrence. These aspects, in conjunction with short treatment times and the minimally invasive nature of treatment administration, show strong potential for using IRE as an effective tissue ablation modality for the improved treatment of many localized tissue pathologies. The new techniques based on the delivery of electric pulses, namely ECT, EGT, IRE, and nsPEFs, have inherent advantages and disadvantages for tissue/tumor ablation. It is quite likely that each will find appropriate uses in modern medicine, separately or in combination.

CHAPTER 3 - NUMERICAL MODELING FOR ELECTROPORATION TREATMENT PLANNING[2]

3.1 INTRODUCTION

In tissue, there are a number of conditions that determine the extent of electroporation, such as tissue type and temperature, as well as a number of pulse parameters, including duration, number, shape, and repetition rate. However, for a given set of conditions, the primary parameter affecting the degree of electroporation is the local electric field strength [32, 125]. Therefore, in order to design protocols for an IRE procedure, the electric field distribution, which is dependent on the procedure's specific electrode-tissue geometry, pulse amplitude, and tissue conductivity distribution, must be determined. Furthermore, to verify that a specific protocol does not induce thermal effects, the temperature distribution can be calculated from the electric field distribution, the electric pulse parameters, and tissue electrical and thermal properties. Knowledge of the electric field and temperature distribution enables surgeons and researchers to reliably predict the results of an IRE procedure. This insight enables surgeons to plan and optimize the electrode geometry and voltage parameters for varying types of tissue and heterogeneities to:

- Ensure treatment of the entire region, especially when multiple applications are necessary
- Minimize applied voltages in order to reduce charge delivered
- Visualize where potential thermal damage may occur to surrounding tissues
- Reduce treatment time, invasiveness, and number of procedures
- Superimpose medical images to plan treatment of the appropriate region

The purpose of this chapter is to supply the readers with the numerical tools and understanding necessary to design appropriate IRE treatment protocols. Therefore, the fundamental theory that determines how electric field and temperature distributions will result from a chosen electrode configuration, pulse characteristics, and the electrical and thermal

[2] Chapter 3 was reprinted with permission from NOVA Science Publishers, Inc. from: Non-thermal irreversible electroporation for tissue ablation, in Electroporation in Laboratory and Clinical Investigations, Enrico P. Spugnini and A. Baldi, Editors. 2010, Nova Science: Hauppauge, NY. Authors: Garcia, P.A., R.E. Neal II, and R.V. Davalos.

properties of the tissue are provided. In addition we highlight the relevant issues to consider and how to account for them when planning IRE therapies.

3.2 BACKGROUND

Electroporation, which results in an increase in the permeability of the cell membrane, is initiated by exposing cells or tissues to electric pulses [193, 195]. As a function of the induced transmembrane potential (the electric potential difference across the plasma membrane), the electroporation pulse can either: have no effect on the cell membrane, reversibly permeabilize the cell membrane, after which the cells can survive (reversible electroporation), or permeabilize the cell membrane in a manner that leads to spontaneous cell death (irreversible electroporation), presumably through a loss of homeostasis if not from other superimposed damage modes. Even though these are the main effects described by the electroporation community, other possible intracellular responses might be responsible for treatment outcome. This increase in transmembrane potential is dependent on a variety of conditions such as tissue type, cell size, and pulse parameters including pulse shape, duration, number, and repetition rate. However, for a specific tissue type and set of pulse conditions, the primary parameter determining the extent of electroporation is the electric field to which the tissue is exposed [50].

3.3 METHOD

To illustrate how the IRE treated area/volume depends on the electrode configuration and applied voltage, two electrode types are analyzed as examples, as depicted in Figure 8. Case A shows single 2-mm diameter bipolar electrode, and case B shows two 1-mm diameter monopolar electrodes, separated by a distance of 10 mm. The red regions are energized and the black ones are set to ground.

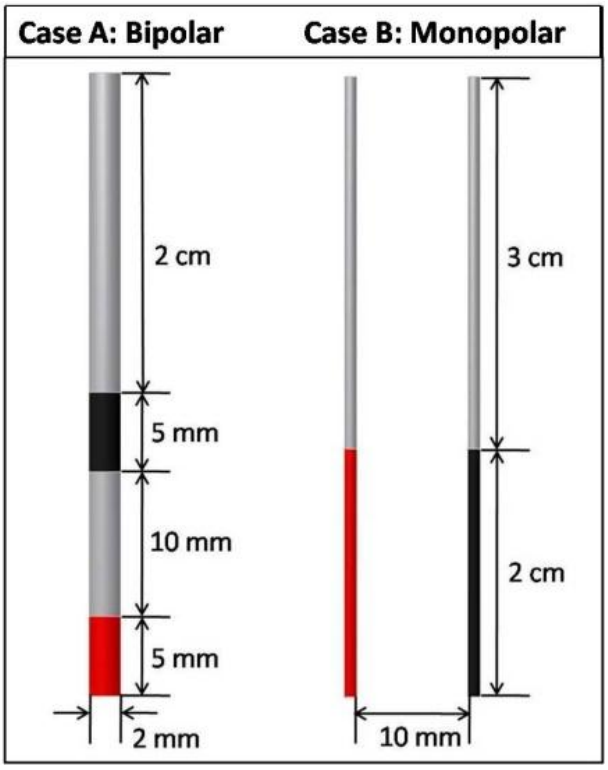

Figure 8: Example models. Case A: One 2-mm diameter bipolar electrode with conducting regions separated by a distance of 10 mm. Case B: Two 1-mm diameter monopolar electrodes separated by a distance of 10 mm. The red regions are energized and the black ones are set to ground. Reprinted with permission from NOVA Science Publishers, Inc. as described in page 23.

3.3.1 Electric Field Distribution

The methods used to generate the electric field and temperature distributions in tissue are similar to the ones described by Edd and Davalos [50]. The electric field distribution associated with the electric pulse is given by solving the Laplace equation:

$$\nabla \cdot (\sigma \nabla \varphi) = 0 \tag{9}$$

where σ is the electrical conductivity of the tissue and φ is the electrical potential [50]. The quasi-static assumption used in the model is valid due to the overall dimensions of the geometry which are small compared to a wavelength in the tissues (i.e. wavelength is much greater than the longest dimension in the geometry). Boundary conditions most often include surfaces where electric potential is specified, as in the case of a source or sink electrode, or surfaces that are electrically insulating, as on the free surfaces of the tissue, for example. The

electrical boundary condition along the tissue that is in contact with the energized electrode is $\varphi = \mathrm{V_o}$. The electrical boundary condition at the interface of the other electrode is $\varphi = 0$. The remaining boundaries are treated as electrically insulating:

$$\frac{\partial \varphi}{\partial \mathrm{n}} = 0 \tag{10}$$

The models are fully defined and readily solvable using a numerical method once an appropriate set of boundary conditions and the properties of the tissue are defined. The computations were performed with a commercial finite element package (Comsol Multiphysics, v.3.5a, Stockholm, Sweden). The analyzed domain extends far enough from the area of interest (i.e. the area near the electrodes) that the electrically and thermally insulating boundaries at the edges of the domain do not significantly influence the results in the treatment zone.

3.3.2 Heterogeneous Tissue

Exposing the entire tissue to the electric field magnitude necessary to achieve cell death is important. However, there can be factors that would make the targeted domain heterogeneous, such as the presence of large blood vessels, multiple tissue types, or tissues with anisotropic properties, such as muscle. Three electric field contour levels (500, 750 and 1000 V/cm) are used to illustrate the effects of heterogeneity in the electric field distribution as shown in section 3.4.2. Under these circumstances, the reader would need to understand these guidelines when making their own model match their specific procedure.

3.3.3 Joule Heating

Joule heating refers to the heat generation rate per unit volume caused by an electric field. As described in [33], the joule heating source term is evaluated by solving the Laplace equation for the potential distribution associated with an electrical pulse. The associated joule heating rate per unit volume, $\dot{q}$, from an electric field, is the square of the absolute value of the local electric field magnitude, $|-\nabla\varphi|$, times the electrical conductivity of the tissue:

$$\dot{q} = \sigma|-\nabla\varphi|^2 \tag{11}$$

A convenient equation to estimate the increase in temperature (ΔT) of homogeneous tissue for the parallel plate configuration from the joule heating is:

$$\Delta T = \frac{\sigma}{\rho c_p} |\nabla \varphi|^2 \Delta t \tag{12}$$

where Δt is the total duration of the pulses, ρ is density and c_p is specific heat of the tissue [102]. This equation assumes no heat dissipation between the pulses, and no fringe effects at the electrode edge. Furthermore, this equation assumes that the biological properties are uniform and the contributions from blood flow, metabolic heat generation, and electrode heat dissipation are negligible.

To account for these other effects, the Pennes bioheat equation is often used to assess tissue heating associated with thermally relevant procedures, because it accounts for the dynamic processes that occur in tissues, such as blood perfusion and metabolism. Blood perfusion is an effective way to dissipate (take away) heat contrary to metabolic processes which generate heat in the tissue. Modifying this equation to include the joule heating term gives the equation the following form:

$$\nabla \cdot (k \nabla T) - w_b c_b \rho_b (T - T_a) + q''' + \sigma |\nabla \varphi|^2 = \rho c_p \frac{\partial T}{\partial t} \tag{13}$$

where k is the thermal conductivity of the tissue, T is the temperature above the arterial temperature ($T_a = 37°C$), w_b is the blood perfusion rate, c_b is the heat capacity of the blood, ρ_b the blood density, q''' is the metabolic heat generation, ρ is the tissue density, and c_p is the heat capacity of the tissue. However, it has been suggested that these factors have a negligible contribution to the overall temperature distribution as compared with joule heating [33]. Therefore, we have neglected the blood perfusion and metabolic heat generation terms in our models.

Several thermal boundary conditions can be employed to study the heat exchange between the electrodes and the tissue [9, 10, 33]. In these models, the electrodes were considered as infinite fins, $h_f = 15 \frac{W}{m^2 \cdot K}$, as described in [33], which dissipate heat from the tissue through the electrodes to the environment. However, in other studies, the boundaries are taken to be adiabatic to predict the maximum temperature rise in the tissue:

$$\frac{\partial \mathrm{T}}{\partial \mathrm{n}} = 0 \tag{14}$$

3.3.4 Common Physical Properties

For the models in this chapter, the physical properties of homogeneous liver are presented to provide insight, but the properties can be easily adapted for other tissues. The values of the liver tissue heat capacity (c_p = 4 kJ·kg^{-1}K^{-1}), electrical conductivity (σ = 0.2 S·m^{-1}), thermal conductivity (k = 0.5 W·m^{-1}K^{-1}), and density (ρ = 1000 kg·m^{-3}) used in the models are taken from the literature [37, 41, 178]. The tissue temperature is assumed to be initially the same as the physiological temperature (37 ^{o}C).

3.3.5 Equivalent Thermal Dose

For procedures involving time varying temperatures, thermal damage can be assessed by calculating the amount of time it would take to equivalently damage the tissue as if it was held at a constant temperature, typically 43°C [1, 9, 37, 50, 163]. The following expression is the duration necessary to hold the tissue at 43°C to result in an equivalent thermal dose:

$$t_{43} = \sum_{t=0}^{t=final} R^{(43-T_t)} \Delta t \tag{15}$$

where T_t is the average temperature during Δt with $R = 0.25$ when $T_t \leq 43°C$ and $R = 0.5$ when $T_t > 43°C$ [31, 163].

3.4 RESULTS

3.4.1 Electric Field Distributions in Homogeneous Tissue

The models for the two treatment relevant electrode geometries outlined above may be seen in Figure 9. A voltage of 2000 V was placed on the energized electrode, and the resulting electric field distribution in tissue with an electric conductivity of σ = 0.2 S/m has been mapped out in the three Cartesian planes (y-z, z-x, and x-y). Based on these models, a general distribution pattern can be seen. It is important to remember that this is a visualization of how the field strength disperses, and that the values of the field seen in the legend will vary with the voltage applied to the energized electrode. It is also important to note that the two needle

array of Case B has a larger exposed surface area than the bipolar electrode of Case A, contributing to its larger volume of high electric field regions.

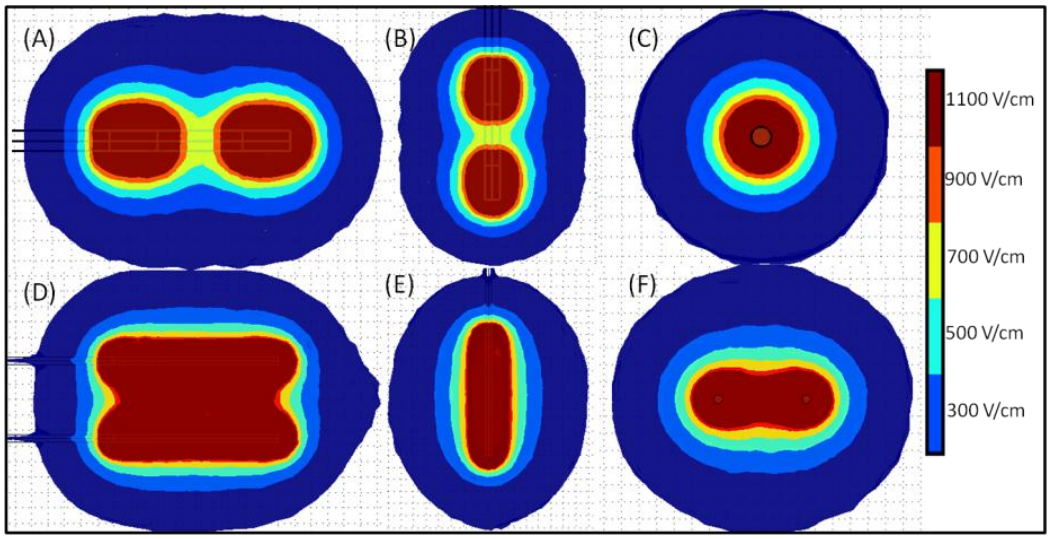

Figure 9: Electric field distribution for the bipolar electrode (A-C) of Case A and the two monopolar electrodes (D-F) of Case B. Images A and D show a cross-section in the y-z plane, B and E in the z-x plane, and C and F in the x-y plane (looking into the electrodes). Reprinted with permission from NOVA Science Publishers, Inc. as described in page 23.

From the images in Figure 9, it can be clearly seen that the strongest electric fields will occur directly beside the electrodes as two distinct ellipses that will connect at the center, forming a "peanut" shape, before expanding into an ellipse. For the bipolar electrode of Case A, the greatest fields occur in concentric rings (Figure 9C) expanding out from the electrode, indicating that inserting this electrode directly into the targeted tissue would yield the most symmetric results. The monopolar needle array has the greatest fields immediately around the conducting surfaces and then expanding inwards between them, suggesting this arrangement would work better when placed slightly on opposing regions of the targeted tissue.

3.4.2 Electric Field Distributions in Heterogeneous Tissue

Figures 10-12 show the tissue treated with a 2000 V (50 µs pulse length) IRE pulse using the same dimensions as Case B in Figure 8. It is important to note that different tissues may have different electric field thresholds to cause IRE. In an IRE treatment, if the conductivity distribution in the targeted region is homogenous, the results in Figure 10 can be applied

directly to estimate the size of the treated region as a function of electrode geometry and applied voltage.

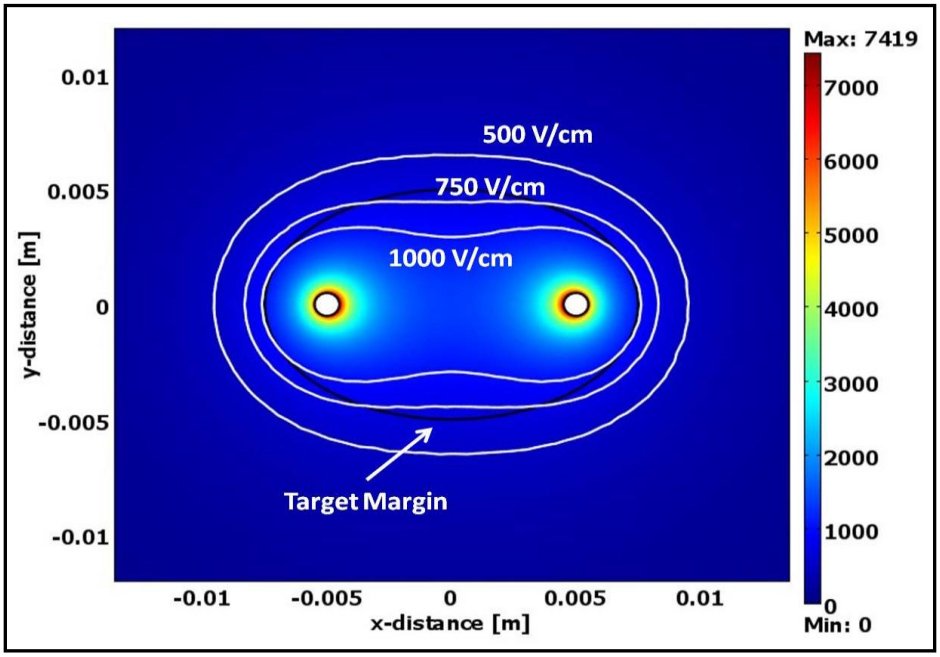

Figure 10: Electric field [V/cm] distribution using a 2000 V (50 µs) IRE pulse in homogeneous tissue ($\sigma_{target} = \sigma_{surrounding}$). The black line outlines the area to be treated with IRE. Reprinted with permission from NOVA Science Publishers, Inc. as described in page 23.

Figure 11 shows the electric field distribution for an IRE procedure in which the electrical conductivity of the surrounding tissue (σ = 0.1 $S \cdot m^{-1}$) is half the magnitude of the treated tissue (σ = 0.2 $S \cdot m^{-1}$). The same electric field contour levels (500, 750 and 1000 V/cm) that were used in the homogeneous tissue discussion were used in this analysis. Having two different electrical conductivities affects the electric field distribution, so knowledge of the physical properties of the tissue is important for more accurate predictions. The treated area by IRE is increased when the surrounding tissue to the region of interest has a smaller electrical conductivity. For example, an electric field of 750 V/cm covers the entire region of interest but was not sufficient to treat the homogeneous tissue. This scenario can occur in mammary tumors in which the fat surrounding the tissue has lower electrical conductivity than the tumor itself.

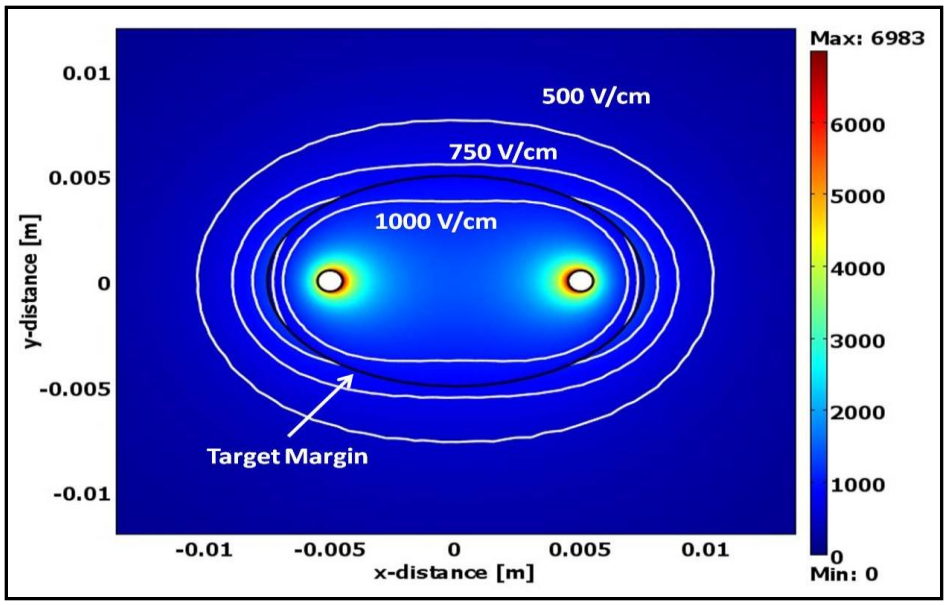

Figure 11: Electric field [V/cm] distribution using a 2000 V (50 µs) IRE pulse in heterogeneous tissue. The black line outlines the area to be treated with IRE ($0.5 \cdot \sigma_{target} = \sigma_{surrounding}$). Reprinted with permission from NOVA Science Publishers, Inc. as described in page 23.

Figure 12 shows the electric field distribution for an IRE procedure in which the electrical conductivity of the surrounding tissue (σ = 0.4 S·m^{-1}) is twice the magnitude of the treated tissue (σ = 0.2 S·m^{-1}). The same electric field contour levels (500, 750 and 1000 V/cm) that were used in the two previous examples were used in this analysis. The treated area by IRE is reduced when the surrounding tissue to the region of interest has a larger electrical conductivity. For example, an electric field of 500 V/cm is now required to cover the entire region of interest which is lower than was needed to treat the homogeneous tissue. These results are to give insight to the reader about the influence of the electrical conductivity in the electric field distribution in heterogeneous tissue. For more information on these effects, other studies of electric fields on heterogeneous tissue can be found in [50, 53, 54, 125, 132].

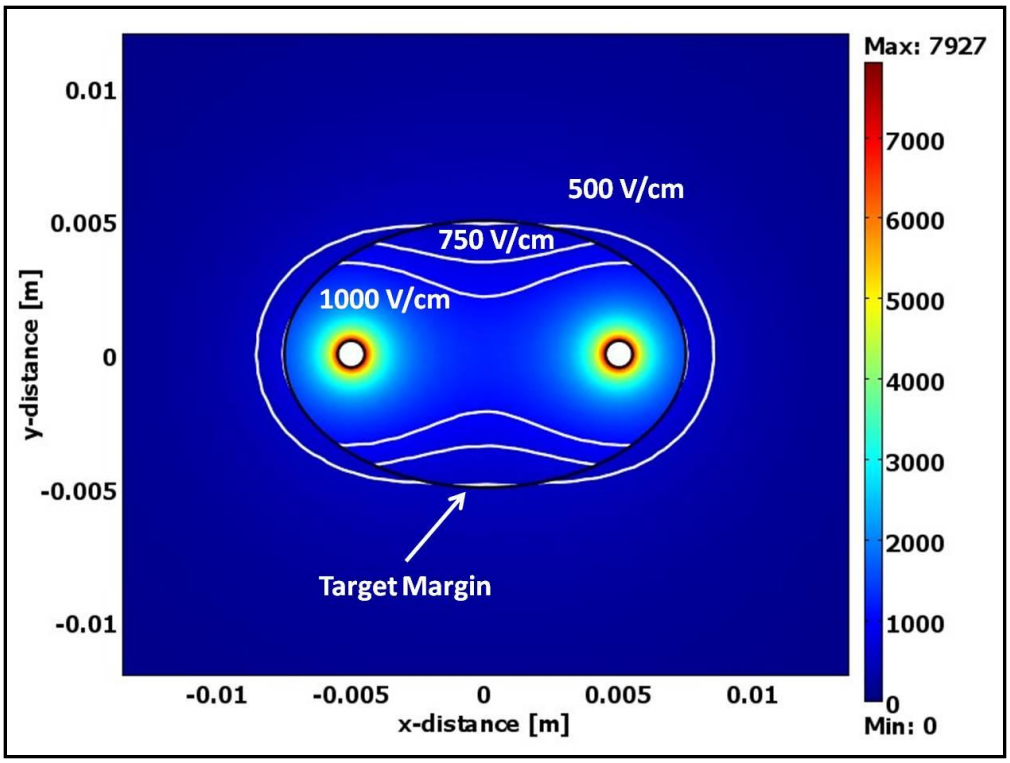

Figure 12: Electric field [V/cm] distribution using a 2000 V (50 µs) IRE pulse in heterogeneous tissue. The black line outlines the area to be treated with IRE $(2 \cdot \sigma_{target} = \sigma_{surrounding})$. Reprinted with permission from NOVA Science Publishers, Inc. as described in page 23.

3.4.3 Three Dimensional Electric and Temperature Distributions in Tissue

An additional comparison of numerical models explored between the two electrode geometries depicted in Figure 8 may be seen in Figure 13 using the joule heating term to observe changes in temperature. The images represent the electric field and temperature distributions of the two geometries at time t = 50 µs, during the application of a single IRE pulse. From Figure 13, it can be seen that large volumes of tissue may be treated with IRE-relevant electric fields (A) and (C); maintaining the same shape of distribution observed in Figure 9. Parts (B) and (D) shows the thermal effects and where they are most prevalent, which is at the edges of the energized surfaces. It should be noted that, although the thermal effects have been depicted to help visualize their distribution, the maximum temperature found at the end of the 50 µs pulse was only 43°C. This temperature is well below the range of thermal lesioning or scarring, typically taken to be 50°C [46]. Therefore, this figure demonstrates the significantly large volumes of tissue that may be treated by IRE without the occurrence of any considerable

thermal damage. This is in accord with previously published studies [1, 32, 36, 49, 143]. Higher energy applications (multiple pulses or longer pulses) will increase the temperature change. However, for most clinical application purposes, the volume of tissue undergoing thermal damage will typically never exceed 5% of the volume of tissue ablated by IRE. Further thermal damage assessment is possible by using the Pennes bioheat equation, calculating the equivalent thermal dose from an IRE treatment, or by assessing the thermal effects using the thermal damage equation as will be introduced in Chapter 4.

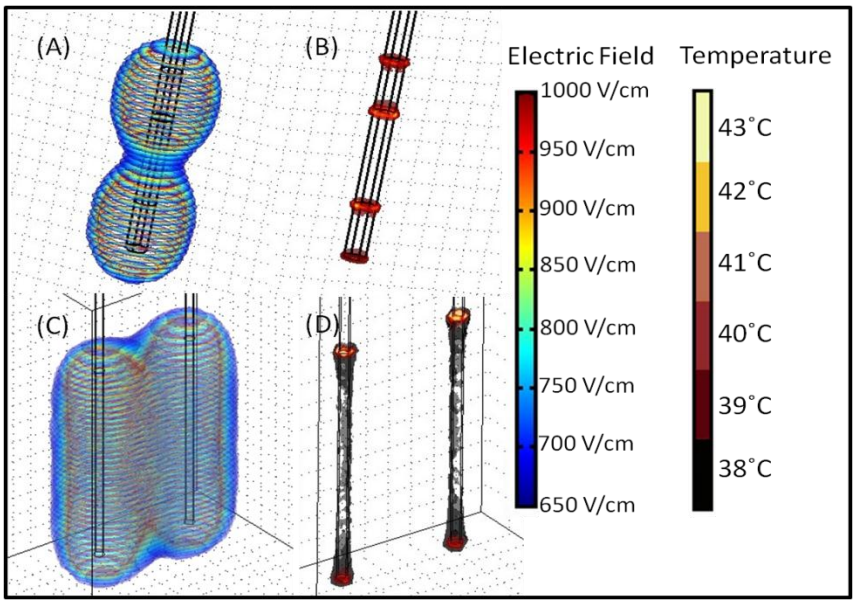

Figure 13: Electric field and temperature distributions for the bipolar (A,B) and monopolar electrodes (C,D). Parts A and C depict the electric field for IRE-relevant ranges from 650 to 1000 V/cm while B and D show the temperature region from 37°C to 43°C. Reprinted with permission from NOVA Science Publishers, Inc. as described in page 23.

3.4.4 Equivalent Thermal Dose

Figure 14 shows the equivalent thermal dose curves for the two monopolar electrode configuration described in Case B of Figure 8. The thermal dose was calculated for an eighty pulse (50 µs pulse length) IRE treatment at a frequency of 1 pulse per second using 1500, 2000 and 2500 V as the input voltage. Thermal doses were calculated along the electrode-electrode axis extending 10 mm to the left and right from the middle of the electrodes, as shown at the bottom of Figure 14. The highest thermal doses occurred at the electrode tissue interface because these locations experienced the maximum electric fields. However, at 2 mm from the interface the thermal dose decreases by a factor of 10 due to heat diffusion to areas of lower

temperature. Increasing the voltage results in more joule heating, as described in Equation 11. The 500 V intervals examined exhibited thermal doses that increased by roughly an order of magnitude each. Nevertheless, the thermal doses remained well below a typical thermal damage threshold of t_{43} = 120 min (7,200 s) that has been found for other soft tissues including breast and muscle for example [31, 79]. This shows that the temperature increase generated by the entire IRE procedure is not responsible for the tissue death.

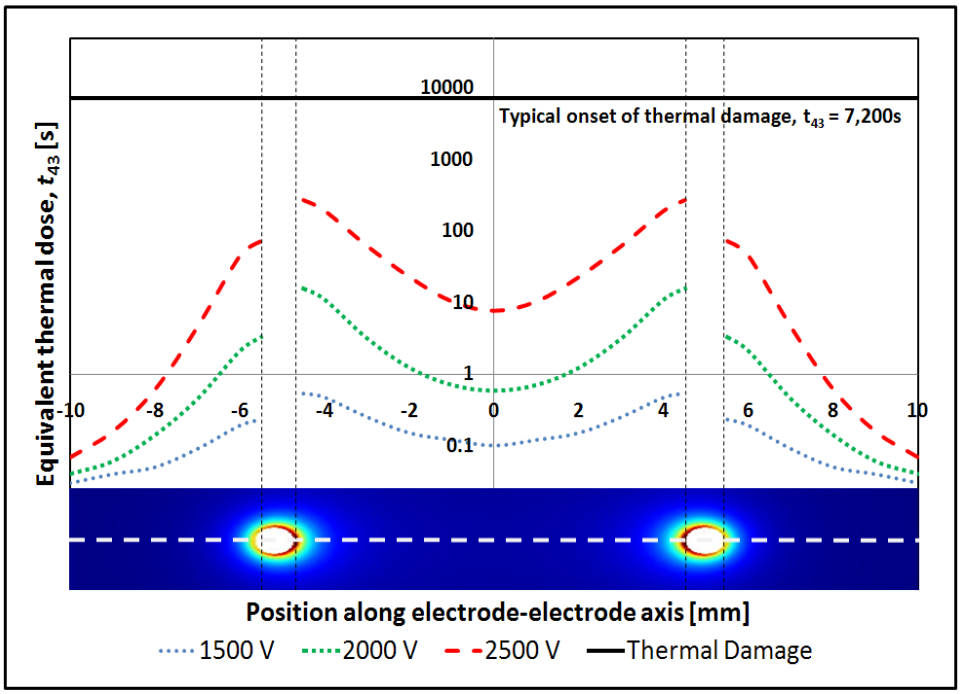

Figure 14: Thermal dose curve along the electrode-electrode axis for eighty (50 µs) pulses at a 1 Hz frequency for 1500, 2000 and 2500 V. Reprinted with permission from NOVA Science Publishers, Inc. as described in page 23.

3.5 CONCLUSION

This chapter focused on applying the basic principles involved in IRE therapies to facilitate accurate treatment planning for clinical therapies. Specifically we provide numerical methods for irreversible electroporation simulation in tissue with two different electrodes geometries, allowing for the generation of electric field and temperature distributions when the tissues are exposed to electric pulses typically used in IRE protocols. The chapter concludes by quantifying the thermal dose and ensuring that the levels don't exceed critical thresholds in order to maintain the benefits of a non-thermal IRE treatment.

CHAPTER 4 - EXPERIMENTAL RESULTS OF IRE IN *EX VIVO* CANINE BRAIN

4.1 INTRODUCTION

Electroporation uses short, pulsed electric fields to induce a cellular transmembrane potential that results in increased cellular permeability. When performed irreversibly, it results in cell death while leaving the extracellular matrix and other sensitive structures intact. These electric fields result in thermal effects to the affected tissues due to resistive heating. We measure this heating extent in an *ex vivo* canine brain by recording temperature changes in real time. Temperatures were measured at three locations near the electrodes. Thermal damage was evaluated using the Arrhenius equation. This study experimentally shows for the first time that typical electroporation protocols result in negligible thermal damage in the bulk of the tissue if the pulse protocol is chosen carefully. In addition, a numerical model for treatment planning was validated with the measured temperature in order to assess the possibility of thermal damage resulting from any given set of electric pulse parameters and electrode configuration.

4.2 BACKGROUND

IRE has proven to be an exciting, new, and effective anti-cancer treatment in the prostate, liver, kidney and lungs [156]. Due to immediate changes in the affected tissue's permeability, the treated regions may be monitored in real-time using conventional imaging techniques including ultrasound [110], MRI [61, 114], or electrical impedance tomography [32, 34]. Treatment may be administered through small needle electrodes, making the treatments minimally invasive [133, 143]. IRE therapies have been shown to leave the major blood vessels, extracellular matrix, and other sensitive tissue architecture intact, allowing for rapid lesion resolution and minimal scarring of the treated volume [121, 143, 155].

The main difference between IRE and other focal ablation techniques such as radiofrequency (RF) ablation [25, 144], high-intensity focused ultrasound (HIFU) [56, 119, 197], Laser Interstitial Thermal Therapy (LITT) [5, 115, 166] or cryoablation [180] is that the mechanism of cell death does not depend on thermal energy [33, 36]. In these thermal techniques, targeted regions are exposed to extreme temperatures in order to kill the tissue by

coagulation necrosis, cell death, or vascular stasis followed by ischemia [171]. Although these techniques are powerful, there are some challenges with their control including discrepancies between the predicted or visualized heated/cooled zone and true cell death regions [88, 159], and local heat and cold sink behavior of vascular perfusion that dissipates the thermal effects [78, 98]. Additionally, hyperthermic techniques that use increased temperatures for ablation produce significant scar tissue [88], which can complicate follow-up monitoring for tumor recurrence [58]. Because IRE technology uses lower energy than the previously mentioned procedures, it has been postulated that cell death is solely caused by altering the transmembrane potential of the cells exposed to electric fields, thus generating loss of cell homeostasis [193].

There have been several theoretical/numerical attempts in the literature to investigate the thermal response of tissues to IRE and other electroporation-based treatments [9, 36, 106, 112, 149, 184]. In some studies, the authors calculate the pulse time required to reach a maximum temperature of 50°C, which they assume is when thermal damage will occur [33, 37]. Others calculate the equivalent thermal dose or damage associated with one or multiple pulses (Arrhenius type analysis) to determine the amount, if any, of tissue damage due to exposure of the tissue to elevated temperatures [9, 36, 112, 184]. Finally, other papers show the equivalent thermal dose for an 80-pulse IRE treatment at a specific location [1, 9, 62]. Because electroporation based therapies require high-voltage pulses to be administered to the tissue, thermistors and thermocouples may become damaged during treatment. Therefore, these previous investigations have relied on numerical modeling, typically using a modified Pennes Bioheat equation with an added Joule heating term to predict the thermal effects resulting from IRE therapies. Although these theoretical analyses are very powerful and well-grounded, to the best of our knowledge, there is no experimental data for actual temperature changes during IRE pulse administration to prove the non-thermal nature for the mechanism of cell death other than a qualitative assessment by Pliquett et al. in which indirect surface thermal maps were generated with temperature-sensitive liquid crystals that turn red at 40°C, appear greenish-blue at 45°C and become dark blue at 50°C [149]. This data is vital in order to ensure that the temperature changes during a procedure do not generate thermal damage.

We hypothesize that IRE therapies do not result in sufficient temperature increases to induce significant thermal damage. This chapter validates the assertion that IRE therapies cause minimal thermal damage by experimentally measuring the changes in temperature from a typical therapeutic protocol administered on an *ex vivo* canine brain. Temperatures were measured at three locations before, during, and after pulse administration using a fluoroptic thermometer. From the measured data, the thermal damage was assessed according to methods described in [112, 171]. Using a typical IRE protocol, it was calculated that the thermal damage probability was at the most 0.649% from the measured temperature data assuming physiologically relevant conditions. Additionally, we created a numerical model that was validated by the measured experimental data. Using this model we were able to calculate a thermal damage distribution in the entire geometry in order to evaluate future IRE treatment protocols and prevent thermal damage using an Arrhenius type analysis by quantifying the volumes of affected tissue.

4.3 METHOD

4.3.1 Real-Time Temperature Measurements

The experimental study was performed on an *ex vivo* canine brain 4 hours post-mortem. By this time, the brain had reached equilibrium with the room temperature (21 °C). IRE pulses were delivered using the NanoKnife® (Angiodynamics, Queensbury, NY USA) pulse generator system, and two single needle electrodes. The electrodes were 1 mm in diameter with a sharpened tip. Two different IRE protocols were used, one in each of the cerebral hemispheres. The tips of the electrodes were placed 2.0 cm below the brain surface within the white matter. These anatomical locations were identical to previous *in vivo* studies that investigated the safety of intracranial IRE procedures [61]. Pulses were delivered in trains of 10 at a frequency of 1.5 Hz. Due to recharging demands of the capacitors, each train of pulses was delivered 3.5 seconds after the completion of the previous train for total treatment duration of 90 seconds. The protocols used are described in Table 1.

Table 1: Parameters used in the *ex vivo* brain treated with IRE.

VOLTAGE (V)	EXPOSURE LENGTH (cm)	SEPARATION DISTANCE (cm)	VOLTAGE-DISTANCE RATIO (V/cm)	PULSE DURATION (μs)	NUMBER OF PULSES	FREQUENCY (Hz)
1000	1.0	1.0	1000	100	9 x 10	1.5
2000	1.0	1.0	2000	100	9 x 10	1.5

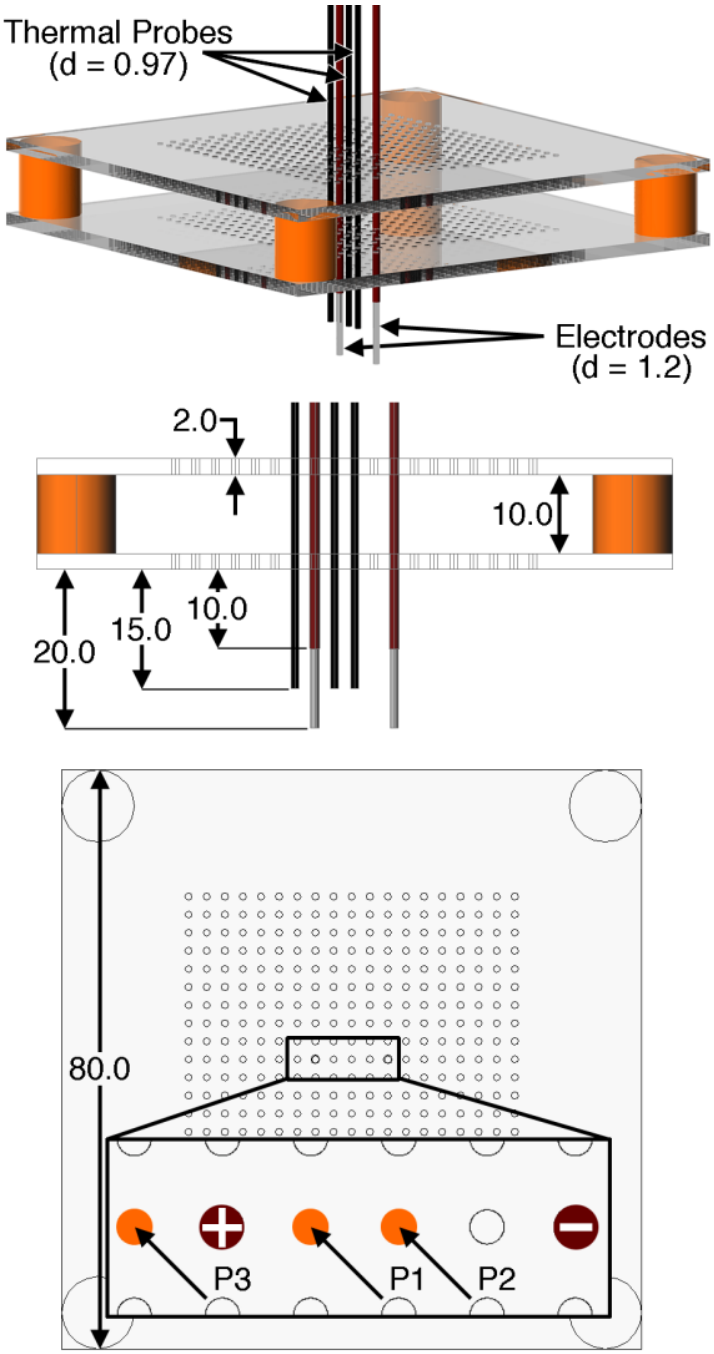

Figure 15: Schematic of the IRE probe placement device (Dimensions in mm). [Insert] Experimental placement of the probes (orange) relative to the electrodes (maroon).

Temperatures were measured in the brain during the experiment using the Luxtron® m3300 Biomedical Lab Kit Fluoroptic® Thermometer (LumaSense™ Technologies, Santa Clara,

CA USA). The probes consist of a fiberoptic cable terminated with a temperature sensitive phosphorescent sensor. Pulsed light strikes the phosphorescent element causing it to fluoresce. The decay time of this fluorescent signal is temperature dependant and is measured with an accuracy of ± 0.2 ˚C. Three STB medical fiber optic probes (LumaSense™ Technologies, Santa Clara, CA USA) were placed at specific locations in relation to one IRE electrode (±2.5mm and +5mm) using a custom-made probe placement device (Figure 15 and Figure 16). The depths of the probes and electrodes were set using stoppers. The thermal probes were inserted to a depth of 1.5 cm from the brain surface, along the centerline of the electrodes. From this depth, temperatures were measured at points in the middle of the exposed lengths of the electrodes. The data acquisition was performed with TrueTemp™ software (Version 2.0, Luxtron® Corporation, Santa Clara, CA USA) in which each probe was set to a recording frequency of 2 Hz.

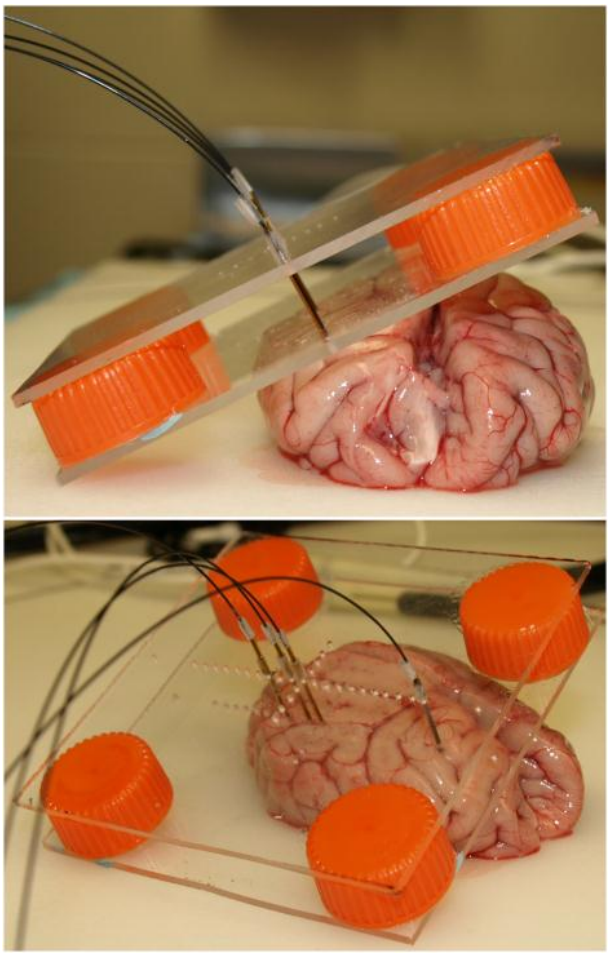

Figure 16: Probe placement and experimental setup for real-time temperature measurements. (Top) Front view and (Bottom) side view of the thermal probe insertions in brain using the custom-made placement device.

4.3.2 Thermal Damage Evaluation

Thermal damage occurs when tissues are exposed to temperatures higher than their physiological temperature for extended periods of time. If the period of exposure is long, thermal damage can occur at temperatures as low as 42°C. However, 50°C is generally chosen as the target temperature [46]. This damage can represent a variety of damage processes including cell death, microvascular blood flow stasis and/or protein coagulation [171]. The thermal damage can be calculated to assess whether a particular set of pulse parameters and electrode configuration will induce thermal effects in addition to IRE. The damage can be quantified using an Arrhenius type analysis which assumes that the damage follows first order reaction kinetics given by:

$$\Omega(t) = \int_0^{\tau} \zeta \cdot e^{-E_a/(R \cdot T(t))}\, dt \tag{16}$$

where ζ is the frequency factor, E_a the activation energy, R the universal gas constant, $T(t)$ is the temperature distribution and τ is the heating time [46, 54, 76, 158, 184]. The thermal damage index (Ω) is exponentially dependent on the temperature and linearly dependent on heating time. It is convenient to express the thermal damage index as a damage probability given by

$$Damage\ (\%) = 100 \cdot \left(1 - exp^{-\Omega(t)}\right) \tag{17}$$

Equation 17 calculates a damage probability of 0 % for an index $\Omega = 0$ and a damage probability of 99 % for an index $\Omega = 4.60$. The damage probability was calculated for the experimental data with the parameters from Table 2.

Table 2: Activation energy (E_a) and frequency factor (ζ) for thermal damage processes [171].

DAMAGE PROCESS	E_a [J mol^{-1}]	ζ [s^{-1}]	REFERENCE
Microvascular Blood Flow Stasis	6.670 x 10^5	1.98 x 10^{106}	[18]
Cell Death	5.064 x 10^5	2.984 x 10^{80}	[17]
Protein Coagulation	2.577 x 10^5	7.39 x 10^{37}	[86]

The temperature data from the experimental model was imported for analysis into Wolfram Mathematica 6.0 for students (Champaign, IL USA). The measured temperatures were scaled by 16°C for thermal damage calculations in order to match the typical *in vivo* canine physiological temperature of 37 °C. The highly oscillatory data was smoothed with the "MovingAverage" command in which each data point reported is the average of the neighboring 50 points. The smoothed data was then converted into a continuous mathematical function of time with the "Interpolation" command. The functions were evaluated numerically using Equation 17 to get the thermal damage probabilities.

4.4 RESULTS

The temperature distributions for both IRE protocols may be seen in Figure 17 where temperature was recorded for 30 seconds before to 360 seconds after IRE pulse administration in order to allow for heat dissipation. From these, an onset and logarithmic temperature increase of the brain tissue is seen during administration of the electric pulses, followed by an exponential decay after pulsing was completed. The maximum temperatures occurred at the end of the final pulse, when all the energy was deposited in the tissue. For the 1000 V/cm case, mild temperature changes were observed with a 2 °C maximum difference. The 2000 V/cm treatment showed a maximum difference of 11.2 °C. The minimum and maximum temperatures observed by all probes during the experiment may be seen in Table 3.

Table 3: Temperature extremes detected from the *ex vivo* IRE protocol.

PROTOCOL	TEMP. P1 [°C]	TEMP. P2 [°C]	TEMP. P3 [°C]
1000 V/cm - Min	21.3	21.3	20.4
1000 V/cm - Max	23.3	23.1	21.6
Difference	2.0	1.8	1.2
2000 V/cm - Min	21.1	20.9	20.4
2000 V/cm - Max	32.3	28.0	25.3
Difference	11.2	7.1	4.9

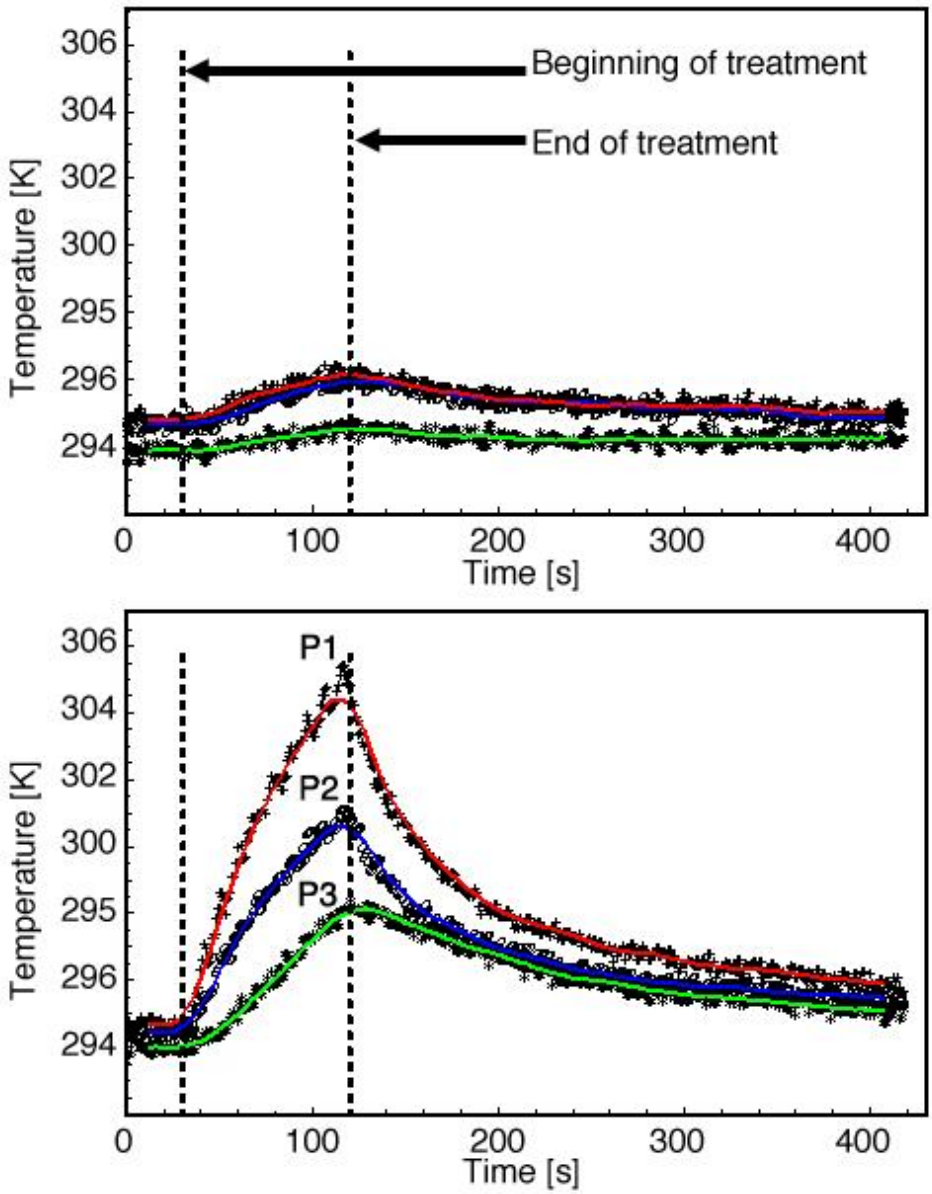

Figure 17: Temperature distribution in (top) 1000 V/cm (voltage-to-distance ratio) and (bottom) 2000 V/cm IRE protocols. The probes are located at a depth of 1.5 cm at known distances 2.5 mm (P1), 5 mm (P2) and -2.5 mm (P3) from the IRE electrode.

Although the maximum temperature ranges induced on the brain serve as a relative indicator of effects, it is desirable to calculate the percentage of thermal damage at each of these points from the various processes described in [112, 171]. These are tabulated in Table 4, where it can be seen that the maximum probability of combined thermal damage is 0.649%, and occurs for the 2000 V/cm protocol at probe 1.

Table 4: Thermal damage probability (%) for each location from the *ex vivo* IRE protocol.

DAMAGE PROCESS	LOCATION	1000 V/CM	2000 V/CM
Microvascular Blood Flow Stasis	P1	3.420E-04	4.788E-02
	P2	3.116E-04	3.466E-03
	P3	1.240E-04	8.820E-04
Cell Death	P1	1.751E-02	5.278E-01
	P2	1.632E-02	8.468E-02
	P3	8.171E-03	3.361E-02
Protein Coagulation	P1	1.888E-02	7.324E-02
	P2	1.823E-02	3.601E-02
	P3	1.289E-02	2.488E-02
Processes Combined	P1	3.674E-02	6.489E-01
	P2	3.496E-02	1.242E-01
	P3	2.118E-02	5.937E-02

4.5 VALIDATION OF NUMERICAL MODEL

The numerical model that was created to simulate the IRE treatment in the gray matter used the same methods described in Chapter 3 to generate the electric field and temperature distributions. The physical tissue properties were set to gray matter (Table 7 in page 69) and the perfusion and metabolic heat generation terms were neglected to mimic the *ex vivo* experimental conditions. Instead of modeling ninety individual pulses we modified the approach to have a continuous delivery of the electric field with the electrodes modeled as boundary conditions. This is important because there is no need to manipulate the time steps in order to ensure that microsecond pulses are captured by the solver every second as in the studied protocol. This in turn helps the simulation run much faster and smoother since there are no abrupt changes due to the pulses. In order to deliver the same amount of energy as in the pulsed approach, we multiplied the resistive heating by the duty cycle (duration/period) of the pulse in the tissue and insulation domains. This ensures that at the onset of each pulse, equal amount of energy have been deposited in the tissue in both approaches. Finally, by applying a continuous electric field, no thermal relaxation is allowed, which results in an upper limit (conservative estimate) for the resulting temperature in the tissue.

Due to the *ex vivo* nature of the experiment, no perfusion or metabolic heat generation terms were included in the simulation but all other pulse parameters and dimensions were identical to the experimental ones. Scaling the electrical conductivity 0.285 S/m (37°C) to room temperature (21°C) using the 3.2% $°C^{-1}$ resulted in a starting value of 0.1885 S/m for the tissue [48, 107]. A linear temperature relationship was used in order to account for the conductivity changes due to thermal effects using

$$\sigma(T) = \sigma_0[1 + \alpha(T - T_0)] \tag{18}$$

where σ_0 is the baseline conductivity, α the temperature coefficient, T the temperature, and T_0 the room temperature. The thermal boundaries of the brain domain and the electrodes were set to heat flux with a convective heat transfer coefficient of $h = 10\frac{W}{m^2K}$ and the insulation to continuity.

The default Comsol Multiphysics 3.5a (Stockholm, Sweden) "fine mesh" was used in the study and it was found that remeshing did not increase the accuracy of the solution by more than 1 %. The 3D simulation was constructed with pulses delivered every second in order to match the 90 s total treatment duration in the experimental portion. The "FGMRES" linear transient solver system and the "Algebraic Multigrid" preconditioner with "Free" time stepping were the solver parameters used to solve the simulation. In order to ensure that the solutions were smooth we used a relative (0.01 s) and absolute (0.001 s) tolerances that would ensure smooth solutions over the total simulation time. A time step of 0.1 s was used during both simulations and it was input in Comsol in the following manner: "range(0,0.1,90)" for the IRE treatments.

Figure 18 shows the simulated temperatures for the three identical locations (Figure 15 and Figure 17) in which we experimentally measured the temperature during the delivery of the IRE pulses. Specifically, Figure 18A and Figure 18B show the resulting temperature for the 1000 V and 2000 V treatment, respectively. The temperatures acquired in the simulation are slightly higher and have the same shape as the experimental data. Additionally, in Figure 18C we simulated the predicted treatment and thermal damage volumes using an electric field threshold for IRE of 500 V/cm. It is important to be able to visualize and understand the implications that thermal effects have on the evolution of the IRE treatments. In this last panel

one can appreciate that a 1000 V protocol can treat a volume approximately 1 cm^3 without any thermal damage when using ninety pulses (100 μs duration) delivered at 1 Hz. As in the experimental section, the resulting temperatures were scaled by 16 °C in order to have the initial temperature of the tissue match the physiological one. The 2000 V treatment is yet more interesting because it demonstrates the importance of incorporating thermal effects when modeling electroporation based therapies. In this case, there is a steady increase of the predicted treatment volume due to the higher temperatures and thus higher electric conductivities surrounding the electrodes. Finally, one can also see that starting at 60 s the thermal damage is acting in superposition with IRE and if the physician does not recognize this they can generate deleterious effects.

4.6 DISCUSSION

The results of this study confirm that the thermal effects induced by irreversible electroporation therapies are insufficient to induce significant thermal damage at the locations investigated. Although temperature increases are observed as a result of Joule heating due to pulse administration, the short duration of these pulses, their separation, and the brief overall period of typical irreversible electroporation treatments allows adequate time for heat to diffuse to their surroundings before the onset of damaging thermal effects. Nevertheless, it is imperative to incorporate the Arrhenius equation or some other mechanism of assessing thermal damage into the numerical models used to predict and plan IRE treatments.

There are several important observations to note from these results. Regarding IRE potential mechanisms, the maximum probability of combined thermal damage from the points evaluated is only 0.649%. Some of the other points used, such as P3 at 1000 V/cm, had probabilities of thermal damage that were an order of magnitude lower. The points and protocols evaluated are from tissue regions typically found to be ablated in IRE therapies. Therefore, it is reasonable to conclude that the vast majority of IRE induced cell death must result from non-thermal mechanisms, such as the proposed induced transmembrane potential from the applied external electric field. Since the voltage parameters (pulse number and strength) for reversible electroporation are typically lower than those for IRE, one would expect that the probability of thermal damage would be even lower than those reported here.

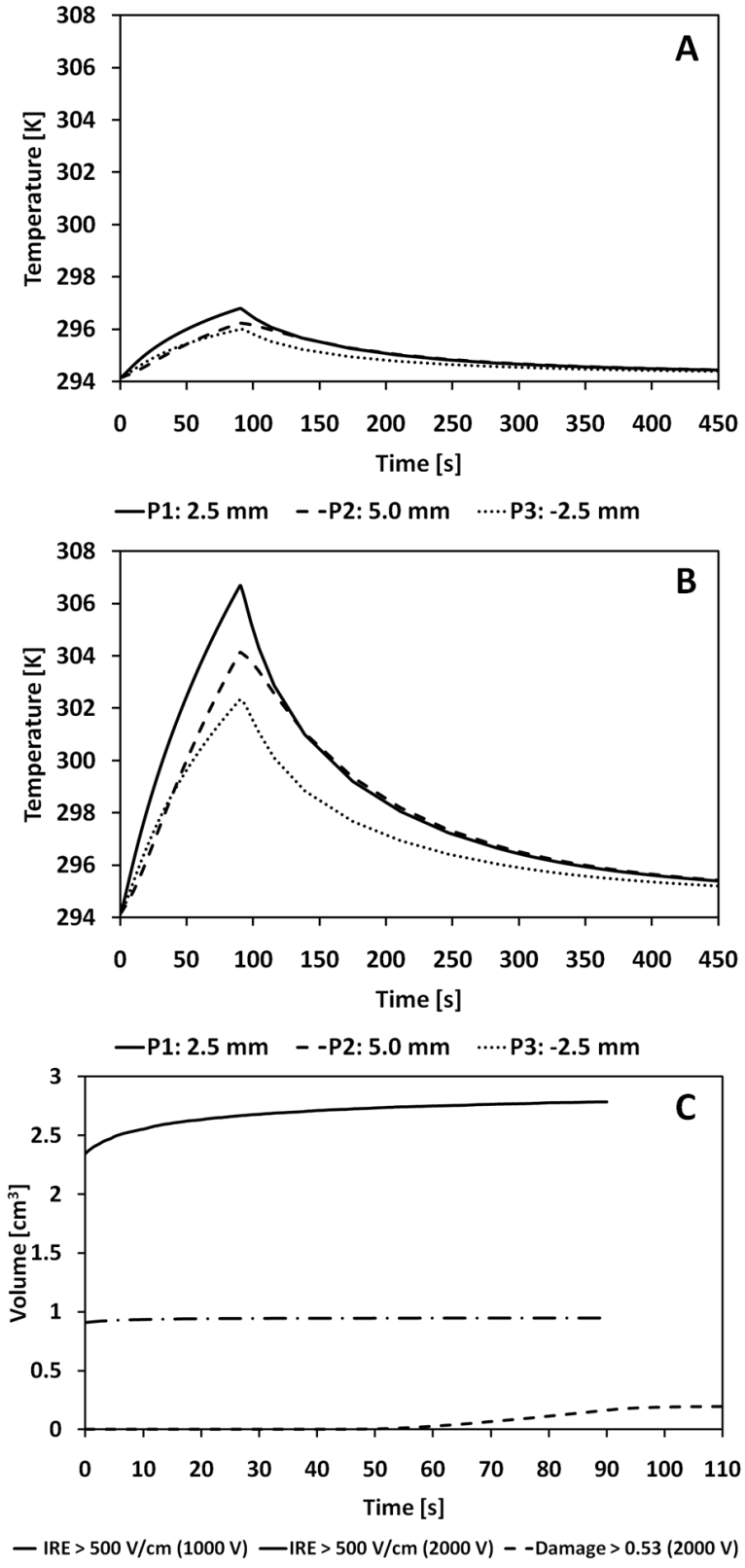

Figure 18: Numerical simulation of *ex vivo* brain using A) 1000 V and B) 2000 V with corresponding C) IRE treatment and thermal damage volumes from 90 pulses (100 us duration) at 1 Hz.

In accordance with typical thermal modeling studies, probes 1 and 2 (located between the electrodes) experienced a greater temperature change than probe 3 which was located outside [37]. This observation is important because typical IRE treatments involve placing electrodes within or around the targeted tissue. Therefore, any regions that do experience major thermal effects will likely be located within the tissue to be ablated, and such effects would be lower for the surrounding healthy tissue. Furthermore, the very low protein coagulation values calculated (0.073%) suggest that most thermal damage will not result in significant scar tissue. The same holds for thermally induced vascular stasis (0.048% maximum), which explains why IRE therapies do not permanently eliminate blood flow to the affected regions [121]. These behaviors are consistent with *in vivo* studies, which have shown rapid lesion creation and resolution (likely a result of adequate blood perfusion) that results in minimal scar tissue [143, 155].

There are several important limitations to this study when compared to an *in vivo* experiment or treatment. First, it must be noted that this study was performed on a brain *ex vivo*. This means that there was no metabolic heat generation or blood perfusion. The metabolic heat generation is typically eliminated by blood perfusion in a living being in accordance with maintaining homeostasis. However, blood perfusion results in dissipating the Joule heating more rapidly, reducing the duration of elevated temperatures, and thus the maximum temperature reached for any given region. Second, the brain used had been removed several hours prior to performing the experiments. As a result, some of the natural cell death processes would already have been in progress. This means that the tissue and cellular electrical and physical properties would have begun to change from that typical in living tissue [48]. The varying properties would affect the electric potential distribution and electrical conductivity, and thus Joule heating, as well as the brain's ability to conduct the heat away from the most affected areas. Furthermore, cellular and tissue property changes resulting from electroporation may be different as the tissue sits [168]. Third, the experiments were performed at room temperature. The electrical conductivity is dependent on the temperature by approximately 3.2% $°C^{-1}$ [48]. If these experiments were performed on a brain at its physiological temperature, then its conductivity would be higher, and the Joule heating would

be more significant. It should also be noted that thermal damage was evaluated by scaling the changes in temperature to a baseline temperature of 37˚C. True physiologic temperatures of different organs may vary from this baseline. In addition, it is common for patients undergoing procedures requiring anesthesia to experience a decrease in body temperature, which would reduce the thermal damage from the levels evaluated in this study.

Finally, this experiment used thermal probes placed at only 3 discrete points in a three-dimensional tissue. Therefore, we have only obtained observations for temperature effects and thermal damage at the observed locations. In accordance with the Joule heating term and previous work using numerical simulations to examine temperature changes [37], it is likely that Joule heating will be greatest at the electrode-tissue interface where the electric field is highest. The magnitude of this effect decreases rapidly from the surface of the electrodes. Because our thermal probes were placed along the center of the exposure length and the closest probes were 2.5 mm (center-to-center) from the electrode, it is reasonable to assume that we did not measure the most dramatic thermal effects. If the probes were placed closer to the electrode-tissue interface, higher percentages of thermal damage probability would likely be calculated. However, even when this is accounted for, it is unlikely that significant thermal effects would occur, as is consistent with the numerical studies [37]. Additionally, due to the nature of IRE treatments, where the electrodes are placed near or within the targeted tissue, these increased thermal damage probability regions would likely be constrained within the targeted tissue and any possible treatment margins.

Overall, this experiment has validated the assumption used in many previous irreversible electroporation investigations that the main effects to the tissue are non-thermal in nature [37]. Further investigation of this initial study will develop a numerical simulation of the experiment performed to ensure that the temperatures observed from the experiment match well with a numerical prediction. From this, the accuracy of such predictions may be determined as well as an understanding of which assumptions made in thermal studies are valid.

4.7 CONCLUSION

IRE therapies have proven to be an effective and beneficial focal ablation technique for the treatment of pathologic tissues such as tumors. To the best of our knowledge, all previous studies into the thermal effects of such treatments have been limited to numerical simulations. This study presents the first experiments to measure the temperature in tissue undergoing a typical IRE treatment protocol. It was found that the maximum temperature change in the tissue was 11.2˚C at the closest probe to the electrode, between the two electrodes. An analysis of thermal damage processes showed that, at this point, there was a combined thermal damage probability of only 0.649%, suggesting that even at the site of the greatest observed temperature changes, the thermal effects are negligible. We also provided a model that was validated by the temperature measured and that can be adapted to other IRE protocols for treatment planning and to prevent thermal damage. Therefore, it may be concluded that IRE therapies may be optimized using the numerical models presented in this Chapter in order to maximize the benefits and advantages of the non-thermal mechanisms of cell death.

CHAPTER 5 - SAFETY OF *IN VIVO* INTRACRANIAL IRREVERSIBLE ELECTROPORATION[3]

5.1 INTRODUCTION

This chapter presents the first systematic *in vivo* study of irreversible electroporation in canine brain tissue. Irreversible electroporation is a new non-thermal focal tissue ablation technique that uses low-energy electric pulses to destabilize cell membranes, thus achieving tissue death. The procedure is minimally invasive and is performed through small electrodes inserted into the tissue with treatment duration of about one minute. We confirmed that the procedure can be applied safely in the brain and was well tolerated clinically in normal dogs. The necrotic lesions created with irreversible electroporation were sub-millimeter in resolution, and sharply delineated from normal brain. The treatment also spared major blood vessels due to its non-thermal mechanism of tissue ablation. The minimal heat generation during treatment and sparing of major blood vessels may also make irreversible electroporation appropriate for treatment of tumors adjacent to, or enveloping critical vascular structures. Incorporating irreversible electroporation with current stereotactic guidance systems may also make it suitable for treating deep-seated, well-circumscribed brain tumors. We believe that irreversible electroporation will play a key role in the treatment of intracranial disorders in which the intent is to focally kill undesired tissue while minimizing damage to surrounding healthy tissue.

5.2 BACKGROUND

The destruction of tumors and other undesirable tissue through focal ablation has become an important, minimally invasive alternative to open surgery over the last several decades. Methods of tissue destruction include phototherapy [3], radiofrequency lesioning [25, 144], cryoablation [180], microwave ablation [145, 179], high-intensity focused ultrasound [56, 119, 197], and laser interstitial thermotherapy (LITT) [5, 115, 166]. Mechanisms of tissue destruction include changes in local temperature resulting in coagulation necrosis [55, 173] (radiofrequency lesioning, LITT, and high-intensity focused ultrasound) and cell membrane rupture [55] (cryoablation), generation of free-radicals (phototherapy) and *in situ* tissue fixation (microwaves) [145]. Each of these techniques has selective advantages when used in the brain.

[3] Chapter 5 was reprinted with permission from the American Association of Neurosurgeons (AANS) from: Nonthermal irreversible electroporation for intracranial surgical applications. J Neurosurg, 2010:(in print). Authors: Ellis, T.L., P.A. Garcia, J.H. Rossmeisl, N. Henao-Guerrero, J. Robertson, and R.V. Davalos,

Electroporation is a technique in which electrical pulses are used to permeabilize tissue, either reversibly or irreversibly, through formation of nanoscale openings in cellular membranes. Reversible electroporation has been used for years to facilitate genetic modifications of cell function via delivery of plasmid DNA, mRNA and macromolecules through the transient creation of nanopores within the cell membrane [52, 146, 157]. Reversible electroporation can also be used to increase permeability in order to allow delivery of cytotoxic agents for targeted cell death in a process referred to as electrochemotherapy (ECT) [42, 68, 75]. When the electric field strength is above a critical value, irreversible electroporation occurs and results in cell death due to loss of homeostasis [53]. Under most conditions, the irreversible increase in membrane permeability has been reported in conjunction with tissue thermal damage caused by electrical Joule heating [33, 112]. Joule heating is the dissipation of energy when an electrical current flows through a medium with resistance to that current. It is possible under certain conditions to permanently increase membrane permeability without thermal damage to the tissue [36] in a process referred to as non-thermal irreversible electroporation (IRE). IRE selectively disrupts cell membranes in non-CNS tissue, leading to the destruction of some, but not all tissues within the treated volume [36].

The exact mechanism of electroporation is unknown. Measurements of changes in membrane electrical properties [77, 95] and species transport across cellular membranes [135, 136] reveal that electroporation allows otherwise impermeant molecules to diffuse more freely through membranes. Although the precise mechanism by which electrical pulses permeabilize membranes is not known, it is believed that the potential induced across the membrane leads to instability in the lipid bilayer, resulting in a localized alteration of membrane shape into aqueous pores through which molecules can pass [24, 190]. While reversible electroporation has been used for decades [7, 27, 29, 127, 129, 135, 198] and knowledge of irreversible electroporation dates to the 1960's [161], the use of IRE *in vivo* as a method of tissue ablation was only recently reported [49]. A study in pig liver demonstrated that IRE protocols can be designed to destroy certain cells within the treated area while preserving major blood vessels

and duct scaffolds [155]. A study in dogs, revealed that IRE can produce focal tissue ablation in the prostate, while sparing the urethra [143].

This study reports the first *in vivo* experimental use of IRE to ablate normal brain. Five purpose-bred canines were used. Three dogs were subjected to IRE therapy at differing voltage configurations. Two additional dogs were used as control. In the fourth animal, two lesions were created to study the upper safety limit of the procedure. The fifth dog was used as a sham to isolate the tissue effects of electrode insertion without IRE treatment. The purposes of this study are to demonstrate that 1) IRE at certain voltages can be used safely to create lesions within the brain and 2) there is a trend between applied voltage and the lesion volume.

5.3 METHODS

The pilot study was approved by the Institutional Animal Care and Use Committee and performed in a Good Laboratory Practices (GLP) compliant facility. The dogs were systemically healthy and neurologically intact prior to the study, based on normal physical and neurologic examinations, results of complete blood counts, and serum biochemistry profiles. No abnormalities were detected on scalp-recorded electroencephalograms (EEG) and baseline magnetic resonance imaging (MRI) examinations of the brain. After administration of general anesthesia, neuromuscular blockade and an anti-convulsant (phenobarbital 6 mg/kg IV), routine craniectomies were performed to expose the right parietotemporal region of the brain of each dog. Focal ablative IRE lesions were created in the ectosylvian gyrus using blunt tip electrodes (Figure 19) attached to the NanoKnife® (Angiodynamics, Queensbury, NY USA). This device is an electric pulse generator in which the desired IRE pulse parameters can be programmed prior to administering a treatment. The design allows the user to monitor the resulting current from the treatment and to automatically suspend the delivery of the pulses if a current threshold is exceeded. The blunt tip electrodes are connected via a 6-foot insulated cable to the generator. The pulses are conducted from the generator to the tip of the electrodes after insertion into the tissue and upon activation of a foot pedal.

Figure 19: Blunt-tip dual probes insertion during the intracranial IRE procedure. Reprinted with permission from the American Association of Neurosurgeons as described in page 50.

For dog 1, a single probe with both an energized and ground contact was used at a depth of 2mm below the gyral surface. For the remaining test dogs smaller dual probes (one energized and the other grounded) were used at a depth of 7 mm below the gyral surface. The dual probes are similar in dimensions to those used in deep brain stimulation. IRE lesions were created by administering nine sets of ten pulses at a repetition rate of 4 Hz. The pulses were each 50 µs in duration and were configured with alternating polarity between each set to minimize total charge delivered to the brain. The pulse sets were delivered in 3.5 second intervals after the end of each pulse train. The strength of the electric field applied is dependent on the voltage configuration between the energized and ground electrodes. Values for each dog are given in Table 5. The voltage and pulse parameters were determined from the literature and from *ex vivo* experiments on canine brain [1, 49, 110, 143]. Using these parameters, the charge delivered during this study was typical of that used in humans during electroconvulsive therapy [87]. The animals were treated with 1600 V, 1000 V and 500 V, respectively in order to assess whether lower voltages could still produce neuronal ablation.

Table 5: Pulse parameters used in IRE brain treatment of canines.

DOG	BLUNT TIP ELECTRODES	ELECTRODE EXPOSURE [mm]	SEPARATION DISTANCE [mm]	VOLTAGE [V]	TOTAL ENERGY [J]	TOTAL PULSES	PULSE DURATION [µs]
1	SINGLE	7	8	1600	18.4	9 x 10	50
2	DUAL	5	5	1000	8.8	9 x 10	50
3	DUAL	5	5	500	0.8	9 x 10	50
4- Control	DUAL	5	5	1000	5.2	9 x 10	50
	DUAL	5	10	2000	39.4	9 x 10	50
5 - Control	DUAL	5	5	0	0	0	n/a

One control animal (Dog 4) was treated at a higher voltage to study the upper safety limit of the procedure. In this animal, two lesions were created using the dual electrode configuration at 1000 V and 2000 V. The last animal was used as a sham control to examine the physical effects of electrode insertion without the IRE pulses. Non-energized electrodes were advanced into the brain and maintained in place for approximately 30 s, the time required to deliver the IRE treatments in the other animals.

During the IRE procedure, each animal underwent intraoperative ultrasonography to assess the position and extent of the lesion created. Post-operatively, all animals underwent immediate MRI evaluation with and without contrast and then were recovered from anesthesia. A repeat MRI was then performed 48 h after the procedure on Dogs 2 and 3 to evaluate possible edema generation. Brain sections were then submitted from all dogs for histological analysis.

5.4 RESULTS

After the procedure, the animals were evaluated and treated in the standard fashion for post-craniectomy canine patients. There was no significant deterioration in neurologic ability or coma scale scores from baseline evaluations. The animals were able to ambulate and eat within 10 hours of the procedure, suggesting that lesioning was well tolerated. No seizures were observed. Analysis of the intra-operative ultrasound (Figure 20) obtained for each animal revealed a clearly demarcated hypoechoic zone with hyperechoic rim within the targeted brain parenchyma.

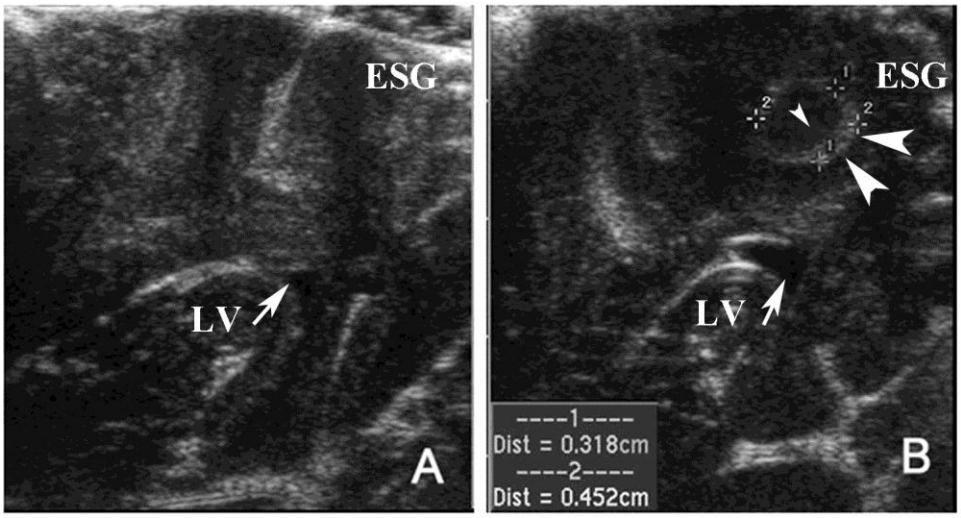

Figure 20: Ultrasound image of A) intra-operative pre-IRE treatment and B) 24 h post-IRE treatment in Dog 1. The IRE ablation zone is clearly visible as a well demarcated, hypoechoic circular lesion (small arrowhead) with a hyperechoic rim (large arrowheads). LV: lateral ventricle and ESG: ectosylvian gyrus. Reprinted with permission from the American Association of Neurosurgeons as described in page 50.

MRI examinations performed immediately post-operatively (Figure 21) reveal fluid accumulation within the ablation sites and a focal disruption of the blood-brain-barrier. These images also show that the IRE ablation zones were sharply demarcated and iso- to hypointense on T1 sequences, hyperintense on T2 sequences and peripherally contrast enhancing following intravenous administration of gadolinium. The 48 h post IRE MRI (Figure 22) demonstrates edema in the subcortical white matter adjacent to the zone of ablation. This edema was not associated with clinical effects in the dogs, and therefore was not specifically treated.

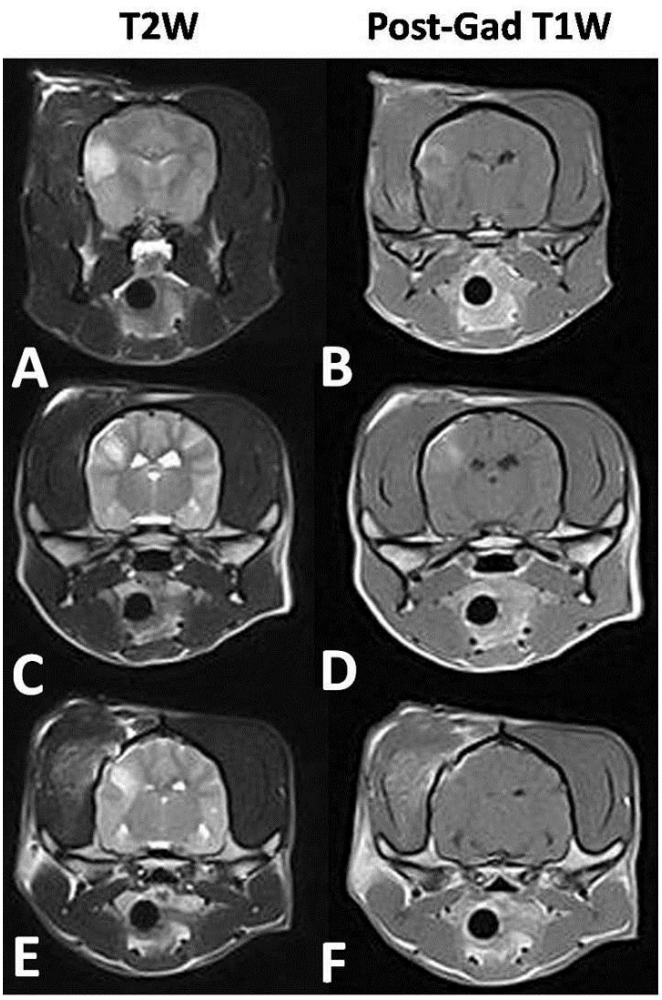

Figure 21: T2 weighted MRI immediate post-procedure for A) Dog 1 (1600 V – 8 mm electrode separation), C) Dog 2 (1000 V – 5 mm electrode separation), and E) Dog 3 (500 V – 5 mm electrode separation). T1 weighted + contrast MRI immediate post-procedure for B) Dog 1 (1600 V), D) Dog 2 (1000 V), and F) Dog 3 (500 V). Reprinted with permission from the American Association of Neurosurgeons as described in page 50.

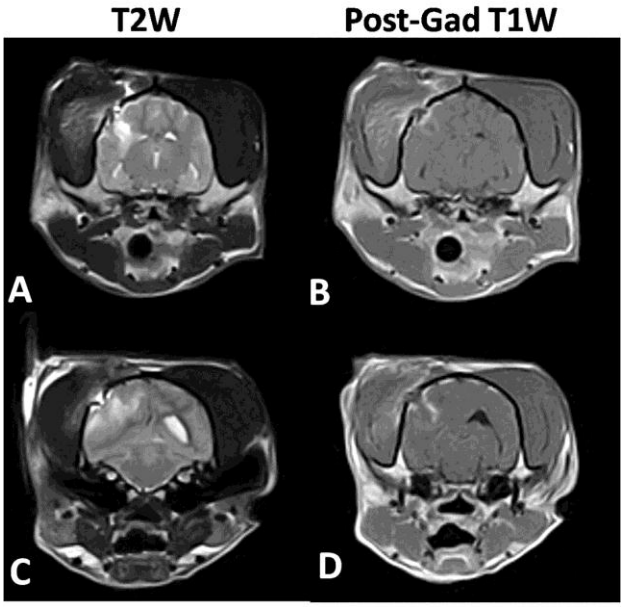

Figure 22: T2 weighted MRI 48h post-procedure for A) Dog 3 (500 V) and C) Dog 2 (1000 V). T1 weighted + contrast MRI 48 h post-procedure for B) Dog 3 (500 V) and D) Dog 2 (1000 V). All images correspond to a 5 mm electrode separation. Reprinted with permission from the American Association of Neurosurgeons as described in page 50.

The IRE lesion in the brain of Dog 1 was more superficial than the lesions in other animals, due to the electrode configuration used. In this animal, a single probe was inserted parallel to the surface of the brain at a depth of 2 mm. Grossly visible brain edema and surface blanching of the gyrus overlying the inserted electrode were observed within 2 minutes of completion of IRE procedure. This edema resolved completely following intravenous administration of 1.0 g/kg of 20 % mannitol. Because of these effects, the subsequent animals were treated with a smaller dual probe configuration with electrodes inserted perpendicular to the brain at a depth of 7mm. Brain edema and surface blanching were not observed during treatment of the remaining dogs.

The microscopic lesions from the histopathology correlated well with the gross appearance and MRI sequences in dogs 1-3. A histological comparison between the sham control and dog 3 (Figure 23) reveals that the isolated effect of electrode insertion is limited when compared to the IRE lesion. Histopathologic sections also demonstrate that the IRE lesions have a sub-millimeter line of demarcation (Figure 24A) between areas of necrosis and normal brain. The areas of treatment are represented by foci of malacia and dissociation of

white and grey matter. Small perivascular hemorrhages are present although there appears to be some sparing of major blood vessels (Figure 24B). High-voltage pulses in dog 4 were associated with non-selective coagulative necrosis of all tissues within the treatment field (Figure 24C), resulting in lacunar infarction secondary to arterial thrombosis. Moderate diffuse perivascular and intraglial edema, reactive gliosis, as well as death of neuronal and glial cells were also observed (Figure 25). The treatment area was moderately infiltrated with mixed inflammatory cells, including neutrophils, macrophages, plasma cells and small lymphocytes. Smaller lesions were observed when decreasing the voltage between dogs. As a result, customizing the pulse parameters should allow the ablation of volumes of varying sizes and shapes.

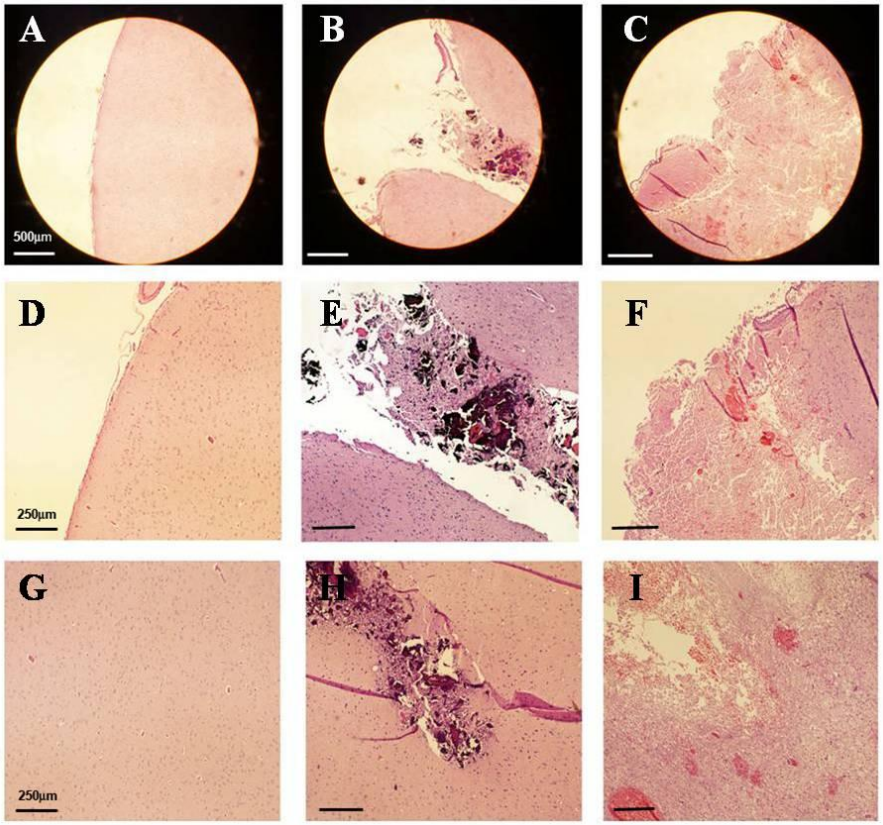

Figure 23: Hematoxylin and eosin stain of canine brain. Normal canine brain at A) 75X magnification (surface) D) 150X magnification (surface) and G) 150X magnification (deep). Sham study to isolate the mechanical effects of electrode insertion at B) 75X magnification (surface) E) 150X magnification (surface) and H) 150X magnification (deep). IRE effect on brain at C) 75X magnification (surface) F) 150X magnification (surface) and I) 150X magnification (deep). The white bars represent 500 µm and the black bars represent 250 µm. Reprinted with permission from the American Association of Neurosurgeons as described in page 50.

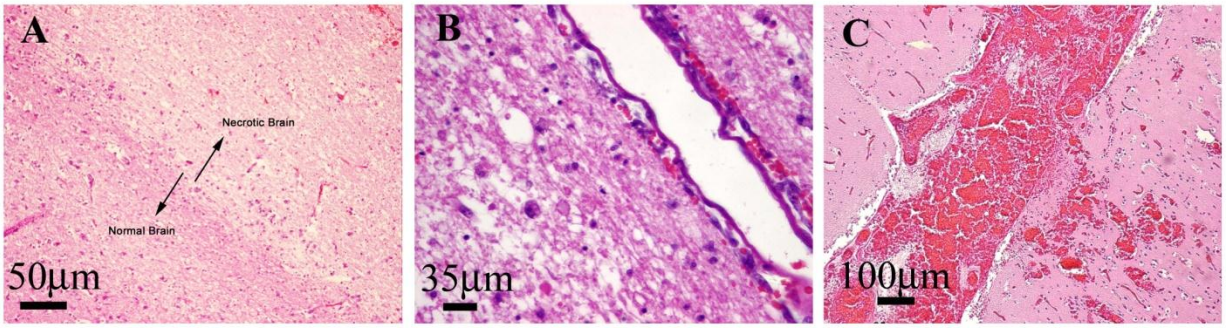

Figure 24: Hematoxylin and Eosin stain of IRE treated brain demonstrating the A) very sharp (50 µm) transition zone between necrotic and normal tissue and B) the sparing of major blood vessels (35 µm). C) In dog 4 a thrombus was detected (100 µm). Reprinted with permission from the American Association of Neurosurgeons as described in page 50.

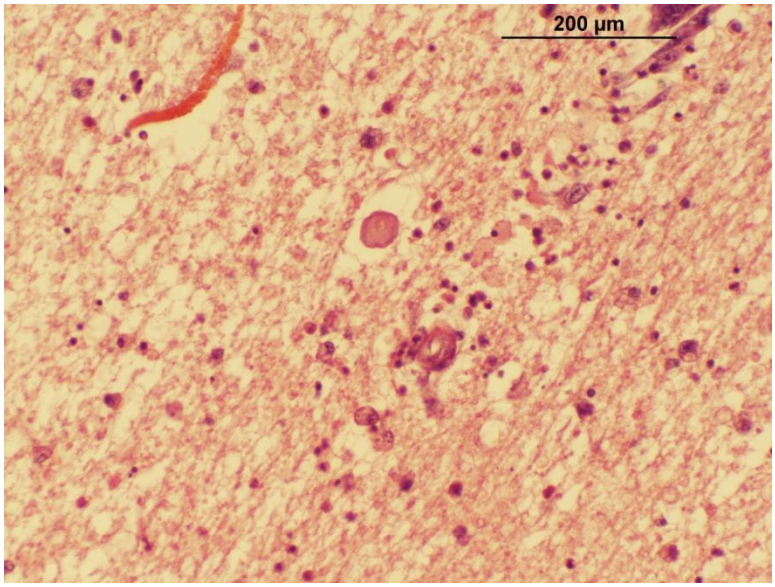

Figure 25: In this section of brain, taken at the site of IRE treatment, there is moderate diffuse perivascular and intraglial edema, as well as death of neuronal and glial cells. Modest reactive gliosis is seen. The treatment area is infiltrated with mixed inflammatory cells, including neutrophils, macrophages, plasma cells and small lymphocytes. This section is representative of the IRE treatment area. (Hematoxylin-eosin stain; original magnification 40 X). Reprinted with permission from the American Association of Neurosurgeons as described in page 50.

5.5 DISCUSSION

IRE is a promising new technique for the ablation of tissue and tumors [1, 49, 110, 143]. A historical review by Rubinsky [154] reveals that the first published reports documenting electroporation were written at the beginning of the 20th century and that the phenomenon

may have been observed as early as the mid 18th century. The first methodical studies describing electroporation in amphibian nervous tissue [57, 174] arose in the 1950's. In a pivotal publication subsequent to this, Sale and Hamilton [161] described the lethal effect of non-thermal electrical fields applied to cells and organisms in suspension. The ability of cellular membranes to recover from milder electrical pulses in what is now called "reversible electroporation" was first elucidated in the 1970's [7, 66, 94]. In 1993, Salford *et al*. first reported on the combined use of electropermeabilization and bleomycin in a rodent glioma model, demonstrating a doubling in survival time compared to animals treated with bleomycin alone [162].

To irreversibly electroporate cell membranes, the electric field in the targeted region needs to be above a critical value, which is dependent on a variety of conditions such as tissue type and pulse parameters (amplitude, duration, frequency, and number) [50]. Under most conditions, the electric field required to produce irreversible electroporation is associated with significant tissue heating and thermal damage. Davalos, Mir, and Rubinsky demonstrated however, that certain pulse parameters can produce irreversible electroporation without thermal damage, and that IRE can be used to destroy substantial volumes of tissue *in vivo* [36]. Since then, researchers have demonstrated the use of IRE in small and large animal models in the liver [49, 110] and prostate [143], and on implanted mouse sarcomas [1]. Because of the non-thermal mechanism, IRE can preserve the extracellular matrix, axons, and major blood vessels in non-CNS tissues [143, 154]. Furthermore, the procedure can be monitored in real-time using ultrasound and confirmed with both ultrasound and MRI [110, 112, 155]. In IRE studies outside the CNS, ablation is rapid in onset and resolution, allowing early repopulation of the ablated region with healthy cells [143, 154]. Although treatment success is not dependent upon the immune system, a tumor specific immune response appears to occur [143].

This chapter describes the first systematic *in vivo* study of IRE for intracranial surgery. Focal lesions were created in the right parietotemporal lobe of dogs using blunt tip probes. Pulse durations (50 μs) shorter than those described in previous studies [1, 49, 110, 143] were used in order to reduce the charge delivered to the tissue and to minimize the heating generated by the procedure. The ablation was confirmed with histopathological analysis,

revealing a sub-millimeter boundary between the necrotic and normal brain. Reconstructed lesion volumes of 1.655 cm^3, 0.599 cm^3, and 0.258 cm^3 were calculated from the post-operative MRIs. The accuracy of the computed lesion volumes was limited to the interval between the MRI scans (2.5 – 3.0 mm). It is important to note that the volumes of the lesions were reconstructed from MRIs taken within 60 minutes after pulse administration, so the observed ablation volume is likely to be that resulting from immediate IRE induced cellular necrosis. This means that any additional cellular death resulting from late-onset apoptosis may not be taken into account in the electric field correlation. However, we have extensive pathological, immunohistochemical, and ultrastructural data obtained 72 hours post-intracranial IRE from three canines (data not shown) which clearly demonstrates that by this time point, necrotic cell death is present. Furthermore, no significant differences in immunoreactivity to bcl-2, caspase-3, or caspase-9 were observed relative to untreated control brain tissue. This data suggests that the primary mechanism for cell death in these brain lesions was necrosis, and that later onset apoptotic regions should not significantly alter the lesion volumes measured immediately after treatment.

IRE treatments are dependent on the tissue of interest and the pulse parameters need to be selected correctly for complete focal ablation. Tissue heterogeneities (gray vs. white matter) are of particular interest in the application of IRE for brain cancer and future modeling studies will incorporate these effects on the resulting lesion volumes. Future work will also investigate the effects of IRE in different brain tissue states (e.g. healthy vs. tumor) and brain tumor types, in the effort to enhance tissue selectivity. In addition, we plan to investigate the effect of pulse number and frequency on the IRE lesion volume. At this point it is unclear whether one application of IRE pulses is sufficient for a successful treatment or if multiple applications are needed in order to cover a volume of interest. Numerical models will have to be developed to establish the parameters needed to predict manageable IRE lesion volumes. At that point, this technology may be applicable for intracranial surgical applications in which ablation of a defined volume of brain parenchyma is desired.

Our results support the hypothesis that IRE can be used safely in the brain and that lesion volume can be correlated with applied voltage. Future studies in an experimental rodent population will focus on the use of IRE for the ablation of brain tumors. In this canine study, as in other studies of soft-tissue organs, IRE associated edema developed following treatment. Although the vasogenic edema observed on the MRI of dogs in this study was not associated with any clinical deterioration, it is a cause of concern. Brain edema after IRE should be anticipated and treated with perioperative corticosteroids.

Although the results presented are preliminary, IRE may offer an advantage over surgical resection for selected brain tumors. The small electrode size makes the procedure minimally invasive and adaptable to virtually any neuroanatomic location with existing stereotactic guidance systems. IRE creates a sharply delineated volume of ablated tissue with sub-millimeter resolution that may make it suitable for treating deep-seated, well-circumscribed brain tumors. The minimal heat generation during treatment and sparing of major blood vessels may also make it appropriate for tumors adjacent to, or enveloping critical vascular structures.

In studies outside the nervous system, IRE produces a penumbra of non-destructive increase in membrane permeability beyond the zone of tissue ablation [36]. It is unclear at this time whether this phenomenon occurs in the brain or in brain tumors. Future efforts within our group will explore this question to determine if the delivery of chemotherapy or other cytotoxic agents can be enhanced in reversibly electroporated areas of infiltrative brain tumors. Determining the extent of any reversible electroporation as well as the minimal electric field threshold necessary to achieve it will be critical for development of a paradigm to plan and treat brain tumors, especially high grade gliomas.

5.6 CONCLUSION

This chapter evaluated the safety of an IRE procedure to lesion normal canine brain tissue. The IRE procedure involved placing electrodes into a targeted area of brain in three canines and delivering a series of short and intense electric pulses. The voltages of the pulses applied were varied between dogs. One additional dog was treated at an extreme voltage to determine the upper safety limits of the procedure. Ultrasound was used at the time of the

procedure to determine if the lesions could be visualized intra-operatively. The volumes of ablated tissue were then estimated on post-procedure MRI. Histological brain sections were then analyzed to evaluate the lesions produced. The animals tolerated the procedure with no apparent complications except for one animal treated at the upper voltage limit. Lesion volume appeared to decrease with decreasing voltage of applied pulses. Histology revealed cell death within the treated volume with a sub-millimeter transition zone between necrotic and normal brain. Our results reveal that IRE at selected voltages can be safely administered in normal canine brain and that the volume of ablated tissue correlates with the voltage of the applied pulses. This preliminary study is the first step towards using IRE as a brain cancer treatment.

CHAPTER 6 - PHYSICAL ANALYSIS OF *IN VIVO* IRREVERSIBLE ELECTROPORATION IN BRAIN[4]

6.1 INTRODUCTION

Irreversible electroporation (IRE) is a new minimally invasive technique to treat cancer. It is unique because of its non-thermal mechanism of tumor ablation. Intracranial IRE procedures involve placing electrodes into the targeted area of the brain and delivering a series of short and intense electric pulses. The electric pulses induce irreversible structural changes in cell membranes, leading to tissue death. This chapter correlates IRE lesion volume in normal brain tissue with electric field distributions from comprehensive numerical models. The electrical conductivity of brain tissue was extrapolated from the measured *in vivo* data and the numerical models. Furthermore, this preliminary study provides some of the necessary numerical tools for using IRE as a brain cancer treatment. Using this, we present results on the electric field threshold necessary to induce IRE lesions (495 V/cm – 510 V/cm) in canine brain tissue using ninety 50 μs pulses at 4 Hz. We also computed the electrical conductivity of brain tissue from the *in vivo* data (0.12 S/m - 0.30 S/m) and provide guidelines for treatment planning and execution. Knowledge of the dynamic electrical conductivity of the tissue and electric field that correlates to lesion volume is crucial to ensure predictable complete IRE treatment while minimizing damage to surrounding healthy tissue.

6.2 BACKGROUND

Irreversible electroporation (IRE) is a promising new technique for the non-thermal ablation of tissue and tumors [1, 36, 49, 154]. This minimally invasive procedure involves placing electrodes into or around a targeted area and delivering a series of short and intense electric pulses to induce irrecoverable structural changes in cell membranes, ultimately resulting in the death of the cell [155]. To achieve IRE, the electric field in the targeted region needs to be above a critical value, which is dependent on a variety of conditions such as tissue properties, electrode configuration and pulse parameters including strength, shape, duration, number, and repetition rate [36, 50, 120]. However, for a specific tissue type and set of pulse conditions, the primary parameter determining the extent of electroporation is the local

[4] Reprinted with kind permission from Springer Science + Business Media: J Membrane Biol, Intracranial Nonthermal Irreversible Electroporation: *In vivo* Analysis, 236(1):127-136, 2010. Authors: Garcia, P.A., J.H. Rossmeisl, R.E. Neal II, T.L. Ellis, J. Olson, N. Henao-Guerrero, J. Robertson, and R.V. Davalos.

electric field to which the tissue is exposed [126]. Davalos, Mir, and Rubinsky demonstrated that IRE can be used to destroy substantial volumes of tissue *in vivo* [36]. Following this, several researchers have confirmed the use of IRE in small and large animal models in the liver [49, 110], the prostate [143], and on implanted mouse sarcomas [1] using a variety of pulse parameters.

One advantage of IRE over other focal ablation techniques is the ability to destroy tissue through a non-thermal mechanism. As a result, it is possible at certain electric field intensities to kill the cells while preserving the extracellular matrix, axons, major blood vessels, and other sensitive tissues, thereby enhancing treatment outcome [143, 154]. The ablated volume can be predicted using numerical modeling for accurate treatment planning [126, 147]. Researchers have shown that conductivity changes due to electroporation and Joule heating can be incorporated to produce more accurate predictions of treatment outcome [34, 83, 84, 147, 167, 168]. Furthermore, the procedure can be monitored in real-time using ultrasound and treatment outcome can be confirmed with ultrasound, CT and MRI [61, 110, 112]. Previous IRE studies outside the central nervous system (CNS) have shown that ablation is rapid in onset and resolution, allowing early repopulation of the ablated region with healthy cells [143, 155]. Although treatment success is not dependent upon the immune system [2], a tumor specific immune response may be invoked [143].

Due to the aforementioned advantages, in conjunction with short treatment time and the minimally invasive nature of the treatments, we hypothesize that IRE can be an effective brain cancer treatment. In order to allow for predictable and effective therapy, planning future brain cancer IRE treatments require accurate knowledge of the electric field intensity needed for brain tissue ablation and the electrical conductivity of the tissue. In this study, we used numerical models to correlate a reconstructed IRE lesion volume in gray matter to an electric field distribution. Finite element software was used to develop a model capable of accounting for temperature and electroporation effects on brain tissue conductivity. This model was solved for the electric field distribution, which was used to correlate an electric field threshold for IRE lesions. Incorporating the conductivity dependency from electroporation and thermal effects provides a more accurate electric field-lesion correlation.

IRE lesions were generated within the ectosylvian gyral surface region of the brain in two canines. The resulting lesion volumes were reconstructed from 0.2 T and 7.0 T MRIs. These volumes were used with our revised numerical model to determine IRE electric field thresholds. In addition, the current and voltage data from the procedure were used to determine the bulk tissue baseline conductivity, σ_0, of gray matter for IRE-relevant procedures. The electrical conductivity determines the electric field distribution, current, and thermal effects from an IRE procedure. The results of this study can be used to improve treatment planning for patients using IRE for the ablation of brain tumors.

6.3 METHODS

This pilot study was approved by the Institutional Animal Care and Use Committee and performed in a Good Laboratory Practices (GLP) compliant facility at the Virginia – Maryland Regional College of Veterinary Medicine as described in Chapter 5. Following the creation of a rostrotentorial craniectomy defect in 2 canines, focal ablative IRE lesions were created in the cerebral cortex using the NanoKnife® generator (Angiodynamics, Queensbury, NY USA) with blunt tip probes. The probes are 1 mm in diameter and surrounded by an insulating sheath, where 0.5 cm long exposed tips were in contact with the tissue. These dimensions are smaller than the typical 1.27 mm in diameter commercial electrodes used in deep brain stimulation (DBS). Two probes (one energized and one set to ground) were used at a depth of 7 mm below the ectosylvian gyral surface, a non-eloquent region of the brain. IRE lesions were created using delivery criterion programmed into the NanoKnife®, where nine sets of ten pulses at a frequency of 4 Hz were administered. Due to recharging demands of the capacitors, the sets were separated by 3.5 seconds. The pulses were each 50 µs in duration and were configured with alternating polarity between each set to minimize charge build-up on the electrode surface. The pulse parameters used are given in Table 6. These pulses are in the lowest spectrum of the charge delivered to humans during electroconvulsive therapy which typically varies between 0.5 mC and 512 mC [87].

Table 6: Pulse parameters used in IRE brain treatment of canine.

DOG	ELECTRODE EXPOSURE [mm]	SEPARATION DISTANCE [mm]	VOLTAGE [V]	VOLT-TO-DIST RATIO [V/cm]	TOTAL PULSES	PULSE DURATION [μs]
1	5	5	1000	2000	9 x 10	50
2	5	5	500	1000	9 x 10	50

After the administration of the IRE pulse train, intraoperative ultrasonography was used to assess the position and extent of the lesion created. Post-operatively, the animals underwent immediate MRI evaluation with and without contrast and then were recovered from anesthesia. Open source image analysis software (OsiriX, Geneva, Switzerland) was used to calculate the IRE focal ablation volumes. The lesions were traced in each of the 2-D post-operative MRI scans and a solid 3-D representation of the IRE lesion volume was generated as in [61]. A high-resolution (7.0 T) *ex vivo* MRI, which scans every 300 μm, was also used for the second dog in order to attain a more accurate IRE lesion reconstruction with the same IRE procedure.

Numerical modeling can be used to predict the electric field distribution, and thus IRE treatment regions in tissue [50, 126, 147]. This has been chosen as the method to correlate lesion volume with an effective electric field threshold for IRE in brain. The methods for predicting IRE areas are similar to the ones described by Edd and Davalos [50]. The mathematical models were solved using a commercial finite element package (Comsol Multiphysics, v.3.5a, Stockholm, Sweden). The brain was modeled as a 7.0 cm x 5.0 cm x 5.0 cm ellipsoid with the electrodes inserted to a maximum depth of 0.7 cm. The electric field distribution is given by solving the Laplace equation:

$$\nabla \cdot (\sigma \nabla \varphi) = 0 \tag{19}$$

where σ is the electric conductivity of the tissue and φ is the potential. Because electrode placement resulted in the electrodes being surrounded mainly by gray matter, homogeneous physical properties were set to those of gray matter (Table 7). The electrodes were modeled as an insulating body with an extension of stainless steel. The electrical boundary condition along the tissue that is in contact with the energized electrode is $\varphi = V_o$. The electrical boundary condition at the interface of the other electrode is $\varphi = 0$. The boundaries where the analyzed domain is not in contact with an electrode are treated as electrically insulative.

Conductivity changes due to electroporation and temperature have been modeled to calculate the dynamic conductivity according to the following equation:

$$\sigma_{dynamic}(normE\_dc, T) = \sigma_0[1 + flc2hs(normE\_dc - E_{delta},\ E_{range}) + \alpha(T - T_0)] \quad (20)$$

where σ_0 is the baseline conductivity, α the temperature coefficient, T the temperature, T_0 the physiological temperature (37°C). The numerical model incorporates the change in conductivity within a pulse resulting from the increased permeabilization to ions presumably associated with the creation of pores in the cell membrane [85]. We assumed that once the conductivity increased due to electroporation it would not revert back. This process was repeated iteratively for each of the ninety pulses that were delivered in the experimental procedures. The $flc2hs$ is a smoothed heavyside function with a continuous second derivative that ensures convergence of the numerical solution. This function is defined in our numerical software (Comsol Multiphysics, v.3.5a, Stockholm, Sweden) and it changes from zero to one when $normE\_dc - E_{delta} = 0$ over the range E_{range}. In the function, $normE\_dc$ is the magnitude of the electric field, and E_{delta} is the magnitude of the electric field at which the transition occurs over the range, $\pm E_{range}$. In the simulations, we used $E_{delta} = 580$ V/cm and $E_{range} = \pm 120$ V/cm in order to match the average brain tissue parameters used by Sel *et al*. [147, 167, 168], where conductivity doubled due to electroporative effects between 460 V/cm and 700 V/cm. It should be noted that the thermal effect on conductivity was only taken into consideration when the electric field was below 460 V/cm since we assumed that the conductivity change due to electroporation already incorporates this dependency. Future research needs to determine the brain tissue conductivity as a function of applied electric field and temperature changes for a more refined IRE treatment model.

To determine baseline conductivities for the two dogs used in this study, we matched the *in vivo* current measured by the NanoKnife® (resolution: ± 0.2 A) during a typical pulse to the current of the numerically modeled IRE treatments. We used the current measured after the transient membrane charging effects had settled within the pulse. These conductivity values (Table 8) were determined by integrating the current density over the electrode surfaces and are within the expected ranges found in the literature [107, 168]. The baseline

conductivities were used with the dynamic conductivity function to simulate the complete ninety-pulse IRE treatments.

Heating of the tissue resulting from the procedures was done by modifying the Pennes Bioheat equation with the additional Joule heating term, as described in Chapter 3 [33, 37]. The joule heating term was zero when the pulses were off and only heat diffusion, blood perfusion and metabolic heat generation were involved in the heat transfer. Table 7 describes the physical parameters used in this study. The entire tissue is set to the initial physiologic temperature of the dogs measured prior to pulse administration: T(x,y,z,0) = 36.1 °C and 36.8 °C for the 500 and 1000 V treatments, respectively. The electrode/tissue interface is set to continuity. The outer surface of the analyzed brain domain is mathematically considered to be thermally insulative and a proportional loss due to convection with $h = 10\ W/(m^2 \cdot K)$, was set at the boundary of the electrodes exposed to air as in [106] with $T_\infty = 23$ °C. The initial temperature distribution of the brain and electrodes was allowed to reach equilibrium before the onset of the treatment to provide an accurate temperature distribution from the IRE pulses.

Table 7: Physical properties used in the numerical simulations.

MATERIAL	QUANTITY	UNITS	VALUE	REFERENCE
Brain	α, temperature coefficient	$°C^{-1}$	0.032	[48]
	k, thermal conductivity	$W\ m^{-1}\ K^{-1}$	0.565	[48]
	c_p , heat capacity	$J\ kg^{-1}\ K^{-1}$	3680	[48]
	ρ , density	$kg\ m^{-3}$	1039	[48]
	q’’’, metabolic heat generation	$W\ m^{-3}$	10437	[196]
Blood	c_b , heat capacity	$J\ kg^{-1}\ K^{-1}$	3840	[196]
	ρ_b , density	$kg\ m^{-3}$	1060	[185]
	w_b , perfusion rate	s^{-1}	7.15E-3	[185]
Insulation	σ, electrical conductivity	$S\ m^{-1}$	1.0E-5	[26]
	k, thermal conductivity	$W\ m^{-1}\ K^{-1}$	0.01	[26]
	c_p , heat capacity	$J\ kg^{-1}\ K^{-1}$	3400	[26]
	ρ , density	$kg\ m^{-3}$	800	[26]
Stainless	σ, electrical conductivity	$S\ m^{-1}$	2.22E6	[1]
Steel	k, thermal conductivity	$W\ m^{-1}\ K^{-1}$	15	[26]
	c_p , heat capacity	$J\ kg^{-1}\ K^{-1}$	500	[26]
	ρ , density	$kg\ m^{-3}$	7900	[26]

After modeling the entire treatment protocol with all of the aforementioned effects taken into account, the final electric field distribution at the end of the ninetieth pulse was used to correlate an electric field threshold with the experimental lesion volume. The volume of modeled tissue domain exposed to varying electric fields was integrated until the calculated volume was equal to the volume computed from the IRE lesion reconstruction.

In order to assess the thermal effects associated with the procedures, a 'thermal isoeffective dose' analysis was used [163]. Thermal isoeffective dose calculations are typically used for procedures involving complex variations in temperature as a function of time. Such calculations determine the amount of time it would take to equivalently damage the tissue as if it was held at a constant temperature. Although thermal damage can occur at lower temperatures for prolonged exposures, typically 43°C is chosen due to the abundant experimental data at this temperature [9, 43, 163]. It has been shown that neuronal damage occurs if temperature is elevated to 43°C for 60 minutes (t_{43} = 60 min) [124]. The following expression is the duration necessary to hold the tissue at 43°C to result in thermal isoeffective dose:

$$t_{43} = \int_{t=0}^{t=final} R^{(43-T_t)} dt \tag{21}$$

where T_t is the average temperature during dt. R is the number of minutes needed to compensate for a 1°C temperature change either above or below a breakpoint of 43°C. R is 0.25 when $T_t \leq 43°C$ and R is 0.5 when $T_t > 43°C$ [31, 124, 163]. The thermal dose was integrated from the onset of pulses to 5 min after the conclusion of treatment, allowing heat dissipation to return the tissue back to physiological temperature, thus incorporating all thermal effects from the procedure.

6.4 RESULTS

Post-operatively, no adverse clinical effects were observed in the animals. The canines did not demonstrate any adverse clinical effects after the procedure and were eating and able to resume normal activities within 10 hours of surgery. MRIs used to confirm the IRE lesion location and focality were performed within 60 minutes after completion of the pulse delivery, and a high resolution *ex vivo* scan is shown in Figure 26. These 7.0 T MRIs were chosen since

only the IRE lesion is visible and they include a superimposed schematic of the dual probes in order to guide the reader as to the placement of the electrodes.

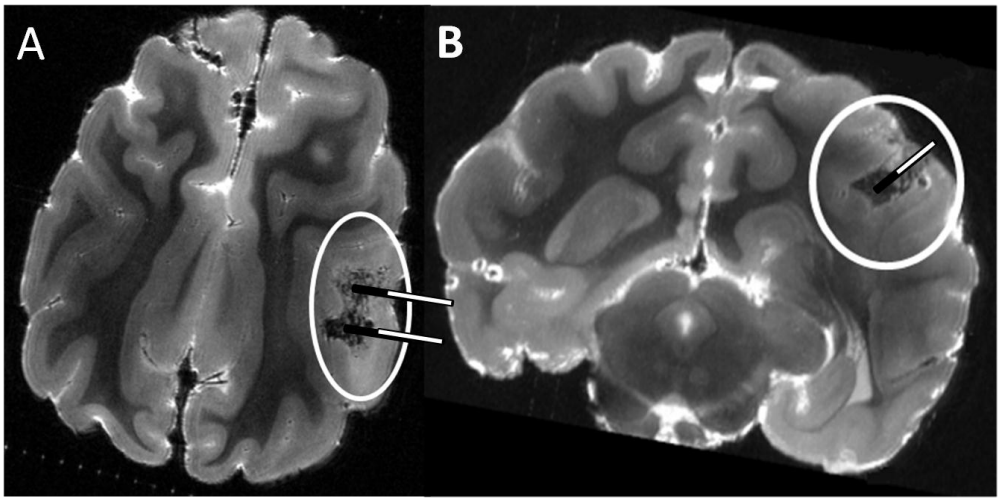

Figure 26: *Ex vivo* high-resolution 7.0 T MRI of IRE treated brain in dog 2 (1000 V). The exposed portions of the electrodes are depicted in black and their insulation in white to represent electrode placement. Reprinted with kind permission from Springer Science + Business Media as described in page 64.

From the *in vivo* MRI images, the appearances of acute intracranial lesions created with IRE procedures have classic MRI features of edema, inflammation, and disruption of the blood brain barrier [21, 22, 181]. These MRI features have been correlated and confirmed with the presence of these pathological processes in post-mortem pathological investigations, as previously reported in [51, 61]. Therefore, when measuring the treated area for the volume reconstructions, the hyper-intense T2W MRI scans were traced.

The three-dimensional reconstructed volumes corresponding to the IRE lesions from the treatments are shown in Figure 27, where the dual probes were inserted perpendicular to the reconstructed lesion. The reconstructions of 1000 V and 500 V in Figure 27 contain five and three white rings, respectively, corresponding to the number of traced slices. The varying voltages generated treatment areas that were approximately 10 mm (1000 V) and 5 mm (500 V) along the major axis across the electrodes.

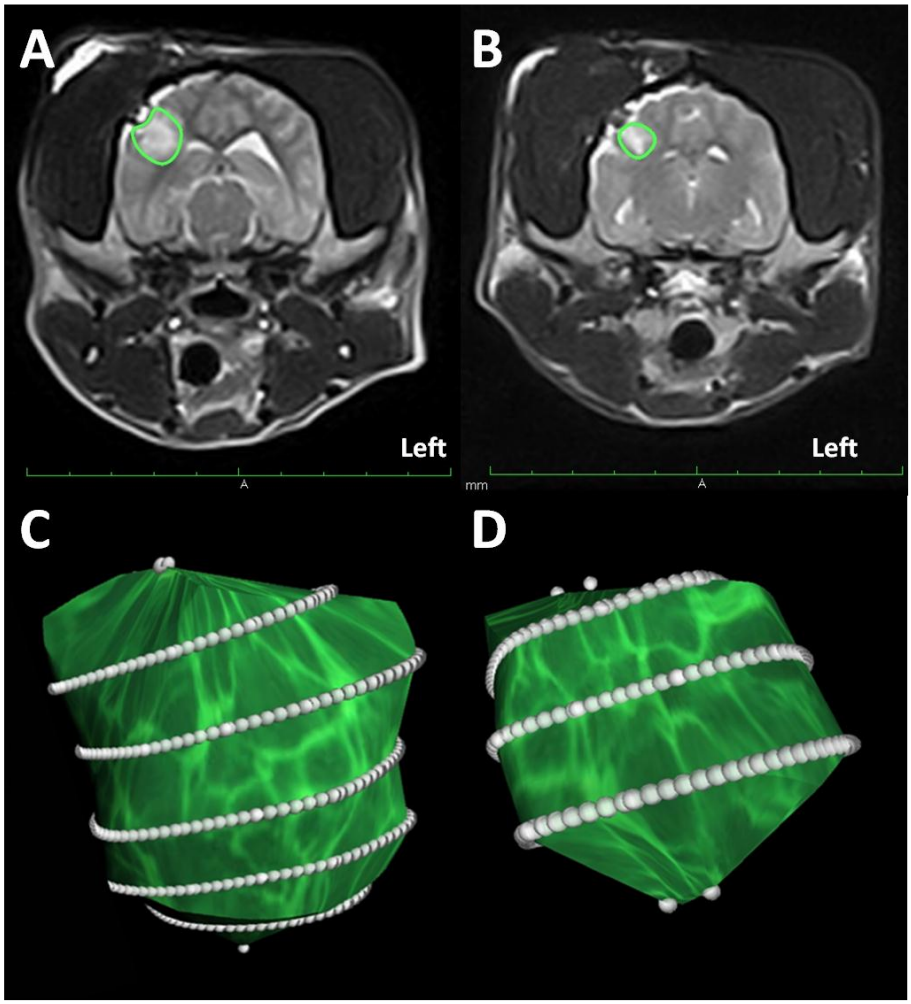

Figure 27: 0.2 T MRIs and 3D reconstructions of the lesions in the canine brains showing axial slices *in vivo* for dogs treated with A) 1000 V (1st dog) and B) 500 V (2nd dog). The sets of slices from these MRIs were used to create the 3D reconstructions of the lesions (green) for the dogs treated with C) 1000 V and D) 500 V. The white rings correspond to the boundary between the area of lesion and normal brain from the post-operative 0.2 T axial MRI (figure not to scale). Reprinted with kind permission from Springer Science + Business Media as described in page 64.

The computed baseline electrical conductivities, σ_o, were found to be 0.30 S/m and 0.12 S/m for the 1000 V and 500 V treatments, respectively (Table 8). These conductivity values are consistent with those typical in the literature [107, 168] and were used to generate the electric field distributions. Figure 28 shows the conductivity map for the 1000 V treatment after a ninety pulse IRE treatment and it shows three main regions. The center area is the tissue that has been exposed to electric field intensities greater than the threshold in our simulations (700

V/cm). There is also a transition region in which the conductivity varies between ~0.6 S/m and ~0.3 S/m for electric field exposures between 460 V/cm and 700 V/cm. Finally, the regions that are below 460 V/cm only represent changes in conductivity due to thermal effects.

Table 8: Computed σ using *in vivo* intracranial IRE data.

DOG	VOLTAGE [V]	CURRENT [A]	CHARGE [mC]	σ_0 [S/m]
1	1000	1.951 ± 0.2	9.89	0.30
2	500	0.361 ± 0.2	1.47	0.12

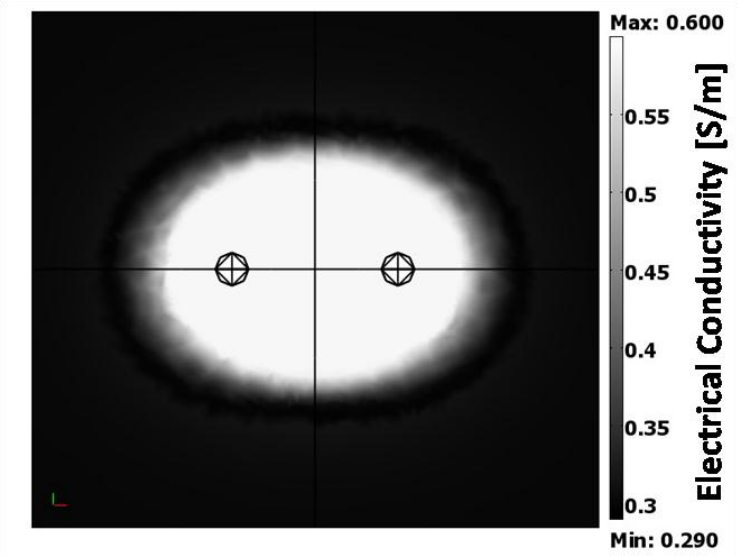

Figure 28: Planar map showing the conductivity (S/m) of the tissue on the plane along the midline of the electrodes as a function of electric field and temperature. Conductivity is seen to be the highest near the electrodes and decreases as it moves further away. Reprinted with kind permission from Springer Science + Business Media as described in page 64.

The electric fields found to correlate with the reconstructed lesion volumes in our experiments are shown in Table 9. For ninety 50 µs pulses delivered at 4 Hz it was found that 495 and 510 V/cm were the IRE thresholds for the 500 and 1000 V experimental dogs, respectively. The electric field distributions for these thresholds at completion of the modeled treatment pulse application are shown in Figure 29 in three Cartesian planes. The superimposed electric field isosurface plots represent the IRE treated areas with 500 V (dark gray) and 1000 V (light gray), respectively. One thing to note is that the dimensions of the IRE lesion is clearer in the xy and xz planes (Figure 29A and 29C) compared to the yz plane (Figure

29B). In addition, the modeled lesion from the 1000 V extends several millimeters beyond the margin of the lower voltage treatment.

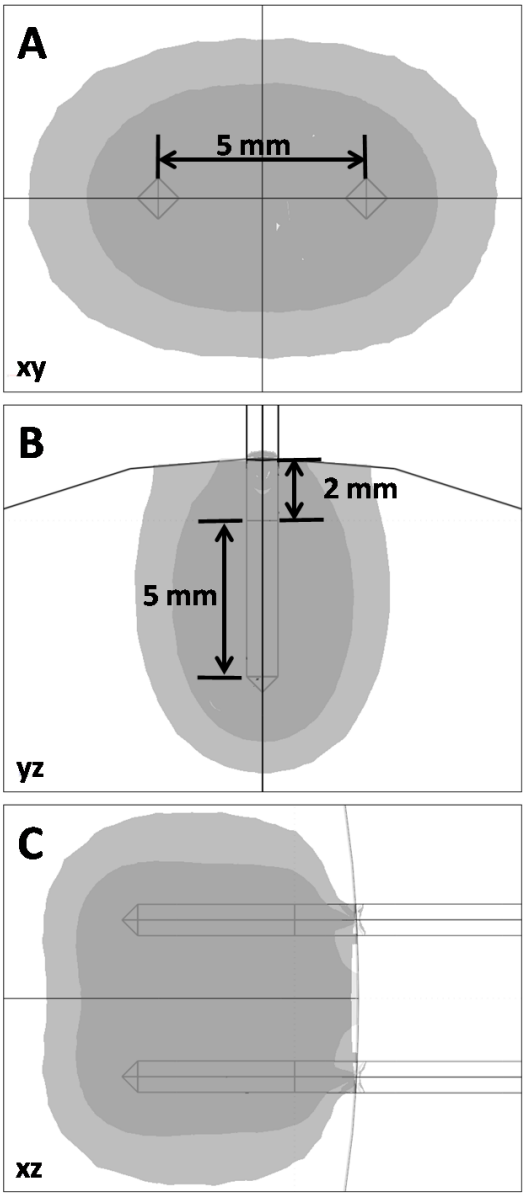

Figure 29: Numerically modeled electric field results showing the lesion threshold outputs for the 500 V (dark gray) and 1000 V (light gray) applied voltages. These volumes match the reconstructed lesions in Figure 27. Reprinted with kind permission from Springer Science + Business Media as described in page 64.

Table 9: Computed lesion volume with corresponding e-field correlation.

DOG	VOLTAGE [V]	VOLUME [cm^3]	ELECTRIC FIELD CORRELATION [V/cm]
1 – 0.2 T MRI	1000	0.599	510
2 – 0.2 T MRI	500	0.258	495
2 – 7.0 T MRI	500	0.250	501

Figure 30 shows the temperature and thermal dose distributions generated during the IRE treatment of dog 1, which received the highest voltage used in the study. The maximum t_{43} values were calculated around the electrode-tissue interface, where the highest electric field intensity is generated, and thus the greatest thermal effects due to Joule heating from pulse administration. A maximum thermal isoeffective dose, t_{43}, of 40 min was calculated for dog 1. This thermal dose is insufficient to generate significant neuronal thermal damage [124]. These results support that thermal effects did not play a significant role in the ablation of the canine brain tissue.

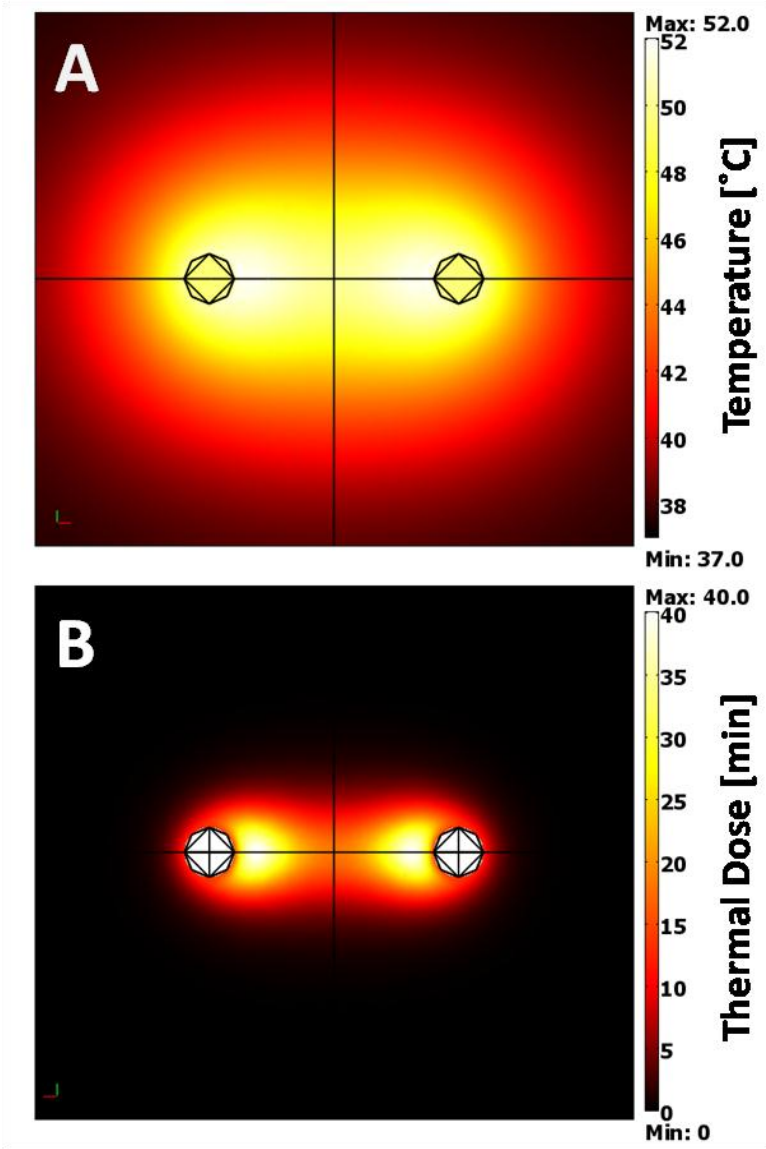

Figure 30: A) Planar map of the temperature distribution at the end of the final (90th) electric pulse. B) Cumulative t_{43} thermal dose equivalent 5 minutes after completion of the final electric pulse. Reprinted with kind permission from Springer Science + Business Media as described in page 64.

6.6 DISCUSSION

This chapter described the electric conductivities, lesion volumes, and electric field thresholds from the first systematic *in vivo* study of IRE for intracranial surgery [51]. Focal lesions were created in the right parietotemporal lobe of canines using small blunt tip probes to minimize damage during insertion. The advantages of IRE include its ability to achieve ablation non-thermally, compared to the mechanisms involved in cryoablation or radiofrequency

lesioning. This presents advantages over thermal focal ablation techniques because of its ability to spare major vasculature and the theoretical enhanced facilitation of drug delivery in reversibly electroporated regions of tissue [126]. Treatment application can be readily adapted for use with existing surgical and stereotactic guidance systems and technologies and can be performed rapidly and minimally invasively. Furthermore, IRE has demonstrated vascular sparing effects and can be monitored in real time using ultrasound, CT, or MRI. Current limitations of the technology appear to be primarily related to protocols with complex electrode design and placement logistics for ablating complex geometries, as well as treatment planning obstacles.

This chapter presents some of the important properties and behavior of brain tissue undergoing IRE therapeutic electric pulses, with strong implications for treatment planning. Focal lesions were created in the right parietotemporal lobe of canines using small blunt tip probes to minimize damage during insertion. The lesion volume reconstructions show affected regions of 0.258 and 0.599 cm^3 for the protocol used with applied voltages of 500 and 1000 V, respectively. When these volumes were calibrated to numerical models that incorporate conductivity changes due to electroporation and temperature changes, it was found that an effective IRE electric field threshold of ~500 V/cm may be used to predict IRE ablation volumes in brain tissue using ninety 50 µs pulses delivered at a frequency of 4 Hz. It is important to note that when applying this threshold to lesion prediction during treatment planning, the numerical simulation should also incorporate the conductivity changes addressed in this model for the protocol being used to ensure accurate pairing with the calibrated IRE threshold.

In order to accurately predict the electric field distribution of an IRE procedure, the bulk conductivity and its changes due to electroporation and temperature play a major role. For the two protocols investigated, the current during a typical pulse was 0.361 ± 0.2 A and 1.95 ± 0.2 A for applied voltages of 500 and 1000 V, respectively, corresponding to baseline modeled bulk conductivities of 0.12 and 0.30 S/m. The difference between these baseline conductivities results from the non-linear electric field dependency on conductivity that occurs due to tissue structural changes during electroporation [35, 106].

Our studies have confirmed that in the brain, the ablated volume is usually underestimated by MRI scans because of the coincidence of transient, IRE induced perilesional vasogenic brain edema resulting from disruption of the blood brain barrier. We have examined this with serial MRI examinations in canines and confirmed with pathological studies. For reconstruction, the accuracy of the volumes was limited to the interval between the MRI scans (2.5 mm). Therefore, the high-resolution (7.0 T) scans of the *ex vivo* brain from dog 2, which used 300 μm slices, may provide a better representation of the lesion and was thus used for matching the IRE threshold. The high-resolution *ex vivo* 7.0 T MRI from the 2nd dog resulted in a measured volume of 0.25 cm^3. This corresponds to an electric field intensity of 501 V/cm, which is similar to that found from the 0.2 T MRI reconstructions. However, this lesion may also be limited in accuracy due to shrinkage from formaldehyde tissue fixation.

To the best of our knowledge, our IRE investigations in the brain are the first to use IRE pulses that are 50 μs in duration. This is considerably shorter than those described in previous studies (100 μs - 20 ms) [1, 49, 110, 143]. It should be noted that the degree of electroporation is dependent on a variety of conditions such as tissue type, cell size, and pulse parameters including pulse shape, duration, number, and repetition rate [120, 129]. The shorter pulse durations allow for a reduced charge delivered to the tissue and minimize the heating generated by the procedure. This reduction in heating allows for larger voltages to be used, and thus larger lesions, while retaining the positive characteristics associated with IRE therapy. Alternatively, smaller and more targeted lesions can be achieved by decreasing the voltages between the IRE treatments. Doing so in combination with customized electrode geometries and pulse parameters should allow for precise ablation of volumes with varying sizes and shapes.

The temperature generated by the electric pulses was calculated and it was confirmed that the energy generated by the procedures were insufficient to induce thermal damage, even at the regions experiencing the greatest thermal effects, reinforcing the notion that IRE is an independent tissue ablation modality. Since thermal damage is a function of temperature and length of exposure, the negligible thermal damage associated with this procedure can be

explained by the fact that an electroporation pulse is typically a fraction of a second in duration [1, 50]. Furthermore, pulses were delivered at a frequency of 4 Hz, significantly faster than current typical procedures using ECG synchronization rates to avoid cardiac arrhythmias [8, 182]. Slowing the repetition rate in this manner will allow more time for heat dissipation by the vasculature, further reducing thermal effects. It should be noted that the thermal dose analysis is generally used for long term exposures of tissues to elevated temperatures. Therefore, the analysis used may not be ideal for electroporation investigations due to the burst of energy during the pulses. Nevertheless, it provides insight into the assessment of thermal damage in the regions of highest electric field.

An important limitation to the accuracy of this study is the relatively sparse amount of literature related to the conductivity of brain tissue and the inherent changes resulting from electroporation. Although the change in conductivity due to electroporation values have been taken from previous investigations [168], these data was based on hypothetical values that corresponded to known thresholds for rabbit liver tissue [167]. Therefore, they do not fully account for the thermally dependent conductivity changes that occur due to cumulative Joule heating associated with a complete IRE treatment. Despite this, it was found that varying the degree of thermal changes in conductivity did not significantly alter the correlated IRE electric field threshold. However, in order to develop a greater understanding of these phenomena, future studies on the brain should experimentally measure the changes in temperature and conductivity of the tissue due to IRE.

In order to obtain an even greater degree of accuracy when correlating lesion volumes with numerically modeled electric fields, future modeling studies should incorporate tissue heterogeneities in order to understand their influence on the resulting electric field and temperature distributions. It has been previously shown that the heterogeneous relations between different tissue types, such as gray vs. white matter brain tissue, plays a significant role in the electric field distribution, and thus IRE ablation zone [132]. Knowledge of the heterogeneous properties of these tissues may improve the outcome of an IRE procedure by allowing for planning of electric field distributions that will enhance tissue selectivity. In addition, these studies would allow even more precise correlation between numerically

modeled volumes and those seen on post-procedure MRI. This will be necessary in order to develop image-based treatment planning algorithms and the software necessary for their implementation.

This study also presented a method of computing the baseline electric conductivity based on measured current during a typical pulse and numerical methods. To keep experimental invasiveness low, the conductivity was backed out from the current measured by the pulse generator. More precise current readings would help to provide a more accurate initial conductivity. However, because the IRE electric field distribution is determined by the conductivity map rather than the absolute conductivity (which will change with the baseline), this should not greatly affect the thresholds determined here. Previous electroporation investigations in other tissues have reported significant increases in conductivity within pulses as compared to when it is removed. The conductivity increase is higher during the pulse presumably due to the contributions of short and long-lived pores [85]. However, in our typical pulses we did not observe this phenomenon likely due to the limitations of the equipment. In order to allow for more accurate treatment planning and outcome prediction, the dependency of the electrical conductivity on individual dogs and treatment location, should be monitored before, during, and after an IRE procedure using similar methods to the ones proposed by Cukjati *et al.* in [30]. By comparing the behavior of conductivity during pulse application with those predicted by numerical models, one may monitor treatment progress and prevent damage beyond the volume of intended ablation. Furthermore, conductivity measurements could be taken immediately prior to pulse administration using a low strength pulse, insufficient to induce electroporation, which would be applied for finalizing treatment planning.

6.7 CONCLUSION

This chapter examined the effects of IRE on brain tissue *in vivo* and used them to derive some of the properties and behaviors of brain tissue essential for effective treatment planning. Techniques were developed to use voltage and current data during a typical pulse to determine appropriate bulk baseline conductivities to be used in numerical simulations. Post-operative MRI scans were used to create three-dimensional lesion reconstructions for two treatment protocols. Numerical models incorporating conductivity changes as a function of

electroporation and temperature were used to coordinate the lesion reconstructions with an electric field threshold. The findings presented in this study may be used to aid in planning for the application IRE therapies in the treatment of brain cancer and other neuropathological disorders.

CHAPTER 7 - CT GUIDED IRREVERSIBLE ELECTROPORATION THROUGH BURR HOLES

7.1 INTRODUCTION

Irreversible electroporation (IRE) is a new minimally invasive technique to kill undesirable tissue in a non-thermal manner. We build on our previous intracranial studies in order to evaluate the possibility of using IRE for deep intracranial disorders. In this chapter we describe a minimally invasive computed tomography (CT) guided IRE procedure primarily in white matter. In addition, we report on the predicted treatment volume vs. thermal damage for three frequencies that are currently being used in clinical IRE protocols. For the first time, we confirm the non-thermal aspect of the technique with real-time temperature data measured *in vivo* at the electrode-tissue interface. In addition, we provide the reader with numerical results of typical protocols (i.e. eighty 50-µs pulses at voltage-to-distance-ratio of 2000 V/cm delivered at 1 Hz) in order to assess the effects of temperature, electroporation, pulse duration and repetition rate on the IRE treatment volumes.

7.2 BACKGROUND

Irreversible electroporation is a new technique for the focal ablation of undesirable tissue by using low energy electric pulses [1, 49]. An IRE treatment involves placing electrodes within the region of interest and delivering a series of electric pulses that are microsecond in duration [110]. The pulses create an electric field that induces an increase in the resting TMP of the cells in the tissue as described in Chapter 2 [36]. When the magnitude of the induced TMP is above a critical value, the cell membrane is disrupted to such an extent that the cell dies due to loss of homeostasis [154]. Consequently, the treated regions are sharply delineated and can be predicted with numerical models that simulate the electric field distributions in tissue [50]. One of the main advantages of IRE over other focal ablation techniques is that the pulses do not generate thermal damage due to resistive heating, thus major blood vessels, extracellular matrix and other tissue structures are spared [1, 49].

Our group has confirmed the safety of intracranial IRE procedures in three experimental dogs [51]. These procedures were performed through craniectomy defects to expose the cortex (gray matter) and allow for the insertion of the electrodes in the brain. We have also correlated

numerical models with 3D lesion reconstructions in order to establish electric field intensities needed to kill gray matter [64]. Our previous results have shown that IRE has potential to treat intracranial disorders. In this study, we report on the minimally invasive treatment that was performed through burr holes with computed tomographic (CT) guidance to aid in electrode positioning. In this manner, we move closer to the treatment of deep seated intracranial disorders where our treatment may offer a unique advantage due to the focal nature of the IRE lesions. In addition, it may give neurosurgeons alternate/complementary options to manage some disorders that are untreatable (not successfully) with current techniques due to their complex anatomical locations or proximity to critical structures. We also confirmed the non-thermal aspect of our technique with *in vivo* temperature measurements during the pulse delivery using fiber optic probes. Finally, we performed a parametric study of the effects that the change in conductivity due to electropermeabilization and the thermal effects have on the electric field distribution and thus outcome. In this manner we can analyze treatment protocols and select those that treat the volume of interest without generating any thermal damage. We provide a realistic view of how changing parameters is important when determining IRE protocols and how important it is to understand the implications of changing one parameter over another one.

7.3 METHODS

This study was approved by the Institutional Animal Care and Use Committee and performed in a Good Laboratory Practices (GLP) compliant facility. After induction of general anesthesia, two 1.2 mm burr holes were created in the skull in preparation for electrode insertion. The CT guidance system was used to place the electrodes into the target location (corpus callosum). A neuromuscuslar blocker was administered to suppress patient motion prior to the IRE treatment. A focal ablative IRE lesion was created in the white matter of the experimental canine subject using the NanoKnife® generator (Angiodynamics, Queensbury, NY USA), and 1-mm diameter blunt tip electrodes exposed and separated by 5 mm each. After insertion of the electrodes, four sets of twenty 50µs pulses were delivered with a voltage-to-distance ratio of 1000 V/cm between the electrodes. The polarity of the electrodes was alternated between the sets to minimize charge build-up on the electrode surface. These

parameters were determined from our previous *in vivo* IRE procedures which showed that they were sufficient to ablate tissue. The NanoKnife® was synchronized with the dog's heart rate in order to prevent any ventricular fibrillation or other arrhythmias.

Open source image analysis software (OsiriX, Geneva, Switzerland) was used to calculate the IRE focal ablation volumes. The lesions were traced in each of the 2D post-operative magnetic resonance imaging (MRI) scans and a 3D solid that represents the IRE lesion volume was generated as in [64]. We calculated lesion volumes based on the axial scans of the *in vivo* T2-weighted, T1-weigthed post-contrast 0.2 T MRI and *ex vivo* 7.0 T MRI in order to investigate the variability between imaging modalities.

Temperatures were measured in the brain during the procedure using the Luxtron® m3300 Biomedical Lab Kit Fluoroptic® Thermometer (LumaSense™ Technologies, Santa Clara, CA USA). STB medical fiber optic probes (LumaSense™ Technologies, Santa Clara, CA USA) were placed at the tip of the electrode-tissue interface and 7.5 mm along the insulation (Figure 31).

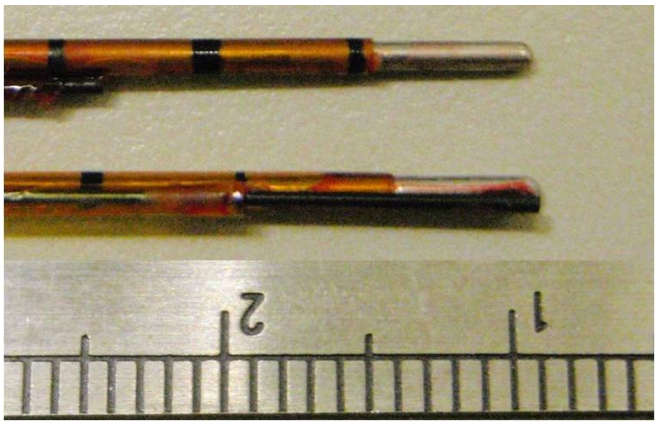

Figure 31: IRE electrodes used in the intracranial treatment of white matter with attached fiber optic probes to measure temperature during pulse delivery.

7.4 MODEL

Numerical models can be used for treatment planning to ensure that only the targeted regions are ablated [50]. In order for this to be accurate one has to know both the physical properties of the tissue and the electric field threshold needed for IRE. To the best of our knowledge this is the first attempt at treating the white matter with IRE. Therefore, our goal is

to use the numerical models to establish the electric field threshold needed to kill white matter and be able to predict future treatments in the same region. The threshold was determined by correlating the IRE lesion volume with electric field distributions of identical dimensions.

In order to simultaneously compute if any thermal damage resulted from the procedure a third time-dependent analysis PDE was added under the PDE Mode in Comsol Multiphysics v.3.5a (Stockholm, Sweden). In this manner we capitalize on the calculated temperatures through the Penne's bioheat equation and compute the thermal damage in the entire tissue domain in order to perform a comprehensive analysis of the thermal effects. The expression to calculate the damage is

$$\frac{\partial \Omega}{\partial t} + \nabla \cdot \Gamma = F \tag{22}$$

where Ω is the damage integral, the Γ is the flux vector and $F$is the forcing function

$$F = \max(0, exp(ln(\zeta) - E_a/(R \cdot T(t))) \tag{23}$$

that was described in Chapter 4. The forcing function is written in logarithmic form in order to prevent abrupt changes since small changes in temperature can have significant impact on the damage. The flux vector was assumed to be zero since the heat conduction is already incorporated in the Bioheat Equation and there is no such thing as thermal damage conduction. Similarly, all the boundaries in the domain were assumed to be of the Neumann form where $\frac{\partial \Omega}{\partial n} = 0$. The analysis was performed with a starting temperature equal to physiological conditions (37 °C = 310.15 K) and the cell death parameters from Chapter 4.

The default Comsol Multiphysics 3.5a "fine mesh" was use in the study and it was found that remeshing did not increase the accuracy of the solution by more than 1 %. Initially, the 3D simulation was solved for 1/1600 of the total treatment duration under homogenous tissue conditions in order to establish a baseline electric field distribution. The homogeneous electric field map is crucial for the simulation to run since it provides the necessary information for the dynamic conductivity function that was also used in Chapter 6. The "FGMRES" linear transient solver system was used with the "Algebraic Multigrid" preconditioner with "Free" time stepping were the solver parameters capable of solving the simulation. In order to ensure that the solutions were smooth we used a relative (0.1 s) and absolute (0.01 s) tolerances that would

ensure smooth solutions over the total simulation time of 20 s, 80 s, and/or 160 s that represented the eighty pulses delivered at 4 Hz, 1 Hz, and 0.5 Hz, respectively. A time step of 0.1 s was used in all of the simulations and it was input in Comsol in the following manner: "range(0,0.1,160)" for the 0.5 Hz IRE treatment for example. The non-permeabilized white matter electrical conductivity, $\sigma = 0.2558\, S/m$, used in the simulations was measured by Latikka *et al.* in [107] in living humans at 37 °C.

7.5 RESULTS

Figure 32 shows the focal, well circumscribed nature of the IRE lesion as seen in the 0.2 T MRI. The lesion as seen on the T2-weighted MRI is represented by the hyperintense areas that are consistent with blood-brain-barrier disruption in the white matter. The T1-weighted post contrast MRI shows the lesion as hypointense regions where the contrast is able to leak into the brain due to the lesion. Finally, the *ex vivo* 7.0 T MRI shows the cavity that is left after an IRE treatment in the brain. The lesion volume is smaller than those calculated from the *in vivo* MRI since transient edema effects have been resolved and due to shrinkage of the brain during the fixation process.

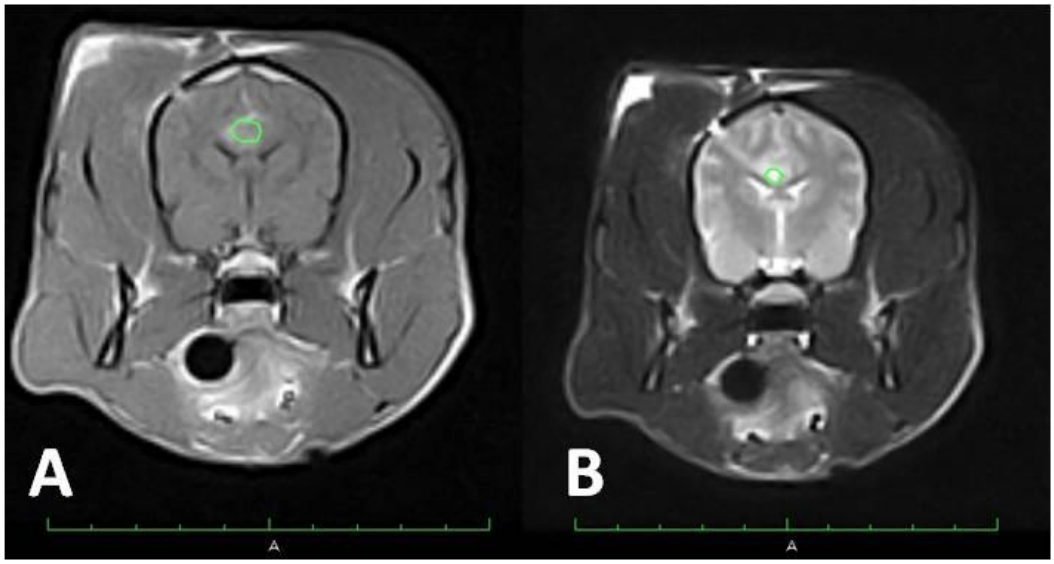

Figure 32: (A) T1W+C and (B) T2W MRI scans post IRE confirms the location and circumscribed nature of the lesion.

There are several lesion reconstructions resulting from the white matter IRE treatment. Figure 33 shows the 3D lesion reconstructions from the high-resolution MRI scans. The

calculated lesion volumes were 0.131 cm^3, 0.120 cm^3, and 0.058 cm^3 for the T1W+C, T2W and 7.0 T MRIs, respectively. The lesion reconstruction from the 0.2 T MRI contains 3 slices while the high-resolution contains 20. The most affected region appears to be directly in between the electrodes. Since the distance between the electrodes is the shortest path for the current to travel from the energized electrode to the ground, this region experiences the highest electric fields. The two different electric field isocontours correlate with the lesion volumes calculated from the 0.2 T and 7.0 T MRI. The larger contour corresponds to the T1W+C lesion volume (0.1313 cm^3) with a lower electric field threshold of 630 V/cm. The smaller contour corresponds to the 7.0 T lesion volume (0.0584 cm^3) with a higher electric field of 875 V/cm.

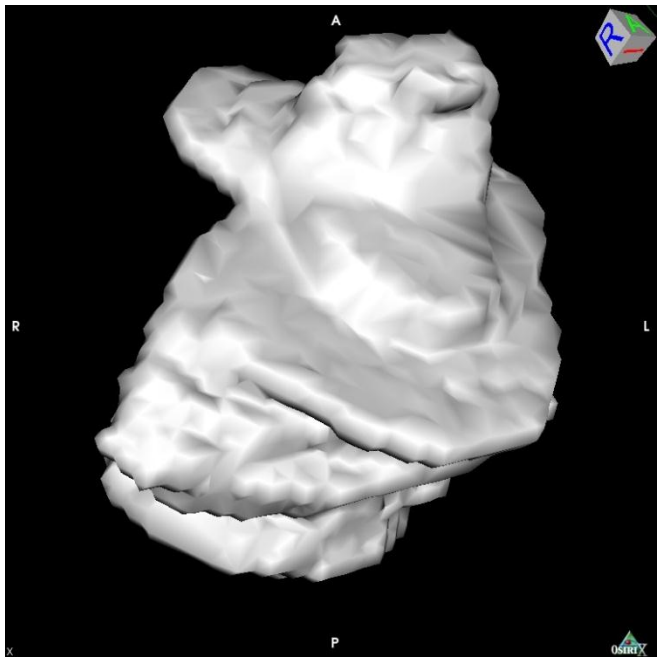

Figure 33: IRE lesions reconstructed using Osirix software from the high-resolution 7.0 T MRI.

Figure 34 shows the temperature distribution measured by the probe located at the electrode-tissue interface tip and 7.5 mm above the insulation (Figure 31). For the probe at the interface, four sets of mild increase in temperatures are seen that correspond to each of the pulse sets delivered. The probe in the insulation also shows some very mild increase in temperature that is probably due to heat conduction from the treatment region. The changes in the temperature resulting from IRE are less than 0.5 °C and they are not sufficient to generate thermal damage. This confirms that any cell death achieved by the procedure was a

direct result of IRE since at the electrode-tissue interface we expect to achieve the highest thermal effects. In addition, this result supports our assumption in the numerical models that electrical conductivity changes due to electroporation only and not temperature. It is important to note that the starting temperature was approximately 33 °C due to the anesthesia effects and this is neuro-protective during brain procedures in general and that the pulse delivery took approximately 200 seconds.

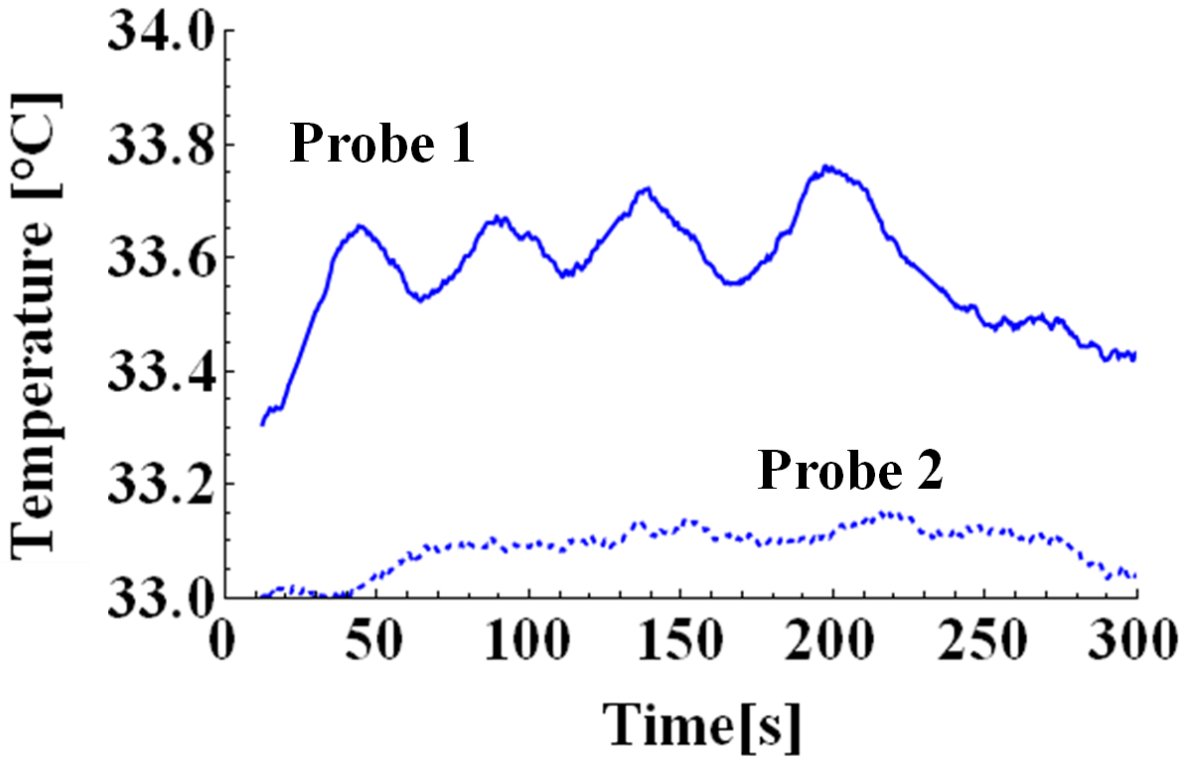

Figure 34: Temperature [°C] distribution during an IRE treatment in the white matter of a canine subject.

The curves on Figure 35 are volumetric quantities of tissue exposed to temperatures greater than 43°C or 50°C during the delivery of an eighty pulse IRE treatment in our numerical simulations. The three applied voltages of 500 V, 1000 V, and 1500 V resulted in voltage-to-distance ratios of 1000 V/cm, 2000 V/cm, and 3000 V/cm respectively. In Figure 35A the pulses were delivered at 0.5 Hz (160 s for total treatment) and it shows that the only volumes of tissue exposed to temperatures greater then 43°C were achieved when delivering 1500 V up to a maximum volume of about 0.1 cm^3 at the completion of the treatment. The effects of temperature are more relevant when the pulses are given at a higher repetition rate as in Figure 35B in which the frequency was increased to 1.0 Hz (80 s for total treatment).

In this case, by applying 1000 V only marginal volume (~0.025 cm^3) of tissue was exposed to elevated temperatures compared to the 1500 V treatment which had a volume of tissue of 0.325 cm^3 and 0.05 cm^3 exposed to temperatures greater than 43°C and 50°C, respectively. In Figure 35C one can appreciate the drastic effects of increasing the repetition rate even more in which the pulses are delivered at 4.0 Hz (20 s for total treatment). In this scenario, even the applied 1000 V is achieving tissue heating above 50°C in about 0.05 cm^3 of tissue and about 0.2 cm^3 experiences temperatures greater than 43°C. Finally, if the applied voltage is 1500 V, the majority of the tissue will be heated to extreme temperatures since 0.58 cm^3 and 0.25 cm^3 of tissue experiences temperatures greater than 43°C and 50°C, respectively.

Even though the volumes of tissue exposed to a minimum temperature can give insight as to the thermal effects resulting from a particular IRE protocol, it does not provide any quantitative measure of thermal damage. Consequently, in Figure 36 we not only report the volume of tissue exposed to a minimum electric field of 580 V/cm (assumed to be IRE threshold) but also the volume of tissue that experiences thermal damage using the Arrhenius analysis as in Chapter 4. Similar to the previous analysis, in Figure 36 we investigate the influence of increasing the frequency of pulse delivery in both predicted IRE treatment and thermal damage. Specifically, in Figure 36A the only curves that are displayed correspond to the IRE volumes treated with 500 V (0.18 cm^3), 1000 V (0.41 cm^3) and 1500 V (0.65 cm^3). This occurs since the pulses are delivered every 2 seconds (0.5 Hz) so there is sufficient time for the heat to dissipate through conduction and blood perfusion by the onset of the following pulse. In Figure 36B there are virtually identical IRE treatment volumes but by using an applying 1500 V there is some thermal damage generated within 40 seconds and affects about 0.08 cm^3 of tissue which is approximately 14 % of the IRE volume. Finally, Figure 36C displays the IRE and thermal damage volumes for the 4.0 Hz treatment. In this case, there is very mild damage when applying 1000 V but significant damage when increasing the voltage to 1500 V since approximately 1/3 of the IRE volume is thermally damaged (0.25 cm^3). Additionally, if one focuses on the first few seconds of the applied 1500 V, there is an increase in the IRE lesion volume due to the increase in the temperature and thus the electric conductivity.

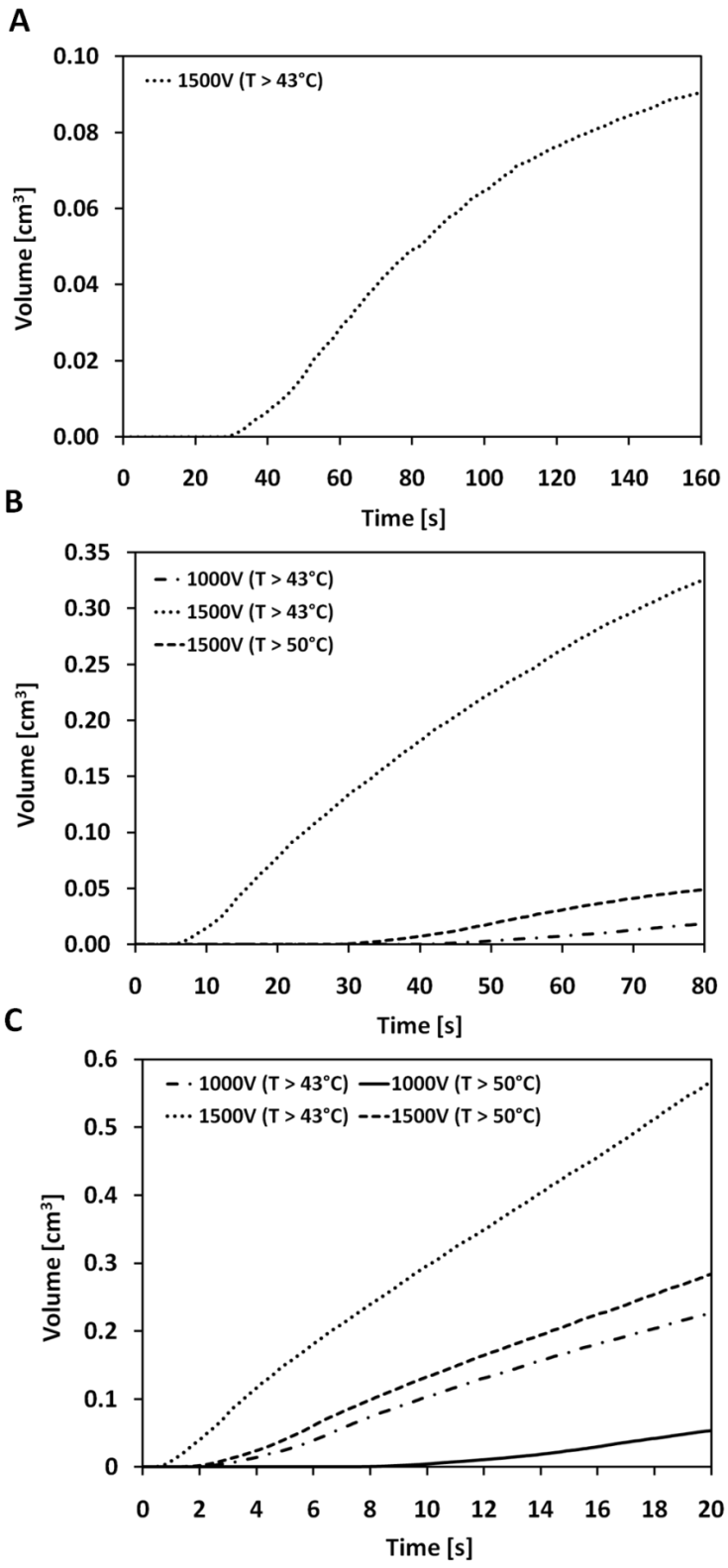

Figure 35: Time history of the volumes of tissue exposed to greater temperatures than 43°C and 50°C during an eighty pulse (50 µs) IRE treatment with pulse frequencies of A) 0.5 Hz (160 s), B) 1.0 Hz (80 s), and C) 4.0 Hz (20 s). The applied voltages were 500 V (1000 V/cm), 1000 V (2000 V/cm), and 1500 V (3000 V/cm) for each case.

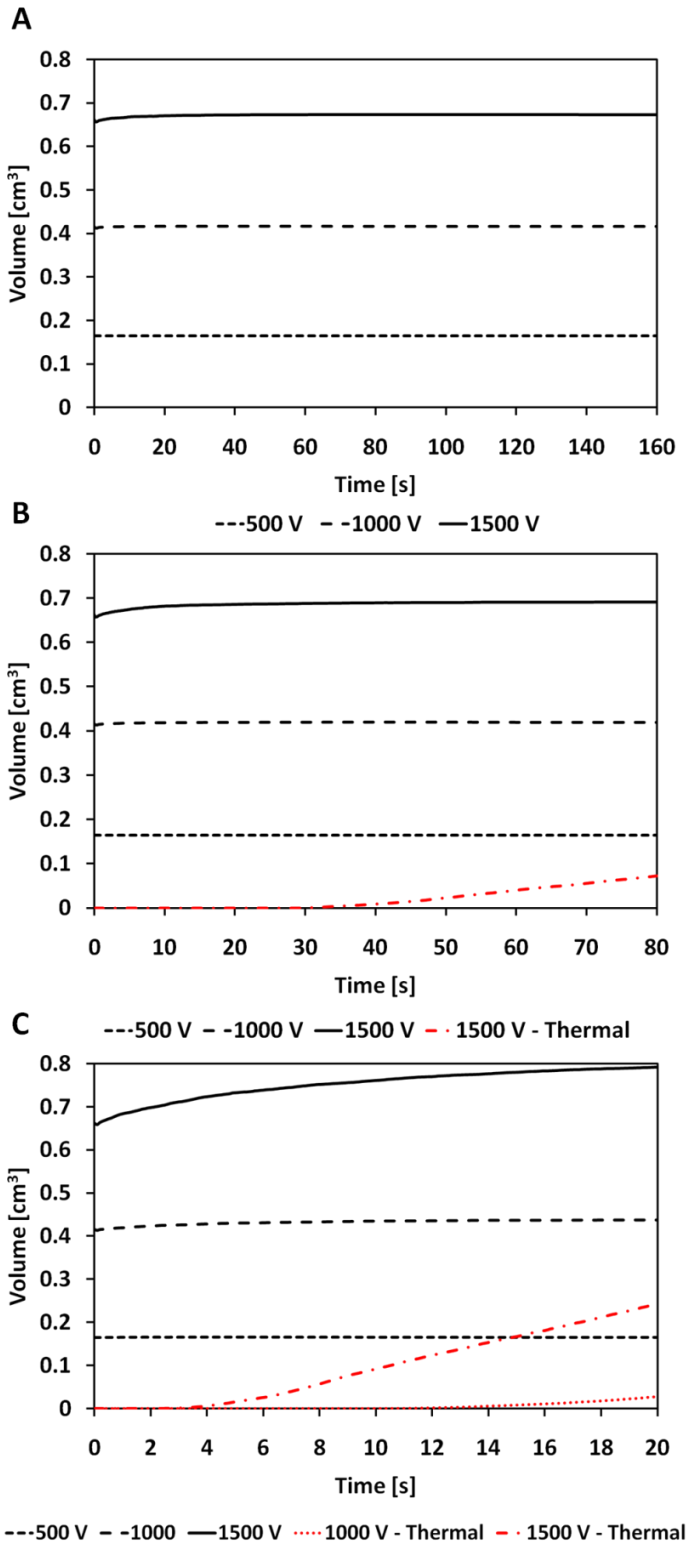

Figure 36: Time history of the tissue volumes experiencing IRE and thermal damage during an eighty pulse (50 µs) IRE treatment with pulse frequencies of A) 0.5 Hz (160 s), B) 1.0 Hz (80 s), and C) 4.0 Hz (20 s). The applied voltages were 500 V (1000 V/cm), 1000 V (2000 V/cm), and 1500 V (3000 V/cm) for each case.

7.6 DISCUSSION

We correlate IRE lesion volumes from post-procedure 0.2 T MRI and from *ex vivo* 7.0 T MRI. It is important to note that the 0.2 T MRI had 3.0 mm slices so the volume may be overstimated. The 7.0 T which scans every 300 μm was performed *ex vivo* which probably underestimates the true volume due to tissue fixation. Finally, there was no time for the lesion to evolve since the aim of the study was to perform the procedure deep in the brain and evaluate the lesion created. Therefore, the electric field thresholds we determined is only as accurate as the reconstructed volumes. Future work will also correlate the IRE lesions with histological and gross pathology.

From the results one can see that the lesion is very small. The ability of IRE to focally ablate small volumes of brain tissue in a minimally invasive fashion has tremendous potential clinical implications for the treatment of brain diseases in which destruction of a known, focal neuroanatomic target is desired, such as some forms of epilepsy or central neuropathic pain syndromes. To the best of our knowledge, this is the first CT- guided intracranial IRE treatment. We believe that the rapidity, minimally invasive nature, and precision offered by image guided IRE procedures, such as this one, will be the preferred treatment delivery platform for future applications of our technology in the brain.

This parametric study provides a reliable method to develop treatment protocols in order to ensure that the IRE protocol acts independently of thermal damage. The pulse frequency was the basis of the study and it confirms that if one delivers pulses too rapidly, thermal damage will be inevitable and many of the benefits from this technology are not realized in treatment. The described method takes into account all the pulse parameters including the duration, frequency, and magnitude in addition to the dynamic changes in tissue electrical conductivity due to electroporation and joule heating and biological processes as the metabolic heat generation and blood perfusion. It is imperative that the models are explored for each particular application in order to optimize treatment protocol and better predict the treatment outcome.

CHAPTER 8 - IRREVERSIBLE ELECTROPORATION TREATMENT OF BRAIN CANCER PATIENT[5]

8.1 INTRODUCTION

Irreversible electroporation (IRE) has shown promise as an ablative therapy for a variety of soft-tissue neoplasms. Here we describe the therapeutic planning aspects and first clinical application of IRE for the treatment of an inoperable, spontaneous malignant intracranial glioma in a canine patient. The IRE ablation was performed safely, effectively reduced the tumor volume and associated intracranial hypertension, and provided sufficient improvement in neurological function of the patient to safely undergo adjunctive fractionated radiotherapy (RT) according to current standards of care. Complete remission was achieved based on serial magnetic resonance imaging examinations of the brain, although progressive radiation encephalopathy resulted in the death of the dog 149 days after IRE therapy. The length of survival of this patient was comparable to dogs with intracranial tumors treated via standard excisional surgery and adjunctive fractionated external beam RT. Our results illustrate the potential benefits of IRE for *in vivo* ablation of undesirable brain tissue, especially when traditional methods of cytoreductive surgery are not possible or ideal, and highlight the potential radiosensitizing effects of IRE on the brain.

8.2 BACKGROUND

High-grade gliomas, most notably glioblastoma multiforme (GBM), are among the most aggressive of all malignancies in humans and dogs. High-grade variants of gliomas are difficult to treat and generally considered incurable with singular or multimodal therapies [105, 176]. Many patients with GBM die within one year of diagnosis, and the 5-year survival rate in people is approximately 10% [176]. Despite extensive research and advancement in diagnostic and therapeutic technologies, very few therapeutic developments have emerged that significantly improve survival for humans with GBM over the last seven decades [176].

Dogs with spontaneous brain tumors have been shown to be excellent translational models of human disease. Intracranial spontaneous primary tumors in dogs are three times

[5] Published with permission from: Non-thermal irreversible electroporation (N-TIRE) and adjuvant fractionated radiotherapeutic multimodal therapy for intracranial malignant glioma in a canine patient. Technol Cancer Res Treat, 10(1):1-11, 2011. Adenine Press; http://www.tcrt.org. Authors: Garcia, P.A., T. Pancotto, J.H. Rossmeisl, N. Henao-Guerrero, N.R. Gustafson, G.B. Daniel, J.L. Robertson, T.L. Ellis, and R.V. Davalos.

more common than in humans, and brachycephalic breeds of dogs have predispositions to the development of gliomas [152]. Canine malignant gliomas (MG) exhibit similar clinical, biologic, pathologic, molecular, and genetic properties as their human counterparts [44, 152, 175]. The husbandry practices of many dog owners in developed countries may allow dogs to be considered sentinels for environmental risk factors associated with tumorigenesis. Dogs are of a suitable size that allows accelerated development and application of novel diagnostic and therapeutic clinical procedures. The physiological and neurologic functions of dogs with brain tumors can be readily assessed by changes in their interactions and learned behaviors and by a battery of clinical neurological examination methods.

Prognostic factors for dogs with primary intracranial neoplasms include both tumor histology, anatomic tumor location, and type of treatment administered [74]. Prolonged survivals are rare in dogs with glial-origin neoplasms, irrespective of the type of treatment administered, and death is often attributed to recurrent local disease [74]. Median survivals of 0.2, 0.9, and 4.9 months have been reported for dogs with several types of brain tumors receiving either symptomatic therapy, cytoreductive surgery, or multimodal therapy (surgery and radiotherapy or hyperthermia), respectively, illustrating the poor long term prognosis for dogs with brain tumors and need for the development of more effective therapies [74].

Considering the therapeutic challenge that human and veterinary neurosurgeons are faced with when managing patients with MG, many recent efforts have been directed into the development of minimally invasive techniques that can be used for focal neoplastic tissue ablation as alternatives to traditional surgical approaches. Thermal-dependent tissue ablation techniques, such as cryoablation [180], laser interstitial thermotherapy [5], and radiofrequency lesioning [25] have been developed, but with limited success or applicability in the brain primarily due to the heat sink effect associated with the vascular brain parenchyma.

Electroporation, which results in an increase in the permeability of the cell membrane, is initiated by exposing cells or tissues to external electric fields [190, 193]. The electric fields induce a transmembrane potential (the electric potential difference across the plasma membrane) which is dependent on a variety of conditions such as tissue type, cell size, and pulse parameters including pulse strength and shape, duration, number, and repetition

rate. As a function of the induced transmembrane potential, the electroporation pulse can either: have no effect on the cell membrane, reversibly permeabilize the cell membrane after which cells can survive (reversible electroporation), or permeabilize the cell membrane in a manner that leads to cell death (irreversible electroporation).

When applied in tissue, it has been shown that certain electric field parameters can achieve irreversible electroporation without causing thermal damage to the treated volume [36], a process which is referred to as non-thermal irreversible electroporation (IRE). IRE is a novel tissue ablation technique that involves delivery of electrical pulses above critical, tissue-specific electric field thresholds, which results in permeabilization of cells presumably through formation of nanoscale aqueous pores in cytoplasmic membranes, and resultant death of cells within a treated volume [36]. The minimally invasive procedure involves placing 1-mm electrodes into the targeted area and delivering series of electrical pulses for several minutes. IRE affects essentially only one component of the tissue, the lipid bilayer, and spares other critical components of the tissue such as major blood vessels, nerves and the extracellular matrix [122, 154].

Recently, IRE has shown promise as a therapy for soft-tissue neoplasms, using minimally invasive instrumentation and allowing for treatment monitoring with routine clinical procedures [1, 110, 154]. We believe that the IRE technology possesses other inherent properties that make it well suited for the treatment of brain lesions in which the therapeutic intent is focal and highly controlled tissue destruction. The thermal sparing effect of IRE is advantageous compared to previously described methods of tissue destruction that are dependent on local tissue temperature changes. Studies of focal IRE ablations in mammalian liver and prostate have shown that therapeutic protocols are safe and can be implemented to preserve the integrity of sensitive tissues, such as the major vasculature and ductal frameworks within treated parenchymal volumes [110, 143, 155]. We have previosuly demonstrated the safety, vascular sparing, and other focal ablative characteristics of IRE in the normal canine brain [51, 61].

Here we describe the first application of IRE for the *in vivo* treatment of an inoperable spontaneous canine intracranial MG as part of a comprehensive multimodal therapeutic

strategy, highlighting its potential for more widespread clinical usage for the ablation of undesirable brain tissue. This case study demonstrates the ability of IRE to safely ablate pathologically heterogeneous brain tissue while preserving vascular integrity and patient neurological functions. We illustrate the minimally invasive nature of IRE and the ability to plan and execute IRE therapy using procedures routinely used in clinical evaluation of the neurosurgical patient. Finally, we present practical and theoretical considerations that require further investigation to better define and refine IRE treatment parameters within the intracranial environment.

8.3 METHODS

8.3.1 CASE HISTORY

The patient was a 12-year-old, castrated male, mixed breed dog with an 8 week history of visual deficits of the right eye and partial seizures, which progressed to behavioral changes and ataxia of all limbs the week prior to referral to the Virginia-Maryland Regional College of Veterinary Medicine Veterinary Teaching Hospital Neurology and Neurosurgery Service. Upon admission, the dog had normal vital parameters. Neurological evaluation revealed mild generalized proprioceptive ataxia, right hemiparesis, aggressive behavior, and propulsive circling to the left. Visual tracking and the menace response were absent in the right eye, with intact direct and consensual pupillary light reflexes. Postural reaction deficits were detected in both right thoracic and pelvic limbs. No other significant physical examination abnormalities were detected. The history and neurological abnormalities present were consistent with a lesion in the left prosencephalon.

Magnetic resonance images (MRI) of the brain were obtained under general anesthesia. An intra-axial mass lesion, originating in the subcortical white matter of the left parietal, temporal, and occipital lobes of the cerebrum was noted on MRI (Figure 37). The mass was poorly marginated, heterogeneously iso- to hyperintense on T1 (Figure 37A), T2, and fluid attenuated inversion recovery (FLAIR; Figure 37B) sequences, and demonstrated heterogeneous enhancement following intravenous administration of gadolinium (Figure 37C and 37D). Significant perilesional edema was present throughout the left cerebral hemisphere, and mass effect was manifested as obliteration of the left lateral ventricle, falx cerebri shift to

the right, transtentorial herniation of the left occipital lobe of the cerebrum resulting in mesencephalic compression (Figure 37), and foramen magnum herniation. The MRI characteristics were consistent with a glial-origin neoplasm associated with subacute intraparenchymal brain hemorrhage. For treatment of the peritumoral edema, intravenous 20% mannitol and corticosteroids were administered.

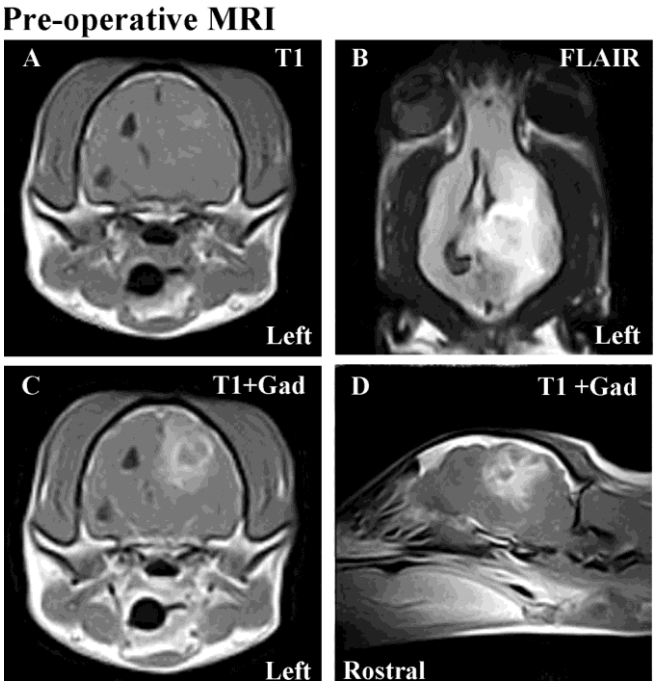

Figure 37: Pre-operative MRI scans (A- axial T1 pre-contrast; B- Dorsal FLAIR; C- axial T1 post-contrast; D- left parasagittal T1 post-contrast) revealing large, intra-axial mass lesion in the left cerebrum associated with secondary peritumoral edema, hemorrhage, and mass effect manifested as obliteration of the left lateral ventricle and shifting of the third ventricle to the right of midline. Published with permission from Adenine Press as described in page 93.

8.3.2 IRE TREATMENT PLANNING

Open source image analysis software (OsiriX, Geneva, Switzerland) was used to isolate the brain tumor geometry from the normal brain tissue. The tumor was traced in each of the two-dimensional (2-D) diagnostic T1 post-contrast MRI scans as seen in Figure 38. Attempts were made to exclude regions of peritumoral edema from the tumor volume by composite modeling of the tumor geometry using all available MRI sequences (T1 pre- and post- contrast, T2, and FLAIR) and image planes. A three-dimensional (3-D) solid representation of the tumor volume (Figure 39) was generated using previously reported reconstruction procedures [61]. The tumor

geometry was then imported into a numerical modeling (Comsol Multiphysics, v.3.5a, Stockholm, Sweden) software in order to simulate the physical effects of the electric pulses in the tumor and surrounding healthy brain tissue. The electric field distribution was determined using the method described in [64] in which the tissue conductivity incorporates the dynamic changes that occur during electroporation [167]. In our model we assumed a 50 % increase in conductivity when the tissue was exposed to an electric field magnitude greater than 500 V/cm, which we have shown as a IRE threshold for brain tissue using specific experimental conditions [64]. Currently, the threshold for brain tumor tissue is unknown so the same magnitude as normal tissue was used for treatment planning purposes.

Based on the tumor dimensions and numerical simulations, we determined pulse parameters that would only affect tumor tissue (Table 10). The resulting electric field distributions from these parameters are displayed in Figure 39. The two sets of pulse strengths were delivered in perpendicular directions to ensure uniform coverage of the tumor and were synchronized with the electrocardiogram (ECG) signal to prevent ventricular fibrillation or other cardiac arrhythmias (Ivy Cardiac Trigger Monitor 3000, Branford, CT, USA). The sets of pulses were delivered with alternating polarity between the sets to reduce charge build-up on the surface of the electrodes. In addition, shorter pulse durations than those used in previous IRE studies [1, 143, 155] were used in order to reduce the charge delivered to the tissue and decrease resistive heating during the procedure. Our calculations and temperature measurements from previous intracranial IRE procedures ensured that no thermal damage would be generated in normal brain. The temperature measured at the electrode tip resulted in a maximum 0.5 °C increase after four sets of twenty 50-µs pulses when using similar pulse parameters to the ones in Table 10 [63]. In addition, the charge delivered during the procedure was typical or lower than that used in humans during electroconvulsive therapy, a treatment for depression that also uses electric pulses [87].

Table 10: IRE treatment protocol for canine malignant glioma patient.

VOLTAGE (V)	ELECTRODE GAP (cm)	ELECTRODE EXPOSURE (cm)	VOLT-TO-DIST RATIO (V/cm)	PULSE DURATION	NUMBER OF PULSES	FREQUENCY
500	0.5	0.5	1000	50 µs	2 x 20	ECG synchronized
625	0.5	0.5	1250	50 µs	4 x 20	ECG Synchronized

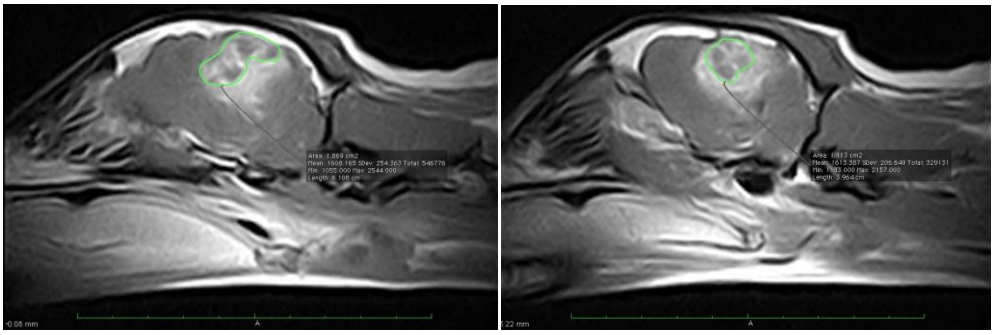

Figure 38: Consecutive T1 post-contrast MRI images in the left parasagittal plane of a canine glioma patient. The tumor is delineated in green and there is marked peritumoral edema and hemorrhage. Rostral is to the left in both images. Published with permission from Adenine Press as described in page 93.

8.3.3 IRE Therapy

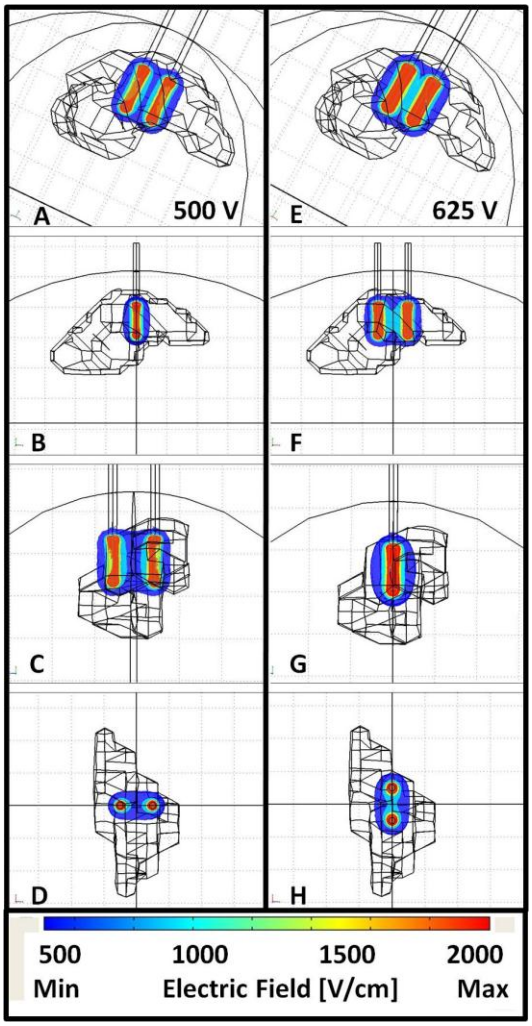

Figure 39: Brain, electrodes and reconstructed tumor geometry imported into numerical software for IRE treatment planning. 3-D electric field distributions corresponding to the (A-D) 500 V and (E-H) 625 V treatment protocols (Table 10). Published with permission from Adenine Press as described in page 93.

Total intravenous general anesthesia was induced and maintained with propofol and fentanyl constant rate infusions. A routine left rostrotentorial approach to the canine skull was performed and a limited left parietal craniectomy defect was created. The craniectomy size was limited to the minimum area necessary to accommodate placement of the IRE electrode configurations required to treat the tumor, as determined from pre-operative treatment plans. Following regional durectomy, multiple biopsies of the mass lesion were obtained, which were consistent with a high-grade (World Health Organization Grade III) mixed glioma.

After administration of appropriate neuromuscular blockade and based on the treatment planning, focal ablative IRE lesions were created in the tumor using the NanoKnife® (AngioDynamics, Queensbury, NY USA), and blunt tip electrodes. The NanoKnife® is an electric pulse generator in which the desired IRE pulse parameters (voltage, pulse duration, number of pulses, and repetition rate) are entered. The NanoKnife® is also designed to monitor the resulting current from the treatment and to automatically suspend the delivery of the pulses if a current threshold is exceeded. The electrodes were inserted into the tumor tissue in preparation for pulse delivery. The blunt tip electrodes were connected via a 6-foot insulated wire (cable) to the generator. After foot pedal activation, the pulses were conducted from the generator to the exposed electrodes.

8.3.4 RADIOTHERAPY (RT) PLANNING

Radiotherapy planning was executed using MRI images obtained from the 48-hour post-IRE MRI (Figure 40). The MRI images were imported into a 3-D computerized treatment planning system (Topslane WiMRT, TGM2, Clearwater, FL, USA). A 3-D treatment plan was created using forward planning and 4 portals. The plan focused on delivering 2.5 Gy per fraction to the area of enhancement including surgical incision plus a 5 mm margin of normal tissue as identified on the T1 + gadolinium transverse images. The tolerance dose for 5% complication in 5 years for irradiation of 1/3 of the brain volume is estimated at 60 Gy [72]. Protocols for daily definitive radiation therapy of brain tumors in veterinary medicine are commonly fractionated into 3 Gy per fraction for a total dose of 48 Gy to 54 Gy. The protocol created for this patient used a decreased dose per fraction with the intent to lower the risk of late effects given the volume of brain in the irradiated field. The protocol was 2.5 Gy per fraction, 20 fractions, for a

total dose of 50 Gy. Two treatment days had double treatments separated by 6 hours. These double treatment days were to account for days missed due to holidays. X-rays were delivered by a Varian Clinac4® linear accelerator (Palo Alto, California, USA). The patient positioning was confirmed by portal imaging.

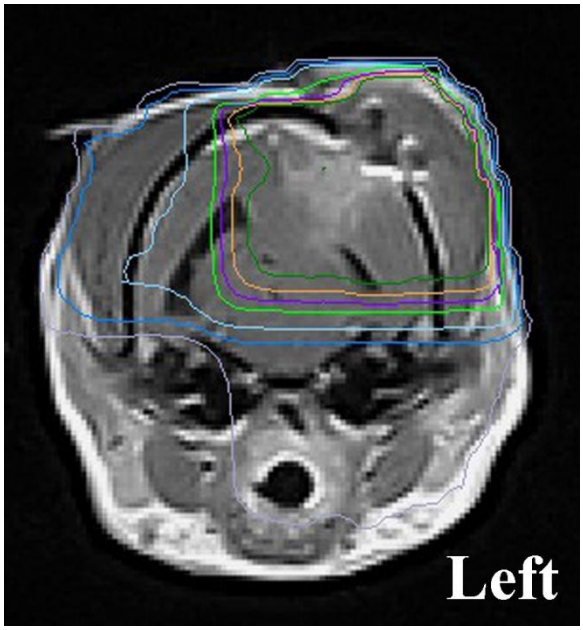

Figure 40: Representative, 48 post IRE therapy MRI image used for radiotherapy planning demonstrating isocenter and isodose distribution. The 100%, 98%, 95%, 90%, 70%, 50% and 30% isodose lines are delineated by the dark green, orange, purple, light green, light blue, dark blue, and gray traces, respectively. Published with permission from Adenine Press as described in page 93.

8.4 RESULTS

The total operative time for the craniectomy was 106 minutes, of which 12 minutes were required for completion of the IRE therapy. The patient recovered from the IRE craniectomy procedure without complication, and was maintained in the intensive care unit on parenteral opioid analgesics and phenobarbital. Post-operatively, no adverse clinical effects were observed in the patient. An MRI examination performed 48 hours after IRE therapy (Figure 41) revealed a reduction in the size of the neoplasm by approximately 75 percent (Table 11), based on volumetric calculations determined from pre- and post-IRE MRI studies using the methods reported in the IRE Treatment Planning section. This suggests that the field strength to kill malignant tissue is significantly lower than for normal tissue, which implies that IRE may

have some selectivity in the brain. There was also improvement in the previously noted mesencephalic compression secondary to the transtentorial herniation, as well as a reduction in the amount and extent of perilesional edema.

Table 11: Tumor volumes calculated pre- and 48 hours post IRE ablation from post-contrast T1 MRI.

PLANE	PRE IRE (cm^3)	POST IRE (cm^3)	REDUCTION (%)
Axial	1.15	0.32	72.2
Sagittal	1.68	0.42	75.1
Dorsal	1.25	0.32	74.7
Average	1.36	0.35	74.2
St.Dev	0.28	0.06	

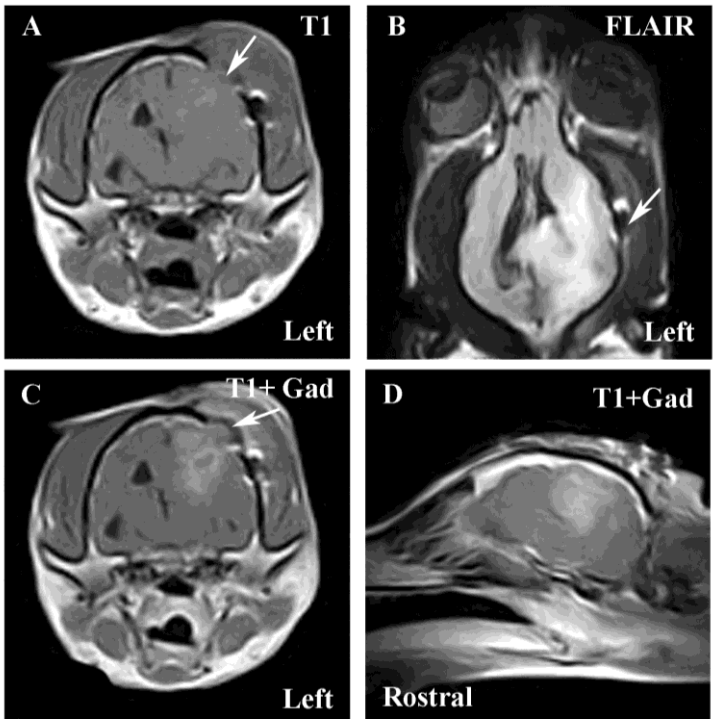

Figure 41: MRI examination performed on canine glioma patient 48 hours post-IRE therapy illustrating a reduction in tumor volume. Panels A-D (A- axial T1 pre-contrast; B- Dorsal FLAIR; C- axial T1 post-contrast; D- left parasagittal T1 post-contrast) are homologous images to those provided in panels A-D of Fig. 1, and the limited craniectomy defect is visible in panels A, B, and C (arrows). Published with permission from Adenine Press as described in page 93.

By post-operative day 5, the patient's neurological status improved, with resolution of the previous right sided hemiparesis, and propulsive circling, and improvement in the previously noted aggression. The visual deficits remained static in the right eye. The dog developed aspiration pneumonia, which resolved with antimicrobial and pulmonary toilet therapies. The dog was discharged to the owner on the 10th post-operative day, with instructions to administer phenobarbital and levetiracetam for the symptomatic seizures, and corticosteroids for peritumoral edema.

Sixteen days post-operatively the patient began fractionated radiotherapy, receiving a total of 50 Gy delivered as 20 treatments of 2.5 Gy each, using a 4 MeV linear accelerator (Varian Clinac4® Palo Alto, California, USA). The patient was treated once daily Monday through Friday following induction of general anesthesia. The patient was observed to be mentally brighter, more alert and better oriented by the 5th treatment. After treatment 11, the dog had two seizures that responded to diazepam therapy. Mannitol was incorporated into the anesthesia for the following two treatments and no additional seizures occurred through the rest of the RT treatment. The patient was ataxic and seemed to be less visual for the next few days, but this resolved over the next week. Throughout treatment, despite noticeable improvement, the patient remained aggressive and mildly disoriented.

Following completion of radiotherapy, the patient developed evidence of cognitive dysfunction, manifesting as lack of awareness of familiar people and environments, blunted responses to verbal commands, and disturbed sleep-wake cycles. These cognitive deficits, as well as the previously documented visual deficits in the right eye remained static during recheck examinations performed 2 and 4 months following the performance of the IRE treatment, and were not responsive to corticosteroid therapy. The patient was determined to be in complete remission following demonstration of no visible tumor on the 4 month post-IRE MRI examination (Figure 42).

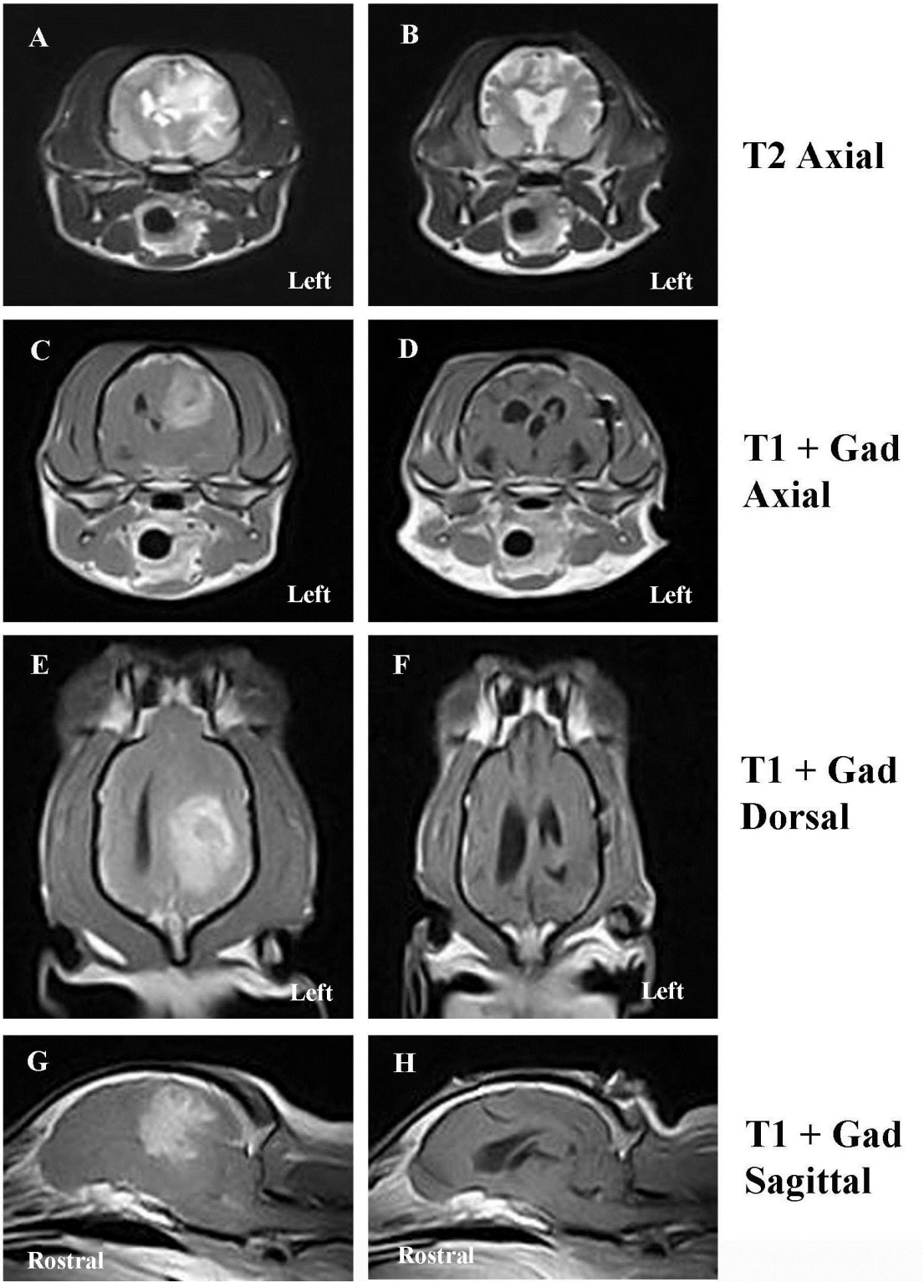

Figure 42: Comparative pre-operative (left panels A, C, E, G) and 4-month post-IRE (right panels B, D, F, H) MRI examinations. There is no evidence of the previously visualized left cerebral MG evident on the 4 month MRI scan. Published with permission from Adenine Press as described in page 93.

Thirteen days following the documentation of complete remission (approximately 4.5 months post-IRE therapy) the dog was presented for evaluation of an acute deterioration in mentation, proprioceptive ataxia and dysequilibrium, and circling to the left, which were attributed to a multifocal brain disorder. An MRI examination of the brain performed at that time revealed a focal cortical depression in the region of the previous IRE therapy, as well as marked T2 and FLAIR hyperintensity (Figure 43A-C) within the white and gray matter surrounding the previous tumor site, as well as bilaterally symmetric T2 and FLAIR hyperintensites involving hippocampus and pyriform lobes (Figure 43A and 36B) of the cerebrum, the internal capsule, optic radiations, and corpus callosum (Figure 43C). These lesions were iso- to mildly hypointense on T1 images, and demonstrated mild to moderate heterogeneous enhancement following intravenous administration of gadolinium. The cumulative clinical and MRI findings were considered suggestive of early-delayed radiation encephalopathy, although recurrent MG could not be excluded.

Anti-edema therapy with parenteral corticosteroids, osmotic, and loop diuretics was instituted and continued for 8 days, but the dog's clinical status continued to deteriorate. The dog was humanely euthanized at the owner's request by intravenous barbiturate overdosage, with an overall survival in this patient of 149 days after performance of IRE therapy.

Gross post-mortem examination revealed an extensive tan-brown necrotic focus in the left fronto-parietal lobes of the cerebrum (Figure 43D). Microscopically, extensive and geographic regions of coagulative brain necrosis and dystrophic calcification were observed, with the epicenter located in the left parietal lobe in the original location of the MG (Figure 43). Necrotic regions extended bilaterally into the hippocampus and pyriform lobes, contained hemorrhage, multiple foci of gemistocytic astrocytosis and spheroids, and were commonly infiltrated with hemosiderin laden macrophages (Figure 43F). Multifocal regions of vascular telangiectasias (Figure 43F), vascular hyalinization and microhemorrhage were noted within necrotic areas. White matter pallor and edema were noted to be marked in the epicentric region of necrosis but were also present, although more moderate, rostrally and caudally along the fibers of the internal capsule, optic radiation, and corpus callosum in both the left and right

cerebral hemispheres. No evidence of recurrent MG was observed on post-mortem examination. The post-mortem changes were interpreted as consistent with early-delayed radionecrosis of the brain.

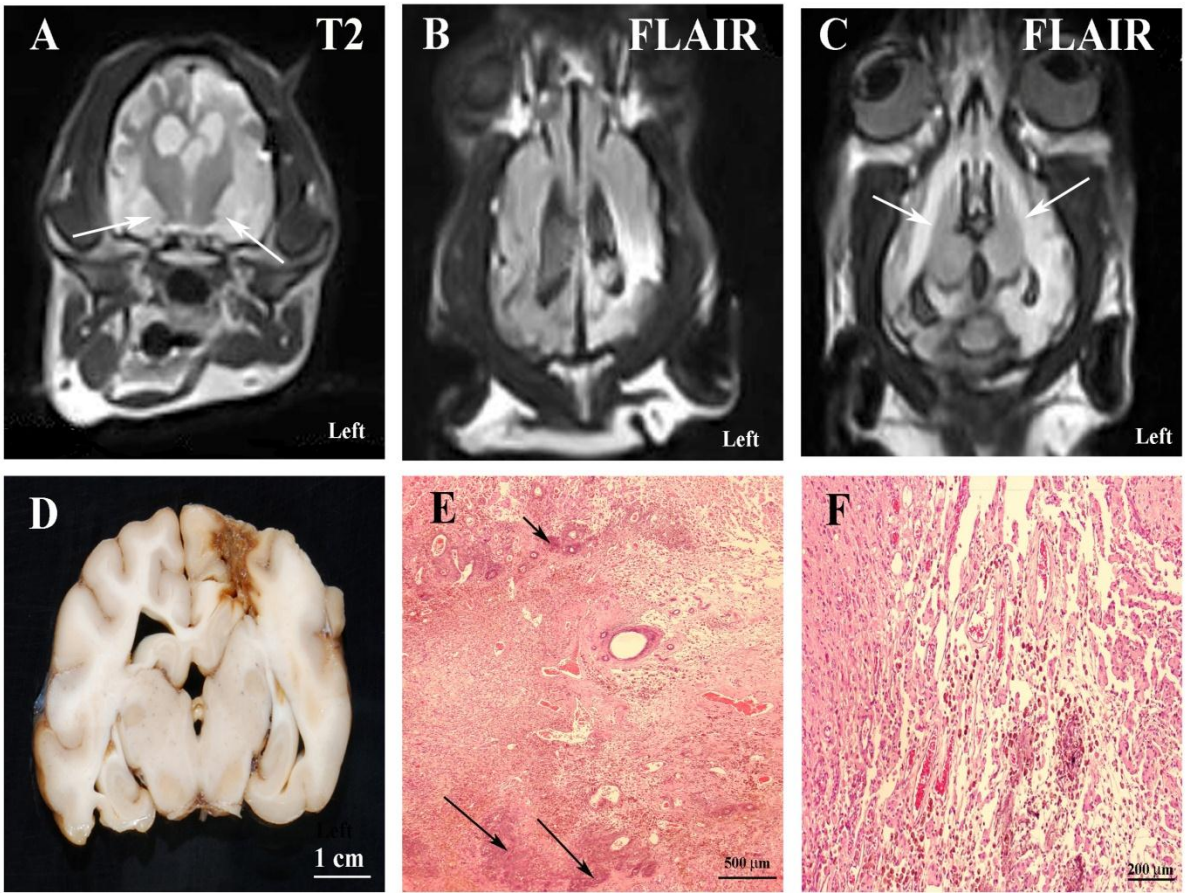

Figure 43: Axial T2 (A) and dorsal FLAIR (B and C) MRI sequences and post-mortem pathology (D-F) of delayed radiation brain necrosis. Marked T2 (A) and FLAIR (B) signal hyperintensity involving the ipsilateral gray and white matter in region of the previous tumor on the left, as well as bilateral involvement of the pyriform lobes (A; arrows) and white matter of the internal capsule (C; arrows). There is marked signal change evident in the region of the previous tumor when Fig.6B is compared to the homologous FLAIR image (Fig. 5F) obtained at the 4 month recheck. (D) A tan focus of necrosis is evident in the left parietal lobe in the region of the previous tumor. (E) Geographic area of coagulative necrosis with dystrophic calcification (arrows; H&E stain). (F) Vascular telangiectasia and hemosiderin laden macrophages within necrotic region of neuropil (H&E stain). Published with permission from Adenine Press as described in page 93.

8.5 DISCUSSION

Despite advances in cancer treatment, MG remains highly resistant to therapy. By nature of their neuroinvasiveness, MG are often not amenable to curative surgery and recur with high frequency [105, 175, 176]. Even with aggressive multimodal treatment most patients succumb to the disease within one year. The 5-year survival rate for human patients with GBM is 10% and this statistic has remained nearly unchanged over the last five years [176]. Although much less is known regarding the effects of single or multimodal therapies on the survival of dogs with gliomas, the prognosis is considered poor for dogs with MG, with one study reporting a median survival of 9 days for all dogs with non-meningeal origin neoplasms [74]. This is the first report of application of IRE for *in vivo* treatment of spontaneous intracranial MG. Adjunctive radiotherapy, anti-edema treatment, and anticonvulsants were subsequently and concurrently administered to provide comprehensive multimodal therapy. Complete remission was achieved in this canine patient based on serial MRI examinations of the brain and post-mortem examination.

We performed a safe, minimally-invasive IRE procedure at the time of tumor biopsy in this patient based on treatment parameters from the numerical models and preliminary data in normal brain [51, 61, 64]. Usage of IRE ablation was considered advantageous for this case, as the large tumor volume precluded complete traditional surgical excision without the potential for significant perioperative morbidity associated with brain manipulation. The procedure resulted in rapid improvement of the patient's neurological signs, which allowed for safe administration of adjunctive post-operative fractionated radiotherapy (RT). We are unable to attribute the clinical improvement entirely to IRE treatment as the patient simultaneously underwent a decompressive craniectomy that provided a reduction in intracranial pressure. However, a limited craniectomy was performed, and two days after the IRE ablation the tumor size was reduced by approximately 75 percent and there was marked reduction in peritumoral edema seen on MRI. Of additional importance is that this patient had evidence of spontaneous, tumor-associated intracerebral hemorrhage on pre-operative MRI sequences. Post-operative MRI showed no additional hemorrhage, further supporting the vascular-sparing nature of IRE treatment [51, 61]. It is important to note that there is only one data point between the IRE

procedure and RT so it is difficult to evaluate the independent effects of the pulses. IRE induces an immune response in tissues [110, 143] including the brain [51] that could have contributed to the reduction in tumor size and/or complete remission. Future experiments will investigate the effects of IRE therapy alone for the treatment of brain cancer.

IRE is a novel minimally invasive technique to focally ablate undesired tissue using low energy electric pulses [1]. These pulses permanently destabilize the membranes of the tumor cells, inducing death without thermal damage in a precise and controllable manner with sub-millimeter resolution [1, 2, 37, 71]. The application of IRE requires minimal time and can be performed at the time of surgery, as in this case, or using stereotactic image (i.e. CT or MRI) guidance [63]. This is an ideal treatment strategy for many canine brain tumor patients where either tumor volumes are often sufficiently large, as in this case, to preclude safe traditional surgical excision without associated significant perioperative morbidity; or excision is not possible due to the neuroanatomic location of the tumor. We believe that, in addition to the ability to effectively ablate tissue without heating, a major advantage of IRE treatment is the very sharp transition between treated and non-treated tissue, which allows for sparing of sensitive neuroanatomic structures in proximity to the treatment field. Numerical models will be used in subsequent investigations in order to establish the value at which this transition occurs in brain tumor tissue.

Clinical experience and the medical literature indicate that focal ablative or cytoreductive techniques, including IRE, are of limited independent use in the treatment of MG due in part to their inherent locoregional neuroinvasive behavior [105, 152, 176]. However, as illustrated here, IRE appears to be an additional and viable technique available to the neurosurgeon when a rapid reduction in tumor volume and intracranial hypertension is clinically necessary. In addition, the advantages of IRE as a focal ablative technique may have applications in treatment of benign intracranial tumors, such as meningiomas, particularly those located in anatomic locations that are difficult to approach, where residual microscopic disease following traditional surgery often leads to recurrence.

With IRE there is a region of non-destructive increase in membrane permeability that occurs outside the zone of irreversible tissue ablation [36]. The temporary increase in membrane permeability of tissues within this reversibly electroporated penumbra could potentially be used to optimize local delivery of cytotoxic compounds for targeted death of neoplastic cells [68, 75]. Microscopic infiltration of tumor cells into the brain parenchyma surrounding gross tumor foci are pathological hallmarks of MG and GBM [105, 175], and a significant limiting factor when employing local therapeutic techniques, including IRE, that are based upon resection or *in situ* destruction of macroscopic tissue in a biologically sensitive tissue, such as the brain. Therefore, capitalizing on the ability to deliver otherwise impermeant therapeutic agents to cells within the reversibly electroporated penumbra is another tremendous possible advantage of IRE for the treatment of MG and brain disease in general.

Documentation of complete remission following therapy for histopathologically confirmed intracranial glioma is extremely rare (or rarely reported) in veterinary medicine. Unfortunately, although complete remission was documented in this case, clinical and MRI evidence of progressive radiation necrosis developed, and ultimately caused the death of the patient. The ante-mortem MRI and post-mortem pathologic changes noted in this case were similar to those reported in human beings with early-delayed types of radionecrosis of the brain [20, 104]. Delayed side effects of radiotherapy are often permanent and develop months to years after the cessation of treatment [104, 169]. Cognitive impairment and radionecrosis of the brain are not commonly recognized in canine patients after RT with doses and fractions similar to those prescribed in the patient described here (personal communication with Dr. Nancy Gustafson, February 2010). Compared to humans, there is a paucity of published data available describing the incidence of or risk factors associated with the development of delayed radiation encephalopathies in dogs with spontaneous brain tumors. The incidence of radiation necrosis in adult humans after conventional doses used for brain tumor treatment ranges from 5 to 24%, but this complication is considered rare when cumulative doses of standard fractionated radiation less than 50-60 Gy are delivered to the brain [20, 104]. Several recognized risk factors associated with the development of post-RT associated neurological complications in humans were present in the patient reported here including advanced age,

large volume of brain irradiated, and >2 Gy fractions administered [4, 28, 169]. However, non-necrotizing radiation encephalopathies manifesting as neurobehavioral disorders are more common than radiation induced necrosis, and may occur at doses as low as 20 Gy in adult humans [28, 169]. Given that progressive radionecrosis of the brain resulted in the death of this patient, we must recognize the possibility that IRE therapy may have some radiosensitizing or other synergistic interaction with external beam RT. Although this may enhance therapeutic effectiveness of RT, it could also predispose to the development of delayed radiation complications in patients with brain disease if administered using current and conventional dosing regimens.

8.6 CONCLUSION

This chapter showed that treatment of canine MG with IRE is rapid, minimally invasive, and effective for ablation of pathologically heterogeneous neoplastic brain tissue without exacerbating intracerebral hemorrhage. In addition, this work demonstrates that IRE can be successfully planned and executed with clinical procedures routinely used during evaluation of the neurosurgical patient. In our patient, IRE ablation was an integral part of a comprehensive multimodality therapeutic regimen that resulted in complete remission from the MG. Our preliminary results justify continued research and development of IRE therapy for the ablation of unwanted brain tissue, and highlight the need for investigations into possible interactions of IRE with other anticancer therapies commonly used in the management of brain tumor patients, such as radio- and chemotherapy.

CHAPTER 9 - SUMMARY

9.1 INTRODUCTION

Irreversible electroporation is a new minimally invasive method at ablating tissue in a non-thermal manner using low-energy electric pulses. The technique involves introducing electrodes into and around the region of interest and delivering a train of high-voltage low duration pulses. This technique has been shown to have promise in the treatment of several types of soft tissue pathologic masses including hepatic, renal, prostate and lung cancer.

The goal of this dissertation was to determine the feasibility and efficacy of using irreversible electroporation for the treatment of brain cancer, specifically aggressive high-grade gliomas. To accomplish this we performed several *in vivo* and *ex vivo* experiments that allowed us to generate and validate numerical models for treatment planning and outcome assessment. In addition, we determined that the procedure is safe to use in the brain and that it can be performed with CT and other imaging methods to confirm electrode placement and assess treatment outcome.

9.2 WHAT THIS DISSERTATION ACCOMPLISHED

In this dissertation we hypothesize that irreversible electroporation is capable of ablating normal (gray and white matter) and pathological (MG and/or GBM) brain tissue in a highly focused non-thermal manner that is modulated through pulse parameters and electrode configuration. Through a comprehensive experimental and numerical investigation, we tested and attained results strongly supporting our hypothesis. Specifically, we developed numerical models that were capable of simulating an entire IRE treatment protocol and would take into account pulse parameters (e.g. duration, frequency, repetition rate and strength) in addition to the dynamic changes in tissue electrical conductivity due to electroporation and joule heating, as well as biologically relevant processes such as blood perfusion and metabolic heat. We also provided a method to isolate the IRE effects from undesired thermal damage in models that were validated with real-time temperature measurements during the delivery of the pulses. Finally we outlined a procedure to use 3D volumetric reconstructions of IRE lesions using patient specific MRI scans in conjunction with the models described for establishing field thresholds or performing treatment planning prior to the surgical procedure; thus supplying the

readers with the tools and understanding necessary to design appropriate treatment protocols for their specific application.

Experimentally we presented the first systematic *in vivo* study of IRE in normal canine brain and the multimodal treatment of a canine MG patient. We confirmed that the procedure can be applied safely in the brain and was well tolerated clinically. The lesions created with IRE were sub-millimeter in resolution and we achieved 75% tumor volume reduction within 3 days post-IRE in the patient. In addition to the sharp delineation between necrotic and normal brain, the treatments spared the major blood vessels, making it appropriate for treatment of tumors adjacent to, or enveloping critical vascular structures.

In Chapter 3 we presented the theoretical background necessary to develop numerical models for IRE treatment planning and execution including the generation of pulsed electric field and temperature distributions. These in turn could be used to evaluate the volume of tissue treated with IRE and determine if the thermal effects can damage tissue by hyperthermic mechanisms.

In Chapter 4 we performed *ex vivo* experiments on canine brain tissue in which we delivered a typical IRE protocol and measured the resulting temperature increase simultaneously. This data was extremely valuable since it allowed for the validation of the numerical models that were being used to predict temperature increase and assess thermal damage. In addition, the models used report on the volume of tissue treated by IRE and experiencing thermal damage by using a conductivity function that was dependent on temperature changes.

In Chapter 5 we experimentally tested the safety of using IRE in normal canine brain which is the most relevant animal model for brain cancer in humans. In these experiments we explored the ability to modulate the size of the lesions by using three different voltages and the clinical outcome of the patients. Our results suggested that the dogs did not experience any clinically adverse effects and their neurological evaluation before and after irreversible electroporation were identical. In addition, we spared the major vasculature and generated lesions that were highly focused and sharply delineated from normal tissue. These results gave

us confidence in the procedure and provided us with the surgical experience to perform treatments in canine patients.

Chapter 6 capitalized on the electric current measurements during the *in vivo* procedures of the previous chapter which were incorporated into the numerical models developed in Chapter 4. In addition, we used the MRI scans of the lesions and generated 3D volumetric reconstructions that were correlated with electric field distributions from the models. The models in this chapter included the dynamic electric conductivity that depended on joule heating and electropermeabilization, and also accounted for metabolic heat generation and blood perfusion. It is in this chapter that we first proposed 500 V/cm as an IRE threshold in gray matters using specific pulse parameters (e.g. ninety 50-µs pulses at a frequency of 4 Hz), electrode configuration and assumptions in our numerical model.

Chapter 7 built on our previous intracranial experiments in normal canine brain and outlined the computed tomographic guidance IRE procedure that was performed through 1.2 mm burr holes. In this procedure, for the first time ever, the temperature was measured during the delivery of the pulses at the electrode tissue interface in order to experimentally confirm the non-thermal aspect of the procedure. Finally, we performed a parametric study of the volumetric effects of applied voltage and pulse repetition rate (frequency) in terms of tissue ablated by IRE and experiencing undesired thermal effects. We provided a method of calculating and visualizing both of these quantities as a function of time which can be used to optimize IRE pulse protocols in order to maximize treatment size and avoid any thermal damage.

Finally in Chapter 8 we reported on the treatment of the first brain cancer patient treated with IRE, specifically for a non-resectable malignant high-grade glioma. The intent of the procedure was to reduce to tumor size significantly in order to improve the clinical condition of the dog with the intent of allowing the dog to undergo radiation therapy. The treatment planning was performed by isolating the tumor geometry from the MRI scans and reconstructing a 3D geometry of the tumor for use in the numerical models. The patient recovered well from the IRE procedure and we calculated the tumor volume to be 75 % smaller than the original one which was impressive and it reduced most of the clinical signs that

resulted from the increased intracranial pressure. After undergoing an intense radiation regimen, at 4-months post combinatorial IRE and high-dose radiation therapy the brain tumor was found to be in complete remission. This study showed the potential of irreversible electroporation to ablate pathological tissue and aid in the clinical outcome. Unfortunately, the patient developed a rare complication of RT called radiation necrosis and was humanely euthanized at the owner's request. This experience continues to motivate our work in order to develop irreversible electroporation as one of the standard brain cancer treatments either in isolation or in combination with other modalities in order to keep helping brain cancer patients, both canine and humans.

9.3 FUTURE WORK

Irreversible electroporation is a new, minimally invasive focal ablation technique for treating tumors [1, 36, 49]. It currently has US FDA 510(k) approval for soft tissue ablation and has only been used by our team for treatment of central nervous system diseases. We conducted the first pilot study on three canine subjects to verify the safety of such a procedure in the brain [51, 61]. Our results show that IRE spares the major vasculature in the brain and creates a sharp delineation between treated and untreated tissue. An MRI using a 7.0 T magnet demonstrated the focal nature of the lesion created. The focal nature of the IRE procedure precludes safety concerns of undue electrical stimulation of the brain, widespread disruption of the blood brain barrier, and neuronal damage. Recently our team also treated an inoperable high-grade glioma on a canine patient at the Virginia-Maryland Regional College of Veterinary Medicine for the first time [65]. The IRE pulse generator delivers a series of low energy electric pulses through needle-like electrodes targeted within the tumor volume. These pulses permanently destabilize the membranes of the tumor cells, inducing death without thermal damage in a precise and controllable manner with sub-millimeter resolution [51]. In summary, our team has demonstrated the feasibility of using IRE for brain cancer and has treated the first canine patient with spontaneous GBM, which is an excellent translational model for human GBM.

9.3.1 Establishing the electric field needed for brain tumor ablation

In this dissertation we outlined a method of determining the electric field threshold for ablating normal brain tissue. In addition, we presented numerical models capable of generating electric field distribution that take into account all of the biological and physical phenomena that occur during IRE. However, normal tissue behaves differently than tumor tissue due to the leaky and immature blood vessels that normally are created in neoplastic tissue in order to compensate for the excessive nutrient demands. Consequently, for accurate treatment planning and execution, it is imperative to determine the physical properties and the electric field intensity needed to ablate brain cancer tissue. This can be done with similar reconstructions techniques from the MRI images taken post-IRE as described in Chapter 6.

9.3.2 Determining the non-linear conductivity effects of electroporation in brain tissue

Electroporation results in an increase in membrane permeability and thus in electrical conductivity. In the models that we have generated we have incorporated these changes by using reports from other organs in which this change has been measured. Nevertheless, the degree of conductivity change with applied voltage needs to be measured experimentally in brain (normal and pathologic) in order to modify the parameters used in the models. A way to achieve this is to monitor the total current that is being delivered during an IRE procedure and incorporating the data into the numerical models. Additionally, the impedance can be measured before, during and after by additional electrodes to the ones used during the IRE treatment. In this manner, the numerical models can be adjusted accordingly in order improve the accuracy of the treatment planning and outcome.

9.3.3 Determine the electric field needed for delivery of agents during an IRE procedure

IRE creates a sharply delineated volume of ablated tissue with sub-millimeter resolution. Outside the zone of tissue ablation, there is a penumbra of non-destructive increase in membrane permeability [36]. The cells outside the zone of ablation but within this penumbra are more susceptible to exogenous agents such as chemotherapy. It is often infiltrative glioma cells that show an increase in their proliferation rates and relative resistance to therapy as compared to the highly cellular center of the tumor. Thus, IRE may be an ideal treatment for GBM due to its ability to destroy tumor cells within a discrete zone while increasing

susceptibility to exogenous agents for a range outside the zone of ablation. Using IRE to either destroy the tumor or increase the delivery of chemotherapeutic agents into infiltrative tumor cells beyond the IRE ablated zone should therefore result in complete tumor regression. We believe that there is a significant penumbra of increased permeability surrounding the IRE ablative region that can be optimized to target treatment of highly infiltrative tumor cells, resulting in a powerful combination strategy for treating humans with GBM. Therefore, defining the pulse parameters of IRE necessary to produce BBB disruption and to estimate the duration of the reversible effects on BBB disruption are needed. By obtaining this minimal pulse parameters necessary for effective opening of the BBB and to obtain an estimate of the duration and extent of reversible effects on BBB opening, a powerful combinatorial approach can be developed in order treat ablate most of the tumor while targeting the highly infiltrative cells at the margins.

9.4 CONCLUSION

We have presented the experimental and numerical results of performing irreversible electroporation in normal and pathologic brain. Our results confirm that IRE can be used to generate lesions in a highly focused and precise manner and that it is able to kill both normal and tumor tissue. Thus, numerical models are crucial in the treatment planning and execution stages in order to optimize pulse protocol for maximizing tumor ablation while minimizing damage to surrounding tissue. We provide all of the necessary tools for IRE treatment planning using patient-derived tumor geometries and have demonstrated the potential of IRE for clinical applications in brain cancer patients, specifically high-grade glioma. We believe that in the next couple years, IRE will be incorporated into the treatment of these patients either alone or in combination with other treatment modalities in order to ablate these highly aggressive tumors and target the highly infiltrative cells that are responsible for tumor recurrence.

CHAPTER 10 - REFERENCES

1. Al-Sakere, B., F. Andre, C. Bernat, E. Connault, P. Opolon, R.V. Davalos, B. Rubinsky, and L.M. Mir, *Tumor ablation with irreversible electroporation.* PLoS ONE, 2007. 2(11):e1135.
2. Al-Sakere, B., C. Bernat, F. Andre, E. Connault, P. Opolon, R.V. Davalos, and L.M. Mir, *A study of the immunological response to tumor ablation with irreversible electroporation.* Technology in Cancer Research and Treatement, 2007. 6:301-306.
3. Al-Waili, N.S. and G.J. Butler, *Phototherapy and malignancy: possible enhancement by iron administration and hyperbaric oxygen.* Med Hypotheses, 2006. 67(5):1148-58.
4. Asai, A. and K. Kawamoto, *[Radiation-induced brain injury].* Brain Nerve, 2008. 60(2):123-9.
5. Atsumi, H., M. Matsumae, M. Kaneda, I. Muro, Y. Mamata, T. Komiya, A. Tsugu, and R. Tsugane, *Novel laser system and laser irradiation method reduced the risk of carbonization during laser interstitial thermotherapy: assessed by MR temperature measurement.* Lasers Surg Med, 2001. 29(2):108-17.
6. Atwood, T., V.S. Payne, W. Zhao, W.R. Brown, K.T. Wheeler, J.M. Zhu, and M.E. Robbins, *Quantitative magnetic resonance spectroscopy reveals a potential relationship between radiation-induced changes in rat brain metabolites and cognitive impairment.* Radiat Res, 2007. 168(5):574-81.
7. Baker, P.F. and D.E. Knight, *Calcium-dependent exocytosis in bovine adrenal medullary cells with leaky plasma membranes.* Nature, 1978. 276(5688):620-2.
8. Ball, C., K.R. Thomson, and H. Kavnoudias, *Irreversible electroporation: a new challenge in "out of operating theater" anesthesia.* Anesth Analg, 2010. 110(5):1305-9.
9. Becker, S.M. and A.V. Kuznetsov, *Numerical modeling of in vivo plate electroporation thermal dose assessment.* Journal of Biomechanical Engineering, 2006. 128(1):76-84.
10. Becker, S.M. and A.V. Kuznetsov, *Thermal damage reduction associated with in vivo skin electroporation: A numerical investigation justifying aggressive pre-cooling.* International Journal of Heat and Mass Transfer, 2007. 50:105-116.
11. Beebe, S.J., J. White, P.F. Blackmore, Y. Deng, K. Somers, and K.H. Schoenbach, *Diverse effects of nanosecond pulsed electric fields on cells and tissues.* DNA Cell Biol, 2003. 22(12):785-796.
12. Belehradek, M., C. Domenge, B. Luboinski, S. Orlowski, J. Belehradek, and L.M. Mir, *Electrochemotherapy, a new antitumor treatment - 1st clinical phase-I-II trial.* Cancer, 1993. 72(12):3694-3700.
13. Belov, S.V., *Effects of high-frequency current parameters on tissue coagulation.* Biomedical Engineering, 1978. 12:209-211.
14. Berger, M.S., *Malignant astrocytomas: surgical aspects.* Semin Oncol, 1994. 21(2):172-85.
15. Biedermann, W., *Electrophysiology*. Vol. 2. 1898, London: Macmillan.
16. Bock, H.C., M.J. Puchner, F. Lohmann, M. Schutze, S. Koll, R. Ketter, R. Buchalla, N. Rainov, S.R. Kantelhardt, V. Rohde, and A. Giese, *First-line treatment of malignant glioma with carmustine implants followed by concomitant radiochemotherapy: a multicenter experience.* Neurosurg Rev, 2010. 33(4):441-9.

17. Borrelli, M.J., L.L. Thompson, C.A. Cain, and W.C. Dewey, *Time-temperature analysis of cell killing of BHK cells heated at temperatures in the range of 43.5 degrees C to 57.0 degrees C.* International Journal of Radiation Oncology Biology Physics, 1990. 19(2):389-399.
18. Brown, S.L., J.W. Hunt, and R.P. Hill, *Differential thermal sensitivity of tumor and normal tissue microvascular response during hyperthermia.* International Journal of Hyperthermia, 1992. 8(4):501-514.
19. Bryant, G. and J. Wolfe, *Electromechanical stresses produced in the plasma membranes of suspended cells by applied electric fields.* J Membr Biol, 1987. 96(2):129-39.
20. Burger, P.C., M.S. Mahley, Jr., L. Dudka, and F.S. Vogel, *The morphologic effects of radiation administered therapeutically for intracranial gliomas: a postmortem study of 25 cases.* Cancer, 1979. 44(4):1256-72.
21. Cha, S., *Neuroimaging in neuro-oncology.* Neurotherapeutics, 2009. 6(3):465-77.
22. Cherubini, G.B., P. Mantis, T.A. Martinez, C.R. Lamb, and R. Cappello, *Utility of magnetic resonance imaging for distinguishing neoplastic from non-neoplastic brain lesions in dogs and cats.* Vet Radiol Ultrasound, 2005. 46(5):384-7.
23. Chizmadzhev, Y.A., V.B. Arakelyan, and V.F. Pastushenko, *Electric Breakdown of Bilayer Lipid-Membranes .3. Analysis of Possible Mechanisms of Defect Origination.* Bioelectrochemistry and Bioenergetics, 1979. 6(1):63-70.
24. Chizmadzhev, Y.A., V.G. Zarnitsin, J.C. Weaver, and R.O. Potts, *Mechanism of electroinduced ionic species transport through a multilamellar lipid system.* Biophys J, 1995. 68(3):749-65.
25. Cosman, E.R., B.S. Nashold, and P. Bedenbaugh, *Stereotactic radiofrequency lesion making.* Appl Neurophysiol, 1983. 46(1-4):160-6.
26. Cosman, E.R., Jr. and E.R. Cosman, Sr., *Electric and thermal field effects in tissue around radiofrequency electrodes.* Pain Med, 2005. 6(6):405-24.
27. Coster, H.G.A., *Quantitative analysis of the voltage-current relationship of fixed charge membranes and the assosciated property of "punch-through".* Biophys. J., 1965. 5:669-686.
28. Crossen, J.R., D. Garwood, E. Glatstein, and E.A. Neuwelt, *Neurobehavioral sequelae of cranial irradiation in adults: a review of radiation-induced encephalopathy.* J Clin Oncol, 1994. 12(3):627-42.
29. Crowley, J.M., *Electrical breakdown of biomolecular lipid membranes as an electromechanical instability.* Biophysical Journal, 1973. 13:711-724.
30. Cukjati, D., D. Batiuskaite, F. Andre, D. Miklavcic, and L.M. Mir, *Real time electroporation control for accurate and safe in vivo non-viral gene therapy.* Bioelectrochemistry, 2007. 70(2):501-7.
31. Damianou, C., K. Hynynen, and X. Fan, *Application of the thermal dose concept for predicting the necrosed tissue volume during ultrasound surgery.* Ultrasonics Symposium, 1993.
32. Davalos, R.V., D.M. Otten, and B. Rubinsky, *A feasibility study for electrical impedance tomography as a means to monitor tissue electroporation for molecular medicine.* IEEE Transactions on Biomedical Engineering, 2002. 49(4):400-403.
33. Davalos, R.V., B. Rubinsky, and L.M. Mir, *Theoretical analysis of the thermal effects during in vivo tissue electroporation.* Bioelectrochemistry, 2003. 61(1-2):99-107.

34. Davalos, R.V., D.M. Otten, L.M. Mir, and B. Rubinsky, *Electrical impedance tomography for imaging tissue electroporation.* IEEE Transactions on Biomedical Engineering, 2004. 51(5):761-767.
35. Davalos, R.V. and B. Rubinsky, *Electrical impedance tomography of cell viability in tissue with application to cryosurgery.* Journal of Biomechanical Engineering, 2004. 126(2):305-309.
36. Davalos, R.V., L.M. Mir, and B. Rubinsky, *Tissue ablation with irreversible electroporation.* Ann Biomed Eng, 2005. 33(2):223-31.
37. Davalos, R.V. and B. Rubinsky, *Temperature considerations during irreversible electroporation.* International Journal of Heat and Mass Transfer, 2008. 51(23-24):5617-5622.
38. DeBruin, K.A. and W. Krassowska, *Modeling electroporation in a single cell. II. Effects of ionic concentrations.* Biophys J, 1999. 77(3):1225-33.
39. DeBruin, K.A. and W. Krassowska, *Modeling electroporation in a single cell. I. Effects of field strength and rest potential.* Biophys J, 1999. 77(3):1213-24.
40. Deng, J.D., K.H. Schoenbach, E.S. Buescher, P.S. Hair, P.M. Fox, and S.J. Beebe, *The effects of intense submicrosecond electrical pulses on cells.* Biophysical Journal, 2003. 84(4):2709-2714.
41. Deng, Z.S. and J. Liu, *Blood perfusion-based model for characterizing the temperature fluctuations in living tissue.* Phys A STAT Mech Appl, 2001. 300:521-530.
42. Dev, S.B. and G.A. Hofmann, *Electrochemotherapy--a novel method of cancer treatment.* Cancer Treat Rev, 1994. 20(1):105-15.
43. Dewhirst, M.W., B.L. Viglianti, M. Lora-Michiels, M. Hanson, and P.J. Hoopes, *Basic principles of thermal dosimetry and thermal thresholds for tissue damage from hyperthermia.* Int J Hyperthermia, 2003. 19(3):267-94.
44. Dickinson, P.J., B.N. Roberts, R.J. Higgins, C.M. Leutenegger, A.W. Bollen, P.H. Kass, and R.A. LeCouteur, *Expression of receptor tyrosine kinases VEGFR-1 (FLT-1), VEGFR-2 (KDR), EGFR-1, PDGFRa and c-Met in canine primary brain tumours.* Veterinary and Comparative Oncology, 2006. 4(3):132-140.
45. Dickinson, P.J., R.A. LeCouteur, R.J. Higgins, J.R. Bringas, B. Roberts, R.F. Larson, Y. Yamashita, M. Krauze, C.O. Noble, D. Drummond, D.B. Kirpotin, J.W. Park, M.S. Berger, and K.S. Bankiewicz, *Canine model of convection-enhanced delivery of liposomes containing CPT-11 monitored with real-time magnetic resonance imaging: laboratory investigation.* J Neurosurg, 2008. 108(5):989-98.
46. Diller, K.R., *Modeling of bioheat transfer processes at high and low temperatures*, in *Bioengineering heat transfer*, Y.I. Choi, Editor. 1992, Academic Press, Inc: Boston. p. 157-357.
47. Doevenspeck, H., *Influencing cells and cell walls by electrostatic impulses.* Fleishwirtshaft, 1961. 13:986-987.
48. Duck, F.A., *Physical Properties of Tissues: A Comprehensive Reference Book*. 1990, San Diego: Academic Press.
49. Edd, J.F., L. Horowitz, R.V. Davalos, L.M. Mir, and B. Rubinsky, *In vivo results of a new focal tissue ablation technique: irreversible electroporation.* IEEE Trans Biomed Eng, 2006. 53(7):1409-15.

50. Edd, J.F. and R.V. Davalos, *Mathematical modeling of irreversible electroporation for treatment planning.* Technology in Cancer Research and Treatment, 2007. 6:275-286.
51. Ellis, T.L., P.A. Garcia, J.H. Rossmeisl, N. Henao-Guerrero, J. Robertson, and R.V. Davalos, *Nonthermal irreversible electroporation for intracranial surgical applications.* J Neurosurg, 2010:(in print).
52. Escoffre, J.M., T. Portet, L. Wasungu, J. Teissie, D. Dean, and M.P. Rols, *What is (still not) known of the mechanism by which electroporation mediates gene transfer and expression in cells and tissues.* Mol Biotechnol, 2009. 41(3):286-95.
53. Esser, A.T., K.C. Smith, T.R. Gowrishankar, and J.C. Weaver, *Towards solid tumor treatment by irreversible electroporation: intrinsic redistribution of fields and currents in tissue.* Technol Cancer Res Treat, 2007. 6(4):261-74.
54. Feng, Y., J. Tinsley Oden, and M.N. Rylander, *A two-state cell damage model under hyperthermic conditions: theory and in vitro experiments.* J Biomech Eng, 2008. 130(4):041016.
55. Finelli, A., J.C. Rewcastle, and M.A. Jewett, *Cryotherapy and radiofrequency ablation: pathophysiologic basis and laboratory studies.* Curr Opin Urol, 2003. 13(3):187-91.
56. Foster, R.S., R. Bihrle, N.T. Sanghvi, F.J. Fry, and J.P. Donohue, *High-intensity focused ultrasound in the treatment of prostatic disease.* Eur Urol, 1993. 23 Suppl 1:29-33.
57. Frankenhaueuser, B. and L. Widen, *Anode break excitation in desheated frog nerve.* J Physiol, 1956. 131:243-247.
58. Franquet, T., C.D. Miguel, R. Cozcolluela, and L. Donoso, *Spiculated lesions of the breast: mammographic-pathologic correlation.* Radiographics, 1993. 13:841-852.
59. Fuller, G.W., *Report on the investigations into the purification of the Ohio river water at Louisville Kentucky*. 1898, New York: D. Van Nostrand Company.
60. Gabriel, B. and J. Teissie, *Control by electrical parameters of short- and long-term cell death resulting from electropermeabilization of Chinese hamster ovary cells.* Biochim Biophys Acta, 1995. 1266(2):171-8.
61. Garcia, P.A., J.H. Rossmeisl, J. Robertson, T.L. Ellis, and R.V. Davalos, *Pilot study of irreversible electroporation for intracranial surgery.* Conf Proc IEEE Eng Med Biol Soc, 2009. 1:6513-6.
62. Garcia, P.A., R.E. Neal II, and R.V. Davalos, *Non-thermal irreversible electroporation for tissue ablation*, in *Electroporation in Laboratory and Clinical Investigations*, Enrico P. Spugnini and A. Baldi, Editors. 2010, Nova Science: Hauppauge, NY.
63. Garcia, P.A., R.E. Neal II, J.H. Rossmeisl, and R.V. Davalos, *Non-thermal irreversible electroporation for deep intracranial disorders.* Conf Proc IEEE Eng Med Biol Soc, 2010. 1:(in print).
64. Garcia, P.A., J.H. Rossmeisl, R.E. Neal II, T.L. Ellis, J. Olson, N. Henao-Guerrero, J. Robertson, and R.V. Davalos, *Intracranial nonthermal irreversible electroporation: In vivo analysis.* J Membr Biol, 2010. 236(1):127-136.
65. Garcia, P.A., T. Pancotto, J.H. Rossmeisl, N. Henao-Guerrero, N.R. Gustafson, G.B. Daniel, J.L. Robertson, T.L. Ellis, and R.V. Davalos, *Non-thermal irreversible electroporation (N-TIRE) and adjuvant fractionated radiotherapeutic multimodal therapy for intracranial malignant glioma in a canine patient.* Technol Cancer Res Treat, 2011. 10(1):1-11.

66. Gauger, B. and F.W. Bentrup, *A study of dielectric membrane breakdown in the fucus egg.* J. Membrane Biol., 1979. 48(3):249-264.
67. Glaser, R.W., S.L. Leikin, L.V. Chernomordik, V.F. Pastushenko, and A.I. Sokirko, *Reversible electrical breakdown of lipid bilayers: formation and evolution of pores.* Biochim Biophys Acta, 1988. 940(2):275-87.
68. Glass, L.F., M.L. Pepine, N.A. Fenske, M. Jaroszeski, D.S. Reintgen, and R. Heller, *Bleomycin-mediated electrochemotherapy of metastatic melanoma.* Arch Dermatol, 1996. 132(11):1353-7.
69. Gothelf, A., L.M. Mir, and J. Gehl, *Electrochemotherapy: results of cancer treatment using enhanced delivery of bleomycin by electroporation.* Cancer Treat Rev, 2003. 29(5):371-87.
70. Gowrishankar, T.R. and J.C. Weaver, *Electrical behavior and pore accumulation in a multicellular model for conventional and supra electroporation.* Biochemical and Biophysical Research Communications, 2006. 349(2):643-653.
71. Granot, Y., A. Ivorra, E. Maor, and B. Rubinsky, *In vivo imaging of irreversible electroporation by means of electrical impedance tomography.* Phys Med Biol, 2009. 54(16):4927-43.
72. Hall, E.J., *Radiobiology for the Radiologist*. 5th ed. 2000, Baltimore, MD: Lippincott Williams and Wilkins.
73. Hamilton, W.A. and A.J. Sale, *Effects of high electric fields on microorganisms. 2. Mechanism of action of the lethal effect.* Biochimica et Biophysica Acta (BBA), 1967. 163:37-43.
74. Heidner, G.L., J.N. Kornegay, R.L. Page, R.K. Dodge, and D.E. Thrall, *Analysis of survival in a retrospective study of 86 dogs with brain tumors.* J Vet Intern Med, 1991. 5(4):219-26.
75. Heller, R., R. Gilbert, and M.J. Jaroszeski, *Clinical applications of electrochemotherapy.* Advanced drug delivery reviews, 1999. 35:119-129.
76. Henriques, F.C. and A.R. Moritz, *Studies in thermal injuries: the predictability and the significance of thermally induced rate processes leading to irreversible epidermal damage.* Arch Pathol., 1947. 43:489-502.
77. Hibino, M., H. Itoh, and K. Kinosita, Jr., *Time courses of cell electroporation as revealed by submicrosecond imaging of transmembrane potential.* Biophys J, 1993. 64(6):1789-800.
78. Hinshaw, J.L. and F.T. Lee Jr, *Cryoablation for Liver Cancer.* Techniques in Vascular and Interventional Radiology, 2007. 10(1):47-57.
79. Ho, C.S., K.C. Ju, T.Y. Cheng, Y.Y. Chen, and W.L. Lin, *Thermal therapy for breast tumors by using a cylindrical ultrasound phased array with multifocus pattern scanning: a preliminary numerical study.* Phys Med Biol, 2007. 52(15):4585-99.
80. Hochberg, F.H. and A. Pruitt, *Assumptions in the radiotherapy of glioblastoma.* Neurology, 1980. 30(9):907-11.
81. Hoffman, G.A., *Cells in electric field. Physical and practical electronic aspects of electro cell fusion and electroporation*, in *Electroporation and Electrofusion in Cell Biology*, E. Neumann, A.E. Sowers, and C.A. Jordan, Editors. 1989, Plenum Press: New York, NY. p. 389-407.
82. Hulsheger, H. and E.G. Niemann, *Lethal effects of high-voltage pulses on E. coli K12.* Radiat Environ Biophys, 1980. 18(4):281-8.

83. Ivorra, A. and B. Rubinsky, *In vivo electrical impedance measurements during and after electroporation of rat liver.* Bioelectrochemistry, 2007. 70(2):287-95.
84. Ivorra, A., B. Al-Sakere, B. Rubinsky, and L.M. Mir, *In vivo electrical conductivity measurements during and after tumor electroporation: conductivity changes reflect the treatment outcome.* Phys Med Biol, 2009. 54(19):5949-63.
85. Ivorra, A., *Tissue electroporation as a biolectric phenomenon: Basic concepts*, in *Irreversible Electroporation*, B. Rubinsky, Editor. 2010, Springer Berlin: Heidelberg. p. 23-61.
86. Jacques S L, Newman C, and He X Y, *Thermal coagulation of tissues: liver studies indicate a distribution of rate parameters, not a single rate parameter, describes the coagulation process* in *Advances in Biological Heat and Mass Transfer* 1991, J McGrath: New York: ASME. p. 71-73.
87. Jaffe, R., *The practice of electroconvulsive therapy: Recommendations for treatment, training, and privileging: A task force report of the American Psychiatric Association, 2nd ed.* Am J Psychiatry, 2002. 159:331.
88. Janzen, N.K., K.T. Perry, K.-R. Han, B. Kristo, S. Raman, and e. al, *The effects of intentional cryoablation and radio frequency ablation of renal tissue involving the collecting system in a porcine model.* J Urol, 2005. 173:1368-1374.
89. Jerry, R.A., A.S. Popel, and W.E. Brownell, *Potential distribution for a spheroidal cell having a conductive membrane in an electric field.* IEEE Trans Biomed Eng, 1996. 43(9):970-2.
90. Jones, J.L., C.C. Proskauer, W.K. Paull, E. Lepeschkin, and R.E. Jones, *Ultrastructural injury to chick myocardial cells in vitro following "electric countershock".* Circ Res, 1980. 46(3):387-94.
91. Joshi, R.P. and K.H. Schoenbach, *Mechanism for membrane electroporation irreversibility under high-intensity, ultrashort electrical pulse conditions.* Phys Rev E Stat Nonlin Soft Matter Phys, 2002. 66(5 Pt 1):052901.
92. Kekez, M.M., P. Savic, and B.F. Johnson, *Contribution to the biophysics of the lethal effects of electric field on microorganisms.* Biochim Biophys Acta, 1996. 1278(1):79-88.
93. Kinosita Jr, K. and T.Y. Tsong, *Hemolysis of human erythrocytes by a transient electric field.* Proc. Natl. Acad. Sci. USA, 1977. 74(5):1923-1927.
94. Kinosita, K., Jr. and T.Y. Tsong, *Formation and resealing of pores of controlled sizes in human erythrocyte membrane.* Nature, 1977. 268(5619):438-41.
95. Kinosita, K., Jr., I. Ashikawa, N. Saita, H. Yoshimura, H. Itoh, K. Nagayama, and A. Ikegami, *Electroporation of cell membrane visualized under a pulsed-laser fluorescence microscope.* Biophys J, 1988. 53(6):1015-9.
96. Kleihues, P., P.C. Burger, and B.W. Scheithauer, *The new WHO classification of brain tumours.* Brain Pathol, 1993. 3(3):255-68.
97. Koestner, A. and R.J. Higgins, *Tumors of Domestic Animals*, in *Tumors of the nervous system*, D.J. Meuten, Editor. 2002, Iowa State University Press: Ames, IA. p. 697.
98. Kontos, M., E. Felekouras, and I.S. Fentiman, *Radiofrequency ablation in the treatment of primary breast cancer: no surgical redundancies yet.* Int J Clin Pract, 2008. 62(5):816-820.
99. Kotnik, T., F. Bobanovic, and D. Miklavcic, *Sensitivity of transmembrane voltage induced by applied electric fields - a theoretical analysis.* Bioelectrochemistry and Bioenergetics, 1997. 43(2):285-291.

100. Kotnik, T., D. Miklavcic, and T. Slivnik, *Time course of transmembrane voltage induced by time-varying electric fields - a method for theoretical analysis and its application.* Bioelectrochemistry and Bioenergetics, 1998. 45(1):3-16.
101. Kotnik, T. and D. Miklavcic, *Analytical description of transmembrane voltage induced by electric fields on spheroidal cells.* Biophys. J., 2000. 79:670-679.
102. Krassowska, W., G.S. Nanda, M.B. Austin, S.B. Dev, and D.P. Rabussay, *Viability of cancer cells exposed to pulsed electric fields: the role of pulse charge.* Ann Biomed Eng, 2003. 31(1):80-90.
103. Krassowska, W. and P.D. Filev, *Modeling electroporation in a single cell.* Biophys J, 2007. 92(2):404-17.
104. Kumar, A.J., N.E. Leeds, G.N. Fuller, P. Van Tassel, M.H. Maor, R.E. Sawaya, and V.A. Levin, *Malignant gliomas: MR imaging spectrum of radiation therapy- and chemotherapy-induced necrosis of the brain after treatment.* Radiology, 2000. 217(2):377-84.
105. La Rocca, R.V. and H.M. Mehdorn, *Localized BCNU chemotherapy and the multimodal management of malignant glioma.* Curr Med Res Opin, 2009. 25(1):149-60.
106. Lackovic, I., R. Magjarevic, and D. Miklavcic, *Three-dimensional finite-element analysis of joule heating in electrochemotherapy and in vivo gene electrotransfer.* IEEE Transactions on Dielectrics and Electrical Insulation, 2009. 16(5):1338-1347.
107. Latikka, J., T. Kuurne, and H. Eskola, *Conductivity of living intracranial tissues.* Phys Med Biol, 2001. 46(6):1611-6.
108. Lavee, J., G. Onik, P. Mikus, and B. Rubinsky, *A novel nonthermal energy source for surgical epicardial atrial ablation: irreversible electroporation.* Heart Surg Forum, 2007. 10(2):E162-7.
109. LeCouteur, R.A., *Tumors of the nervous system*, in *Small Animal Clinical Oncology*, S.J. Withrow and E.G. MacEwen, Editors. 2001, WB Saunders Co: Philadelphia, PA.
110. Lee, E.W., C.T. Loh, and S.T. Kee, *Imaging guided percutaneous irreversible electroporation: ultrasound and immunohistological correlation.* Technol Cancer Res Treat, 2007. 6(4):287-94.
111. Lee, R.C. and M.S. Kolodney, *Electrical injury mechanisms: Electrical breakdown of cell membranes.* Plast Reconstr Surg, 1987. 80(5):672-9.
112. Lee, R.C., D. Zhang, and J. Hannig, *Biophysical injury mechanisms in electrical shock trauma.* Annual Review of Biomedical Engineering, 2000. 2(1):477-509.
113. Lee, R.C., *Cell Injury by Electric Forces.* Annals of the New York Academy of Sciences, 2005. 1066:85-91.
114. Lee, R.C. and F. Despa. *Distinguishing Electroporation from Thermal Injuries in Electrical Shock by MR Imaging*. in *Engineering in Medicine and Biology 27th Annual Conference*. 2005. Shanghai, China: IEEE.
115. Leonardi, M.A., C.B. Lumenta, H.K. Gumprecht, G.H. von Einsiedel, and T. Wilhelm, *Stereotactic guided laser-induced interstitial thermotherapy (SLITT) in gliomas with intraoperative morphologic monitoring in an open MR-unit.* Minim Invasive Neurosurg, 2001. 44(1):37-42.
116. Lesser, G.J. and S. Grossman, *The chemotherapy of high-grade astrocytomas.* Semin Oncol, 1994. 21(2):220-35.

117. Lubicki, P. and S. Jarayam, *High voltage pulse application for the destruction of the Gram-negative bacterium.* BIoelectrochem Bioenerg, 1997. 43:135-141.
118. Luginbuhl, H., R. Fankhauser, and J.T. McGrath, *Spontaneous neoplasms of the nervous system of animals.* Prog Neurology Surgery, 1968. 2:85-164.
119. Lynn, J.G., R.L. Zwemer, and A.J. Chick, *The biological application of focused ultrasonic waves.* Science, 1942. 96(2483):119-120.
120. Macek-Lebar, A. and D. Miklavcic, *Cell electropermeabilization to small molecules in vitro: control by pulse parameters.* Radiol Oncol, 2001. 35(3):193-202.
121. Maor, E., A. Ivorra, J. Leor, and B. Rubinsky, *The effect of irreversible electroporation on blood vessels.* Technology in Cancer Research and Treatment, 2007. 6(4):307-312.
122. Maor, E., A. Ivorra, and B. Rubinsky, *Non thermal irreversible electroporation: novel technology for vascular smooth muscle cells ablation.* PLoS ONE, 2009. 4(3):e4757.
123. Marty, M., G. Sersa, J. Garbay, J. Gehl, C. Collins, M. Snoj, V. BIllard, P. Geersten, J. Larkin, and D. Miklavcic, *Electrochemotherapy - an easy, highly effective and safe treatment of cutaneous and subcutaneous metastases: results of the ESOPE (European Standard Operating Procedures of Electrochemotherapy) study.* Eur J Cancer Supplements, 2006. 4:3-13.
124. Matsumi, N., K. Matsumoto, N. Mishima, E. Moriyama, T. Furuta, A. Nishimoto, and K. Taguchi, *Thermal damage threshold of brain tissue--histological study of heated normal monkey brains.* Neurol Med Chir (Tokyo), 1994. 34(4):209-15.
125. Miklavcic, D., K. Beravs, D. Semrov, M. Cemazar, F. Demsar, and G. Sersa, *The importance of electric field distribution for effective in vivo electroporation of tissues.* Biophysical Journal, 1998. 74(5):2152-2158.
126. Miklavcic, D., D. Semrov, H. Mekid, and L.M. Mir, *A validated model of in vivo electric field distribution in tissues for electrochemotherapy and for DNA electrotransfer for gene therapy.* Biochimica et Biophysica Acta, 2000. 1523(1):73-83.
127. Mir, L.M., S. Orlowski, J. Belehradek, Jr., and C. Paoletti, *Electrochemotherapy potentiation of antitumour effect of bleomycin by local electric pulses.* Eur J Cancer, 1991. 27(1):68-72.
128. Mir, L.M., L.F. Glass, G. Sersa, J. Teissie, C. Domenge, D. Miklavcic, M.J. Jaroszeski, S. Orlowski, D.S. Reintgen, Z. Rudolf, M. Belehradek, R. Gilbert, M.P. Rols, J. Belehradek, J.M. Bachaud, R. Deconti, B. Stabuc, M. Cemazar, P. Coninx, and R. Heller, *Effective treatment of cutaneous and subcutaneous malignant tumours by electrochemotherapy.* British Journal of Cancer, 1998. 77(12):2336-2342.
129. Mir, L.M., *Therapeutic perspectives of in vivo cell electropermeabilization.* Bioelectrochemistry, 2001. 53(1):1-10.
130. Mir, L.M., J. Gehl, G. Sersa, C. Collins, J. Garbay, V. BIllard, P. Geersten, Z. Rudolf, G. O'Sullivan, and M. Marty, *Standard operating procedures of the electrochemotherapy.* Eur J Cancer Supplements, 2006. 4:14-25.
131. Moustakas, A. and T.N. Kreisl, *New treatment options in the management of glioblastoma multiforme: a focus on bevacizumab.* Onco Targets Ther, 2010. 3:27-38.
132. Neal II, R.E. and R.V. Davalos, *The feasibility of irreversible electroporation for the treatment of breast cancer and other heterogeneous systems.* Ann Biomed Eng, 2009. 37(12):2615-25.

133. Neal II, R.E., R. Singh, H.C. Hatcher, N.D. Kock, S.V. Torti, and R.V. Davalos, *Treatment of breast cancer through the application of irreversible electroporation using a novel minimally invasive single needle electrode.* Breast Cancer Res Treat, 2010. 123(1):295-301.
134. Neu, J.C. and W. Krassowska, *Asymptotic model of electroporation.* Phys. Rev. E, 1999. 59(3):3471-82.
135. Neumann, E. and K. Rosenheck, *Permeability changes induced by electric impulses in vesicular membranes.* J. Membrane Biol., 1972. 10:279-290.
136. Neumann, E., S. Kakorin, and K. Toensing, *Membrane electroporation and electromechanical deformation of vesicles and cells.* Faraday Discuss, 1998(111):111-25; discussion 137-57.
137. Nishikawa, R., *Standard therapy for glioblastoma--a review of where we are.* Neurol Med Chir (Tokyo), 2010. 50(9):713-9.
138. Nollet, J.A., *Recherches sur les causes particulieres des phenomenes electriques*. 1754, Paris: Chez H.L. Guering & L.F. Delatour.
139. Nuccitelli, R., U. Pliquett, X. Chen, W. Ford, R. James Swanson, S.J. Beebe, J.F. Kolb, and K.H. Schoenbach, *Nanosecond pulsed electric fields cause melanomas to self-destruct.* Biochem Biophys Res Commun, 2006. 343(2):351-60.
140. Nuccitelli, R., X. Chen, A.G. Pakhomov, W.H. Baldwin, S. Sheikh, J.L. Pomicter, W. Ren, C. Osgood, R.J. Swanson, J.F. Kolb, S.J. Beebe, and K.H. Schoenbach, *A new pulsed electric field therapy for melanoma disrupts the tumor's blood supply and causes complete remission without recurrence.* Int J Cancer, 2009. 125(2):438-45.
141. Okino, M., H. Tomie, H. Kanesada, M. Marumoto, K. Esato, and H. Suzuki, *Optimal electric conditions in electrical impulse chemotherapy.* Jpn J Cancer Res, 1992. 83(10):1095-101.
142. Olson, M.E., N.L. Chernik, and J.B. Posner, *Infiltration of the leptomeninges by systemic cancer. A clinical and pathologic study.* Arch Neurol, 1974. 30(2):122-37.
143. Onik, G., P. Mikus, and B. Rubinsky, *Irreversible Electroporation: Implications for Prostate Ablation.* Technol Cancer Res Treat, 2007. 6(4):295-300.
144. Organ, L.W., *Electrophysiologic principles of radiofrequency lesion making.* Appl Neurophysiol, 1976. 39(2):69-76.
145. Ozaki, T., K. Tabuse, T. Tsuji, Y. Nakamura, K. Kakudo, and I. Mori, *Microwave cell death: Enzyme histochemical evaluation for metastatic carcinoma of the liver.* Pathol Int, 2003. 53(12):837-45.
146. Parham, J.H., M.A. Iannone, L.K. Overton, and J.T. Hutchins, *Optimization of transient gene expression in mammalian cells and potential for scale-up using flow electroporation.* Cytotechnology, 1998. 28(1-3):147-55.
147. Pavselj, N., Z. Bregar, D. Cukjati, D. Batiuskaite, L.M. Mir, and D. Miklavcic, *The course of tissue permeabilization studied on a mathematical model of a subcutaneous tumor in small animals.* IEEE Trans Biomed Eng, 2005. 52(8):1373-81.
148. Pinero, J., M. Lopez-Baena, T. Ortiz, and F. Cortes, *Apoptotic and necrotic cell death are both induced by electroporation in HL60 human promyeloid leukaemia cells.* Apoptosis, 1997. 2(3):330-6.
149. Pliquett, U., *Joule heating during solid tissue electroporation.* Med Biol Eng Comput, 2003. 41(2):215-9.

150. Pucihar, G., T. Kotnik, B. Valic, and D. Miklavcic, *Numerical determination of transmembrane voltage induced on irregularly shaped cells.* Ann Biomed Eng, 2006. 34(4):642-52.
151. Rockwell, A.D., ed. *The medical and surgical uses of electricity: including the X-ray, Finsen light, vibratory therapeutics, and high-frequency currents*. 1903, E.B. Treat & Company: New York.
152. Rossmeisl, J.H., R.B. Duncan, W.R. Huckle, and G.C. Troy, *Expression of vascular endothelial growth factor in tumors and plasma from dogs with primary intracranial neoplasms.* Am J Vet Res, 2007. 68(11):1239-45.
153. Rowan, N.J., S.J. MacGregor, J.G. Anderson, R.A. Fouracre, and O. Farish, *Pulsed electric field inactivation of diarrhoeagenic Bacillus cereus through irreversible electroporation.* Lett Appl Microbiol, 2000. 31(2):110-4.
154. Rubinsky, B., *Irreversible Electroporation in Medicine.* Technology in Cancer Research and Treatement, 2007. 6(4):255-260.
155. Rubinsky, B., G. Onik, and P. Mikus, *Irreversible electroporation: a new ablation modality--clinical implications.* Technol Cancer Res Treat, 2007. 6(1):37-48.
156. Rubinsky, B., ed. *Irreversible Electroporation*. 2010, Springer Berlin Heidelberg.
157. Ruby, K.M. and B. Zheng, *Gene targeting in a HUES line of human embryonic stem cells via electroporation.* Stem Cells, 2009. 27(7):1496-506.
158. Rylander, M.N., Y. Feng, Y. Zhang, J. Bass, R.J. Stafford, J. Hazle, and K.R. Diller, *Optimizing HSP expression in prostate cancer laser therapy through predictive computational models.* Journal of Biomedical Optics, 2005. 11(4):04111131-16.
159. Sabel, M.S., C.S. Kaufman, P. Whitworth, H. Change, L.H. Stocks, R. Simmons, and M. Schultz, *Cryoablation of Early-Stage Breast Cancer: Work-in-Progress Report of a Multi-Institutional Trial.* Ann Surg Oncol, 2004. 11(5):542-549.
160. Sale, A.J. and W.A. Hamilton, *Effects of high electric fields on micro-organisms. 1. Killing of bacteria and yeasts.* Biochimica et Biophysica Acta, 1967. 148:781-788.
161. Sale, A.J. and W.A. Hamilton, *Effects of high electric fields on micro-organisms. 3. Lysis of erythrocytes and protoplasts.* Biochim Biophys Acta, 1968. 163(1):37-43.
162. Salford, L.G., B.R. Persson, A. Brun, C.P. Ceberg, P.C. Kongstad, and L.M. Mir, *A new brain tumour therapy combining bleomycin with in vivo electropermeabilization.* Biochem Biophys Res Commun, 1993. 194(2):938-43.
163. Sapareto, S.A. and W.C. Dewey, *Thermal dose determination in cancer therapy.* Int J Radiat Oncol Biol Phys, 1984. 10(6):787-800.
164. Schoenbach, K.H., F.E. Peterkin, R.W.I. Aldden, and S.J. Beebe, *The effect of pulsed fields on biological cells: Experiments and applications.* IEEE Trans Biomed Eng, 1997. 25:284-292.
165. Schwan, H.P., *Electrical properties of tissue and cell suspensions.* Adv. Biol. Med. Phys., 1957. 5:147-209.
166. Schwarzmaier, H.J., F. Eickmeyer, W. von Tempelhoff, V.U. Fiedler, H. Niehoff, S.D. Ulrich, Q. Yang, and F. Ulrich, *MR-guided laser-induced interstitial thermotherapy of recurrent glioblastoma multiforme: preliminary results in 16 patients.* Eur J Radiol, 2006. 59(2):208-15.

167. Sel, D., D. Cukjati, D. Batiuskaite, T. Slivnik, L.M. Mir, and D. Miklavcic, *Sequential finite element model of tissue electropermeabilization.* IEEE Trans Biomed Eng, 2005. 52(5):816-27.
168. Sel, D., A.M. Lebar, and D. Miklavcic, *Feasibility of employing model-based optimization of pulse amplitude and electrode distance for effective tumor electropermeabilization.* IEEE Trans Biomed Eng, 2007. 54(5):773-81.
169. Shaw, E.G. and M.E. Robbins, *The management of radiation-induced brain injury.* Cancer Treat Res, 2006. 128:7-22.
170. Shaw, E.J., *Central nervous system overview*, in *Clinical Radiation Oncology*, L.L. Gunderson and J.E. Tepper, Editors. 2000, Churchill-Livingstone: Philadelphia, PA. p. 314-354.
171. Sherar, M.D., J.A. Moriarty, M.C. Kolios, J.C. Chen, R.D. Peters, L.C. Ang, R.S. Hinks, R.M. Henkelman, M.J. Bronskill, and W. Kucharcyk, *Comparison of thermal damage calculated using magnetic resonance thermometry, with magnetic resonance imaging post-treatment and histology, after interstitial microwave thermal therapy of rabbit brain.* Phys Med Biol, 2000. 45(12):3563-76.
172. Sickles, E.A. and K.A. Herzog, *Intramammary scar tissue: a mimic of the mammographic appearance of carcinoma.* AJR Am J Roentgenol, 1980. 135(2):349-52.
173. Solbiati, L., T. Ierace, S.N. Goldberg, S. Sironi, T. Livraghi, R. Fiocca, G. Servadio, G. Rizzatto, P.R. Mueller, A. Del Maschio, and G.S. Gazelle, *Percutaneous US-guided radio-frequency tissue ablation of liver metastases: treatment and follow-up in 16 patients.* Radiology, 1997. 202(1):195-203.
174. Stampfli, R. and M. Willi, *Membrane potential of a Ranvier node measured after electrical destruction of its membrane.* Experientia, 1957. 13(7):297-8.
175. Stoica, G., H.T. Kim, D.G. Hall, and J.R. Coates, *Morphology, immunohistochemistry, and genetic alterations in dog astrocytomas.* Vet Pathol, 2004. 41(1):10-9.
176. Stupp, R., W.P. Mason, M.J. van den Bent, M. Weller, B. Fisher, M.J. Taphoorn, K. Belanger, A.A. Brandes, C. Marosi, U. Bogdahn, J. Curschmann, R.C. Janzer, S.K. Ludwin, T. Gorlia, A. Allgeier, D. Lacombe, J.G. Cairncross, E. Eisenhauer, and R.O. Mirimanoff, *Radiotherapy plus concomitant and adjuvant temozolomide for glioblastoma.* N Engl J Med, 2005. 352(10):987-96.
177. Summers, B.A., J.F. Cummings, and A. De Lahunta, *Tumors of the central nervous system*, in *Veterinary Neuropathology*. 1995, Mosby-Year Book Publishers, Inc.: St. Louis, MO. p. 364.
178. Swarup, A., S.S. Stuchly, and A. Surowiec, *Dielectric properties of mouse MCA1 fibrosarcoma at different stages of development.* Bioelectromagnetics, 1991. 12(1):1-8.
179. Tabuse, K., *A new operative procedure of hepatic surgery using a microwave tissue coagulator.* Nippon Geka Hokan, 1979. 48(160-172).
180. Tacke, J., *Thermal therapies in interventional MR imaging. Cryotherapy.* Neuroimaging Clin N Am, 2001. 11(4):759-65.
181. Thomas, W.B., S.J. Wheeler, R. Kramer, and J.N. Kornegay, *Magnetic resonance imaging features of primary brain tumors in dogs.* Veterinary Radiology & Ultrasound, 1996. 37(1):20-27.

182. Thomson, K., *Human experience with irreversible electroporation*, in *Irreversible Electroporation*, B. Rubinsky, Editor. 2010, Springer Berlin: Heidelberg. p. 249-254.
183. Toepfl, S., A. Mathy, V. Heinz, and D. Knorrr, *Review: Potential of high hydrostatic pressure and pulsed electric field for energy efficient and environmentally friendly food processing.* Food Review International, 2006. 22:405-423.
184. Tropea, B.I. and R.C. Lee, *Thermal injury kinetics in electrical trauma.* J Biomech Eng, 1992. 114(2):241-50.
185. Uzuka, T., R. Tanaka, H. Takahashi, K. Kakinuma, J. Matsuda, and K. Kato, *Planning of hyperthermic treatment for malignant glioma using computer simulation.* Int J Hyperthermia, 2001. 17(2):114-22.
186. Vandevelde, M. *Brain tumors in domestic animals: An overview*. in *Proceedings of the Conference on Brain Tumors in Man and Animals*. September 1984. Research Triangle Park, NC.
187. Vernhes, M.C., P.A. Cabanes, and J. Teissie, *Chinese hamster ovary cells sensitivity to localized electrical stresses.* Bioelectrochem Bioenerg, 1999. 48(1):17-25.
188. Vernhes, M.C., A. Benichou, P. Pernin, P.A. Cabanes, and J. Teissie, *Elimination of free-living amoebae in fresh water with pulsed electric fields.* Water Res, 2002. 36(14):3429-38.
189. Weaver, J.C. and A. Barnett, *Progress toward a theoretical model for electroporation mechanism: membrane electrical behavior and molecular transport*, in *Guide to Electroporation and Electrofusion*, D.C. Chang, Editor. 1992, Academic Press, Inc.: San Diego, CA.
190. Weaver, J.C., *Electroporation: a general phenomenon for manipulating cells and tissues.* J Cell Biochem, 1993. 51(4):426-35.
191. Weaver, J.C., *Electroporation theory. Concepts and mechanisms.* Methods Mol Biol, 1995. 48:3-28.
192. Weaver, J.C., *Electroporation in cells and tissues - a biophysical phenomenon due to electromagnetic-fields.* Radio Science, 1995. 30(1):205-221.
193. Weaver, J.C. and Y.A. Chizmadzhev, *Theory of electroporation: a review.* Bioelectrochem. Bioenerg., 1996. 41:135-60.
194. Weaver, J.C., *Electroporation of cells and tissues.* IEEE Transactions on Plasma Science, 2000. 28(1):24-33.
195. Weaver, J.C., *Electroporation of biological membranes from multicellular to nano scales.* IEEE Transactions on Dielectrics and Electrical Insulation, 2003. 10(5):754-768.
196. Werner, J. and M. Buse, *Temperature profiles with respect to inhomogeneity and geometry of the human body.* J Appl Physiol, 1988. 65(3):1110-8.
197. Yang, R., N.T. Sanghvi, F.J. Rescorla, C.A. Galliani, F.J. Fry, S.L. Griffith, and J.L. Grosfeld, *Extracorporeal liver ablation using sonography-guided high-intensity focused ultrasound.* Invest Radiol, 1992. 27(10):796-803.
198. Zimmermann, U., J. Vienken, and G. Pilwat, *Dielectric breakdown of cell membranes,.* Biophysical Journal, 1974. 14(11):881-899.
199. Zimmermann, U., G. Pilwat, F. Beckers, and F. Riemann, *Effects of external electrical fields on cell membranes.* Bioelectrochem Bioenerg, 1976. 3:58-83.